DISSERTATION

ASPECTS OF MOAT FORMATION IN TROPICAL CYCLONE EYEWALL REPLACEMENT CYCLES

Submitted by

Christopher Michael Rozoff

Department of Atmospheric Science

In partial fulfillment of the requirements

for the Degree of Doctor of Philosophy

Colorado State University

Fort Collins, Colorado

Summer 2007

COLORADO STATE UNIVERSITY

3 April 2007

WE HEREBY RECOMMEND THAT THE DISSERTATION PREPARED UNDER OUR SUPERVISION BY CHRISTOPHER MICHAEL ROZOFF ENTITLED ASPECTS OF MOAT FORMATION IN TROPICAL CYCLONE EYEWALL REPLACEMENT CYCLES BE ACCEPTED AS FULFILLING IN PART REQUIREMENTS FOR THE DEGREE OF DOCTOR OF PHILOSOPHY.

Committee on Graduate Work

Outside Member: Prof. Iuliana Oprea

Department Member: Prof. William R. Cotton

Advisor: Prof. Wayne H. Schubert

Committee Member and Department Head:
Prof. Richard H. Johnson

ABSTRACT OF DISSERTATION

ASPECTS OF MOAT FORMATION IN TROPICAL CYCLONE EYEWALL REPLACEMENT CYCLES

In order to increase our fundamental understanding of rapid intensity change in tropical cyclones (TCs), the evolving kinematic and thermodynamic conditions in TC eyewall replacement cycles and attendant moats are examined in this study. With the assistance of theory, observations, and cloud-resolving numerical simulations, the response of convection to typical environments outside of intense TC cores is addressed. In our analysis of the environmentally-dependent behaviors of deep, convective clouds, we consider new hypotheses and insights in rainband dynamics and concentric eyewall formation.

Re-visiting basic stirring criteria for two-dimensional flows, we derive simple rules-of-thumb for the existence of deep, moist convection in environments of intense horizontal strain. These results are compared with numerical integrations of vorticity in a nondivergent barotropic model. The kinematic and thermodynamic environments during eyewall replacement cycles are documented through observational case studies incorporating dense arrays of dropsondes and aircraft data. Moat observations are compared with idealized balanced vortex theory to increase our understanding of moat dynamics. In addition, idealized cloud-resolving, numerical simulations are carried out to address how horizontal strain, vertical shear and the thermodynamic basic state influence individual deep, convective clouds in TC-like environments.

We find that regions of intense horizontal strain are quite common outside of intense TC eyewalls. Observations show this region is also marginally unstable at low-levels and that, as a moat forms in concentric eyewall formation, the region outside of an inner eyewall acquires eye-like thermodynamics. Consistent with observations, idealized solutions to an axisymmetric, balanced-vortex model show that subsidence rapidly increases in the moat region as a secondary eyewall forms. In the midst of marginal convective instability, our idealized cloud simulations suggest a practical threshold for adverse filamentation of convective clouds. However, convection exhibits increasing resiliency to adverse strain under increasingly favorable thermodynamic conditions. Also, rich dynamics, which are most likely at work in concentric eyewall and moat formation and in rainbands, are revealed in our systematic exploration of convective behaviors across a wide spectrum of horizontal and vertical shears.

Christopher Michael Rozoff
Department of Atmospheric Science
Colorado State University
Fort Collins, Colorado 80523
Summer 2007

ACKNOWLEDGEMENTS

I would like to thank my advisor, Professor Wayne H. Schubert, who gave me the opportunity to carry out this research in a collaborative research environment, with his patient insight, support and guidance. Great appreciation is also extended to my committee members, Professors William R. Cotton, Richard Johnson, and Iuliana Oprea, who have taken the time to offer advice and support in this research. Professor Michael Montgomery, of the Naval Postgraduate School, also provided pivotal advice in much of this work.

A lot of research I have worked on has been cooperative. In particular, my research has benefitted from joint projects with Paul Ciesielski, Prof. Scott Fulton, Dr. James Kossin, Brian McNoldy, Wesley Terwey, and Jonathan Vigh. Brian McNoldy's tutoring in graphics display was invaluable in my research as well. Rick Taft also provided invaluable computer and technical support in this research. Useful discussions and help with RAMS from Drs. William Cheng, Louie Grasso, Sue van den Heever, and Dr. Mel Nicholls are greatly appreciated. Michael Bell, Dr. Michael Black, Dr. Neal Dorst, Kevin Mallen, and Dr. Hugh Willoughby have been instrumental in obtaining hurricane observational data. Advice and comments from Matt Masarik, Dr. Matt Parker, Dr. John Persing, Dr. Dave Schecter, and Russ Schumacher have proved very helpful at various times. Gail Cordova deserves many thanks for her dedicated administrative support for this research.

Finally, I would like to thank my family and friends for always encouraging me

to follow my dreams. I would especially like to thank my wife Jill for her editorial assistance in this dissertation and for her constant support and love during this arduous process.

This research was supported by the National Science Foundation under grants ATM-0530884, ATM-0332197, ATM-0435644, and ATM-0715426. Support was also received from NASA under grant NNG06GA54G.

CONTENTS

FIGURES

TABLES

Chapter 1

INTRODUCTION

1.1 Opening remarks

In the last 30 years, we have witnessed vast improvements in tropical cyclone (TC) prediction. However, a large portion of this success lies in the area of track forecasting. Rapid intensity change still poses a substantial challenge for operational forecasting (Snow et al., 2006). For instance, current indicators of maximum potential intensity (MPI) for a TC (Emanuel, 1988; Holland, 1997) are rarely achieved in real storms, and in other cases, MPI can be exceeded because of asymmetric mixing of high equivalent potential temperature (θ_e) air from the eye into the eyewall (e.g., Persing et al., 2003; Montgomery et al., 2006; Bell and Montgomery, 2007). Intensity fluctuations can be rapid due to TC interactions with an evolving environment and internal dynamical processes. Large-scale environmental factors are relatively well resolved on TC timescales, whereas asymmetric, internal processes, which may result from environmental forcing and ocean-atmosphere feedbacks, are not. Forecast models that can resolve internal TC dynamics are also sensitive to small errors in initial conditions which can lead to large ensemble spreads.

1.2 Eyewall replacement cycles

A well-known challenge in rapid intensity change includes accurate forecasts of eyewall replacement cycles (ERCs). ERCs are quite common in intense TCs. According to passive microwave satellite imagery, over 50 % of all TCs attaining

at least 120 kt wind speeds undergo ERCs (Hawkins et al., 2006). A basic ERC begins with organization of rainbands surrounding an intense TC into a concentric, convective ring. As a secondary eyewall forms, the primary eyewall often dissipates, maximum tangential winds decrease, and the central pressure rises. On the other hand, secondary eyewalls often drastically spread the width of damaging winds. In a full ERC, the secondary eyewall eventually contracts and the maximum tangential wind re-intensifies. However, in some intense storms, a secondary eyewall forms but never fully contracts to the radius of the original eyewall while other storms are known to repeat self-similar ERCs.

Essential characteristics of an ERC are well-illustrated in an observational study by Willoughby et al. (1982). Figure 1.1 shows central pressure and eye diameter as a function of time in Hurricane Allen (1980). These data were collected from satellite estimations and aircraft observations. Between 3–10 August, the central pressure fluctuates dramatically between roughly 900 and 970 hPa with periodicity ranging between one and two days. These findings demonstrate how rises in pressure often accompany discontinuous jumps in the estimated eye diameter. As confirmed in corresponding flight-level radar reflectivity (Willoughby et al., 1982), these jumps are associated with a secondary eyewall that has overtaken the primary eyewall. After such a jump, the new primary eyewall contracts and the pressure rapidly falls. Two complete ERCs are captured in Fig. 1.1.

Concentric eyewalls have been documented for over 50 years. Fortner (1958) was the first to publish observations of a concentric eyewall cycle, where Typhoon Sarah (1956) produced a 46 m s^{-1} drop in maximum flight-level winds in eight hours in connection with an ERC. Since this pioneering paper, concentric eyewalls have been noted and analyzed in numerous observational studies (e.g., Jordan and Schatzle, 1961; Jordan, 1966; Hoose and Colon, 1970; Holliday, 1977; Black and Willoughby, 1992; Samsury and Zipser, 1995; Dodge et al., 1999; Houze et al., 2007; among others).

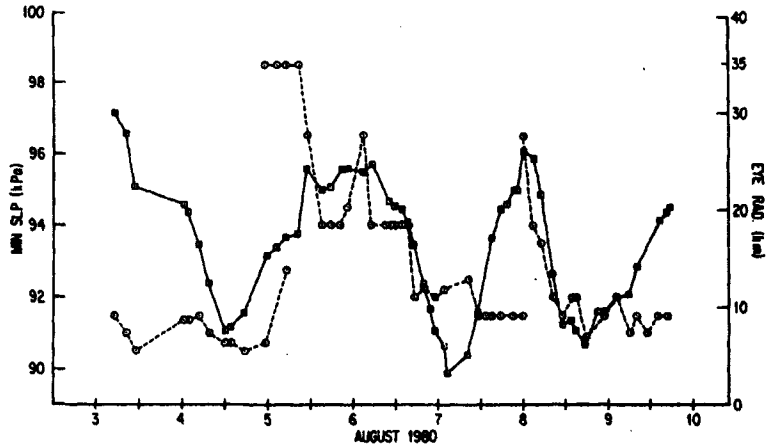

Figure 1.1: Eye radius (dashed) and central pressure (solid) for Hurricane Allen (1980). The date is plotted at 1200 UTC for each day. This figure is taken from Willoughby et al. (1982).

McNoldy (2004) even documented a triple eyewall structure in the Eastern Pacific Hurricane Juliette (2001). Because it was noted in early studies that secondary eyewall formation is associated with the weakening of the primary eyewall and the overall maximum wind, project STORMFURY was launched in 1969 to find out if targeted cloud seeding could form secondary eyewalls, but the results were inconclusive (Gentry, 1970; Hawkins, 1971; and Black et al., 1972). One of the most comprehensive documentations of ERCs up to its point was the observational analysis of Willoughby et al. (1982). As confirmed in the recent, comprehensive study of Hawkins et al. (2006), Willoughby et al. (1982) suggested concentric eyewalls are commonplace in intense TCs.

A full theory for the ERC requires physical explanations for the genesis of a concentric eyewall, the subsequent death of a primary eyewall, the contraction of the secondary eyewall, why multiple or single eyewall configurations are preferred, and when and where secondary eyewalls are likely to form. The process of eyewall contraction is well understood and the death of the primary eyewall is fairly well explored in the literature. For a mature, concentric eyewall, a plausible explanation for secondary eyewall contraction was developed in Shapiro and Willoughby (1982).

Considering the Sawyer-Eliassen transverse circulation equation (e.g., Eliassen, 1951), Shapiro and Willoughby (1982) demonstrate that contraction of a heated ring located near the radius of maximum winds (RMW) occurs because of the large gradient in inertial stability situated immediately inside the RMW. This contraction mechanism is well supported in observational analysis (e.g., Willoughby, 1990). Considering the balanced vortex mechanism of Shapiro and Willoughby and incorporating observations of concentric eyewalls, Willoughby et al. (1982) determined that the situation of two concentric eyewalls creates hostile conditions for the inner eyewall since a component of the primary eyewall's low-level inflow is robbed by the outer ring. Adapting a nonhydrostatic model constructed with an elegant formulation of equilibrium thermodynamics (Ooyama, 1990; Ooyama, 2001) to an axisymmetric framework, Hausman (2001) successfully simulated a TC with ERCs. While Hausman's study confirmed earlier proposed mechanisms for primary eyewall replacement, he also found that when a concentric eyewall forms, mesoscale downdrafts resulting from precipitation underneath the primary eyewall's stratiform region advect low entropy and low angular momentum air from mid-troposphere into the boundary layer inflow. These conditions are unfavorable for the sustenance of the primary eyewall. Hausman's finding complements the observational study by Samsury and Zipser (1995) and the modeling work of Willoughby et al. (1984), which similarly suggest that low-level outflow from a secondary eyewall or surrounding rainbands decreases the entropy of boundary layer inflow into the primary eyewall.

The formation of a concentric eyewall remains elusive to a complete theory of an ERC. Numerical models have dominated the search for correct physical mechanisms since they may be the only feasible way to capture the probable small-scale processes required for secondary eyewall formation. Axisymmetric (Willoughby et al., 1984; Zeng, 1996; Hausman, 2001; Nong and Emanuel, 2003), 2D nondivergent barotropic (Kuo et al., 2004; Rozoff et al., 2006), and 3D models (Zhang et al., 2005; Terwey

and Montgomery, 2006; Wang, 2006; Yau et al., 2006) can produce concentric rings around an intense TC-like vortex. A high resolution (1.67 km grid spacing), real-time, 3D model has almost successfully predicted concentric eyewall formation in Hurricane Rita (2005) — the model forecasted secondary eyewall formation was 6–7 h too early (Houze et al., 2007). Since both axisymmetric and 2D nondivergent barotropic models form their own model equivalents of concentric eyewalls, there appears to be at least two fundamentally different types of physical mechanisms that can lead to secondary eyewall formation.

Axisymmetric models were the first to successfully simulate full ERCs. A key observation from Shapiro and Willoughby (1982) suggests a concentric, convective ring can appear before a secondary wind maximum emerges (see their Hurricane Anita description). For an axisymmetric vortex in thermal wind balance, Shapiro and Willoughby found that applying a point source of heat at a radius outside of the wind maximum accelerates the tangential wind inside that radius. This concept was further elucidated in Camp and Montgomery (2001). Using a nonhydrostatic, axisymmetric TC model with sophisticated ice microphysics, Willoughby et al. (1984) found multiple ERCs in a simulated TC. Sensitivity experiments in Willoughby et al. (1984) suggested inclusion of ice in the model is a necessary ingredient for secondary eyewall formation. Their hypothesis for secondary eyewall formation further involves increasing convective instability at low-levels and increasing upper-level inertial instability. At low-levels, enhanced surface fluxes associated with high wind speeds increase the boundary layer entropy. Simultaneously, cooling from melting ice aloft invigorates the potential convective instability. To realize this potential convective instability, Willoughby et al. (1984) conjectured that inertial instability of the upper-level outflow may create sufficient lift to overcome a low-level capping inversion. Zeng (1996) captured secondary eyewalls in an axisymmetric model without ice but provided evidence that inertial instability is important for the formation of deep convection in

secondary eyewalls. In his axisymmetric model simulation, Hausman (2001) revealed that symmetric instability is not essential for secondary eyewall formation. Low-level convergence is sufficient to force an incipient secondary eyewall. Nonetheless, inertial instability reinforces the young secondary eyewall in Hausman's simulations. Extra buoyancy associated with freezing expedited formation of a concentric eyewall, but ice was not essential in Hausman's simulation of an ERC.

A more recent axisymmetric study provides intriguing insight into important factors related to secondary eyewall formation. Using both an axisymmetric, two-layer model formulated with balanced dynamics and an idealized, full-physics, axisymmetric model of Rotunno and Emanuel (1987), Nong and Emanuel (2003) covered a wide phase space of situations to investigate the important processes in concentric eyewall formation. The full-physics component of their work suggests that in order to form a secondary eyewall, finite-amplitude perturbations are needed to overcome a capping inversion. Furthermore, they demonstrated that wind-induced surface heat exchange (WISHE) is essential for the growth of the perturbation. They also hypothesized that TC interactions with baroclinic eddies, topography, or sea surface temperature (SST) variations are likely the types of perturbations needed for concentric eyewall formation.

Research over the last decade has also suggested that asymmetric processes, which may be important in 3D models and which are essential in the nondivergent, barotropic models, are crucial to concentric eyewall formation. Using a 2D nondivergent barotropic model, Kuo et al. (2004) demonstrated that binary vortex interactions could lead to concentric rings of vorticity. Rozoff et al. (2006) showed that placing a strong central vortex within a field of randomly distributed vorticity can lead to concentric ring structures as well. At the same time, Montgomery and Kallenbach (1997), Montgomery and Enagonio (1998), Möller and Montgomery (1999), and Möller and Montgomery (2000) pointed out the possible importance of vortex Rossby waves prop-

agating on the mean potential vorticity (PV) gradient, which can accelerate the mean tangential flow near a stagnation radius. Asymmetric forcing by convectively coupled waves, which likely include vortex Rossby waves (Chen and Yau, 2001; Wang, 2001, 2002; Chen et al., 2003; Franklin et al., 2006), have been hypothesized to play a crucial role in secondary eyewall formation (Montgomery and Kallenbach, 1997). Study of these asymmetric processes is currently an active area of research.

In summary, there appears to be a variety of distinct mechanisms that may initiate secondary eyewalls in real TCs. Given a potential convectively unstable region in a simulated TC, axisymmetric models produce concentric eyewalls through somewhat stochastic, low-level convergence mechanisms that are available in such an axisymmetric setting. Nong and Emanuel (2003) draw out the probable importance of ocean feedbacks in developing an incipient secondary eyewall. Plausible asymmetric arguments have recently been offered to explain the forcing for incipient secondary eyewalls. No matter which forcing mechanisms for a secondary eyewall turn out to be relevant, the next problem to address is determination of the most probable radial location of secondary eyewall formation as a function of TC structure and environmental conditions. Many of the asymmetric studies offer potential regions based on wave-mean flow interactions and critical radii. However, another important consideration involves determining where a secondary eyewall is unlikely to initiate. The following section introduces an unfavorable region for the important secondary eyewall ingredient that is deep, moist convection.

1.3 Formation of the moat

Coincident with the formation of a secondary eyewall is the formation of a relatively convective free environment in between two eyewalls. This region is typically referred to as the "moat." [Note the definition of a moat here differs from the definition coined by Simpson and Starrett (1955) for the relatively cloud-free ring that

forms inside a TC's eye.] The tendency for convection to be suppressed in the moat is generally attributed to mesoscale subsidence between two regions of strong upward motion. As one example, through analysis of Doppler radar data, Dodge et al. (1999) found that the moat of Hurricane Gilbert (1988) was characterized by weak stratiform precipitation with 0.5–1.0 m s^{-1} downward motion below the bright band observed near 5 km height, and 0.5 m s^{-1} upward motion above 5 km. More recently, high-resolution dual Doppler analysis from the Hurricane Rainband and Intensity Change Experiment (RAINEX) shows that a well-formed moat in Hurricane Rita (2005) contained subsidence through much of the troposphere, and further, that eye-like thermodynamic dropsonde profiles exist in the moat's lower troposphere (Houze et al., 2006; and Houze et al., 2007).

Conventional thinking is that weak-echo moats form in conjunction with subsidence. However, the region outside of the RMW of an intense TC also contains strong horizontal strain. For example, in analogy to the surroundings of the stratospheric polar vortex, Guinn and Schubert (1993) refer to the region outside of the high PV core of a TC as a surf zone since the differential rotation of this region promotes repetitive wave breaking. Shapiro and Montgomery (1993) alluded to such processes in developing their asymmetric balance model. Kossin et al. (2000) also qualitatively hypothesized that filamentation outside a PV core is a possible reason for a weak-echo moat.

Given two mechanisms for the existence of a moat, questions still remain. In a moat, is horizontal strain or subsidence the leading reason for the suppression of convection? Since, prior to concentric eyewall formation, the region outside of the primary eyewall may not be experiencing as much subsidence as a well-formed moat, does horizontal strain help initiate the formation of a moat and suppress secondary eyewall formation within certain annular regions outside of the RMW of a TC? What role does filamentation play in the formation of a secondary eyewall? The research

that follows begins to address these important questions through consideration of the relative importance of both the effects of filamentation and subsidence in the suppression of convection in a forming moat.

1.4 Proposed research

We propose in the following work that strain-dominated flows filament cumulonimbus convection outside the cores of strong TCs. Moreover, we consider how adverse filamentation is modulated by different thermodynamic background states. This work employs theory, observations, and modeling to explore formation mechanisms for a moat. In Chapter 2, the definition of a rapid filamentation zone is derived and evaluated in simple 2D nondivergent, barotropic model applications. Some case studies of moat observations and balanced vortex arguments are considered in Chapter 3. In Chapter 4, a cloud-resolving model is utilized to understand the response of deep, moist convection to hurricane-like horizontal and vertical shears. Different thermodynamic environments are considered, and the dynamics and thermodynamics of convective elements in these environments is surveyed. These results are followed by conclusions and discussion in Chapter 5.

Chapter 2

RAPID FILAMENTATION THEORY AND APPLICATIONS

2.1 Overview

Strong deformation in the flow outside of the cores of intense TCs promotes rapid filamentation of important quantities including vorticity and passive tracers. Such regions are characterized by enhanced particle dispersion and mixing. Sometimes this region along the periphery of the vortex is referred to as the "surf zone" since it is an area where large-amplitude waves form and break. In the context of 2D turbulence, this region plays an essential role in the enstrophy cascade as vorticity gradients grow quickly here. Moreover, this filamentation region also plays a crucial role in vortex axisymmetrization (e.g., Melander et al, 1987; Polvani et al, 1989; Mariotti et al., 1994; Kimura and Herring, 2001; Louazel and Hua, 2004).

In 2D studies, the rate of filamentation is often assessed by evaluating vortex kinematics. For example, considering particle dispersion in steady flow, Okubo (1970) developed a 2D scheme classifying oceanic circulations by their relative strengths of divergence, vorticity, and deformation. In an attempt to physically describe the enstrophy cascade in 2D turbulence, Weiss (1991) arrived at a nondivergent form of Okubo's stirring criterion by exploring the time evolution of vorticity and tracer gradients. Weiss developed stirring criteria for flows assumed to have slowly varying velocity gradients and he also developed a more general criterion that relaxed the assumption of constant velocity gradients. Numerical experiments of forced and unforced 2D turbulence indicate that the assumption of slowly varying velocity gra-

dients, with respect to vorticity gradients, is typically only valid within vortex cores and in approximately 30 % of the model domain (Basdevant and Philipovitch, 1994). With this in mind, Hua and Klein (1998) expressed Weiss' more general criterion in terms of the pressure field, which provides a criterion that is simple to compute from model output. However, the above stirring criteria have limitations in the study of vortex filamentation because of the rotation of the strain axes along the vortex edge. Incorporating the strain bases of Dresselhaus and Tabor (1991), Lapeyre et al (1999) and Klein et al. (2000) derived stirring criteria for passive tracers, which account for the rotation of the strain principal axes and depend on Lagrangian accelerations. Lapeyre et al. (2001) extended these methods to study stirring of the active tracer of vorticity in flows with and without diffusion.

Considering the hierarchy of geophysical fluid dynamics models, more general stirring criteria have been developed. Hua and Klein (1998), Louazel and Hua (2004), and Lukovich and Shepherd (2005) have derived accurate shallow water model criteria which include the impact of divergence on particle dispersion and stirring. Hua et al. (1998) extended these concepts to the quasi-geostrophic system. More complete theories for 3D flows have emerged from vortex identification techniques (e.g, Haller, 2005).

2.2 Review of select two-dimensional stirring criteria

In the context of TCs, we now more closely examine relatively simple stirring criteria in order to diagnose regions of rapid filamentation in model and observational data. While divergent flow is associated with a TC's secondary circulation and its various asymmetries, the large-scale, axisymmetric flow outside of inner and secondary eyewalls is assumed to be nondivergent in the following discussion. From a nondivergent barotropic perspective, we can utilize kinematical stirring criteria to describe the evolution of convective clouds and vorticity outside of a hurricane core.

As mentioned above, stirring criteria can be derived considering the horizontal dispersion of particles. Okubo (1970) was the first to objectively divide flows into regions of rotation, strain, and divergence. Okubo considers steady flow on a horizontal plane. This horizontal plane can be interpreted as a physical height level in a 3D model. Letting u and v be the components of velocity along the horizontal, Cartesian x and y directions, respectively, then

$$\begin{pmatrix} \dot{x} \\ \dot{y} \end{pmatrix} = \begin{pmatrix} u(x,y) \\ v(x,y) \end{pmatrix}, \tag{2.1}$$

where the dotted variables designate time derivatives of the particle in trajectory. Expanding (2.1) into a Taylor series about a desired point set to $(x_0, y_0) = (0,0)$,

$$\begin{pmatrix} \dot{x} \\ \dot{y} \end{pmatrix} = \mathcal{V}_2 \begin{pmatrix} x \\ y \end{pmatrix} + \begin{pmatrix} u_0 \\ v_0 \end{pmatrix} + \text{H.O.T.}, \tag{2.2}$$

where (u_0, v_0) are the velocities at the origin (Okubo set these terms to zero), "H.O.T." denotes "higher order terms", which are neglected in the interest of studying motions close to the origin, and $\mathcal{V}_2$ is the 2D velocity gradient tensor defined by

$$\mathcal{V}_2 = \begin{pmatrix} \partial u/\partial x & \partial u/\partial y \\ \partial v/\partial x & \partial v/\partial y \end{pmatrix}. \tag{2.3}$$

Defining the horizontal divergence as

$$\delta = \frac{\partial u}{\partial x} + \frac{\partial v}{\partial y}, \tag{2.4}$$

the vertical component of vorticity as

$$\zeta = \frac{\partial v}{\partial x} - \frac{\partial u}{\partial y}, \tag{2.5}$$

and the stretching and shearing deformation as

$$S_n = \frac{\partial u}{\partial x} - \frac{\partial v}{\partial y} \tag{2.6}$$

and

$$S_s = \frac{\partial v}{\partial x} + \frac{\partial u}{\partial y}, \tag{2.7}$$

respectively, the 2D velocity gradient tensor can be written in the form

$$\mathcal{V}_2 = \frac{1}{2}\begin{pmatrix} \delta + S_n & S_s - \zeta \\ S_s + \zeta & \delta - S_n \end{pmatrix}. \tag{2.8}$$

Then, neglecting terms higher than order one in the Taylor series, (2.2) can be expressed as

$$\begin{pmatrix} \dot{x} \\ \dot{y} \end{pmatrix} = \frac{1}{2}\begin{pmatrix} \delta + S_n & S_s - \zeta \\ S_s + \zeta & \delta - S_n \end{pmatrix}\begin{pmatrix} x \\ y \end{pmatrix} + \begin{pmatrix} u_0 \\ v_0 \end{pmatrix}. \tag{2.9}$$

The flow patterns in the neighborhood of the origin can be classified by the complex eigenvalues of the velocity gradient tensor, which are

$$\lambda_o = \frac{1}{2}[\delta \pm (S_n^2 + S_s^2 - \zeta^2)^{1/2}]. \tag{2.10}$$

Assuming the velocity gradient tensor is constant in time, these eigenvalues are the frequencies associated with solutions to (2.9). The real (imaginary) part of λ_o corresponds to exponential (oscillatory) solutions. With (x_0, y_0) assumed to be an origin of zero velocity ("singularity"), Fig. 2.1 describes the solution space of trajectory patterns for different λ_o.

The ordinate in Fig. 2.1 specifies the relative importance between strain and vorticity. The abscissa describes the amount of divergence. Thus, in nondivergent flow, particles disperse in regions where strain dominates vorticity. If convergence is added in such a flow region, particle dispersion is mitigated, if not reversed. In nondivergent regions where vorticity dominates strain, particle separation is oscillatory. However, if divergence (convergence) is added to this region of flow, the particles will disperse away from (converge toward) one another.

An alternative way to obtain Okubo's stirring criterion is accomplished through analysis of tracer gradient evolution. We consider a materially conserved tracer q in

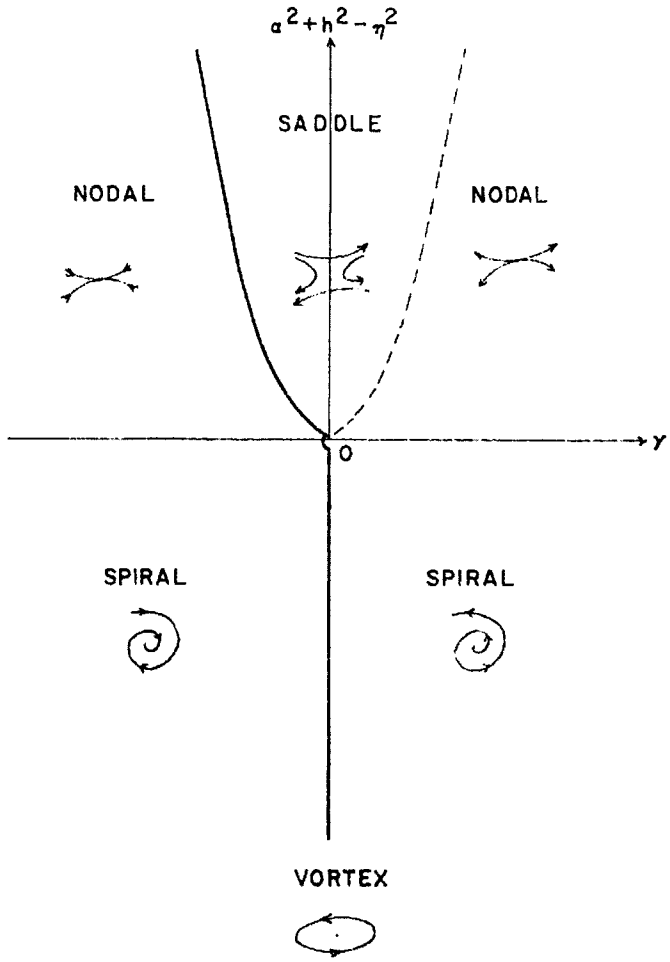

Figure 2.1: The flow classification based on the eigenvalues (2.10). Here $\alpha^2 + h^2 - \eta^2$ is $S_n^2 + S_s^2 - \zeta^2$ and γ represents δ. This figure is from Okubo (1970).

2D flow,

$$\frac{D_2 q}{Dt} \equiv \left(\frac{\partial}{\partial t} + \mathbf{u} \cdot \nabla_2 \right) q = 0, \tag{2.11}$$

where $\mathbf{u} = (u, v)$ and $\nabla_2 = (\partial/\partial x, \partial/\partial y)$. Here, q may represent the specific entropy of moist air (alternatively, the equivalent potential temperature), the mixing ratio of total airborne moisture (i.e., the sum of mixing ratios of water vapor and airborne condensate), the mixing ratio of precipitation, or even the moist PV (Schubert et al., 2001; Schubert, 2004). Differentiating (2.11) with respect to x and y, we find that

$$\frac{D_2}{Dt} \begin{pmatrix} \partial q/\partial x \\ \partial q/\partial y \end{pmatrix} + \mathcal{V}_2^T \begin{pmatrix} \partial q/\partial x \\ \partial q/\partial y \end{pmatrix} = 0, \tag{2.12}$$

where $\mathcal{V}_2^T$ is the transpose of the 2D velocity gradient tensor given in (2.3). As a result, the eigenvalues associated with this matrix are identical to λ_o obtained from Okubo's (1970) method.

To illustrate the dynamics of the 2D enstrophy cascade, Weiss (1991) considered the evolution of vorticity gradients in the nondivergent barotropic framework, and consequently, obtained the nondivergent version of Okubo's stirring criterion. The equations for 2D, nondivergent flow on the f-plane are

$$\frac{D_2 \mathbf{u}}{Dt} + f_0 \mathbf{k} \times \mathbf{u} = -\frac{1}{\rho_0} \nabla_2 p, \tag{2.13}$$

and

$$\nabla_2 \cdot \mathbf{u} = 0, \tag{2.14}$$

where f_0 is the constant Coriolis parameter, ρ_0 is the constant background density, and p is the pressure field. Cross differentiating both vector components of (2.13), we can form a vorticity equation and defining a streamfunction ψ for the nondivergent flow such that $(u, v) = (-\partial\psi/\partial y, \partial\psi/\partial x)$, we can obtain the invertibility principle for the nondivergent barotropic model:

$$\frac{D_2 \zeta}{Dt} \equiv \frac{\partial}{\partial t} \zeta + J_{xy}(\psi, \zeta) = 0, \tag{2.15}$$

and

$$\zeta = \nabla_2^2 \psi, \tag{2.16}$$

where $J_{xy}(\cdot,\cdot)$ is the Jacobian operator [i.e., $J_{xy}(\psi,\zeta) = (\partial\psi/\partial x)(\partial\zeta/\partial y) - (\partial\psi/\partial y)(\partial\zeta/\partial x)$]. Computing $\partial(2.15)/\partial x \pm i\,\partial(2.15)/\partial y$, we obtain

$$\frac{D_2}{Dt}\begin{pmatrix} \frac{\partial\zeta}{\partial x} + i\frac{\partial\zeta}{\partial y} \\ \frac{\partial\zeta}{\partial x} - i\frac{\partial\zeta}{\partial y} \end{pmatrix} = \frac{1}{2}\begin{pmatrix} i\zeta & -(S_n + iS_s) \\ -(S_n - iS_s) & -i\zeta \end{pmatrix}\begin{pmatrix} \frac{\partial\zeta}{\partial x} + i\frac{\partial\zeta}{\partial y} \\ \frac{\partial\zeta}{\partial x} - i\frac{\partial\zeta}{\partial y} \end{pmatrix}, \tag{2.17}$$

The eigenvalues corresponding to solutions of (2.17) are

$$\lambda_{\text{ow}} = \pm\frac{1}{2}\sqrt{S_n^2 + S_s^2 - \zeta^2}, \tag{2.18}$$

which is the nondivergent form of λ_o. For future convenience, we hereafter refer to λ_{ow} as the Okubo-Weiss eigenvalues. From the perspective of the nondivergent barotropic model, it should be pointed out vorticity is an active tracer. In contrast with a passive tracer, as vorticity is advected along by the flow, the new resulting vorticity distribution simultaneously changes the flow.

For the study of TC vortices, it is convenient to express the terms in (2.18) in the polar coordinates (r,θ). Noting the transformation of wind components from Cartesian to polar coordinates,

$$\begin{aligned} u &= v_r \cos\theta - v_\theta \sin\theta, \\ v &= v_r \sin\theta + v_\theta \cos\theta, \end{aligned} \tag{2.19}$$

and incorporating the chain rule,

$$\begin{aligned} \frac{\partial}{\partial x} &= \cos\theta\frac{\partial}{\partial r} - \sin\theta\frac{\partial}{r\partial\theta}, \\ \frac{\partial}{\partial y} &= \sin\theta\frac{\partial}{\partial r} + \cos\theta\frac{\partial}{r\partial\theta}, \end{aligned} \tag{2.20}$$

it can be shown that

$$S_n^2 + S_s^2 = \left(\frac{\partial v_r}{\partial r} - \frac{v_r}{r} - \frac{\partial v_\theta}{r\partial\theta}\right)^2 + \left(\frac{\partial v_\theta}{\partial r} - \frac{v_\theta}{r} + \frac{\partial v_r}{r\partial\theta}\right)^2, \tag{2.21}$$

and

$$\zeta^2 = \left(\frac{\partial v_\theta}{\partial r} + \frac{v_\theta}{r} - \frac{\partial v_r}{r \partial \theta} \right)^2, \tag{2.22}$$

where v_r and v_θ are the radial and tangential components of velocity, respectively. In the case of axisymmetry and zero radial flow, (2.21) and (2.22) give the following Okubo-Weiss eigenvalues:

$$\frac{1}{4}\left(S_n^2 + S_s^2 - \zeta^2\right) = -\frac{v_\theta}{r}\frac{\partial v_\theta}{\partial r} = -\omega\left(\omega + r\frac{\partial \omega}{\partial r}\right), \tag{2.23}$$

where $\omega = v_\theta / r$ is the angular velocity.

As briefly mentioned earlier, a more accurate description of 2D, nondivergent flow involves the acceleration gradient tensor. Following the method of Okubo (1970), Hua and Klein (1998) incorporated a local expansion of the flow velocity components to obtain an expression for the Lagrangian accelerations of particles. Here, the Lagrangian acceleration is defined as

$$\gamma_{\mathrm{L}} \equiv \begin{pmatrix} \gamma_x \\ \gamma_y \end{pmatrix} = \begin{pmatrix} \ddot{x} \\ \ddot{y} \end{pmatrix}. \tag{2.24}$$

Differentiating (2.9) with respect to time, we can obtain the second order equation governing particle motion:

$$\begin{pmatrix} \ddot{x} \\ \ddot{y} \end{pmatrix} = \left(\mathcal{V}_2^2 + \dot{\mathcal{V}}_2\right) \begin{pmatrix} x \\ y \end{pmatrix} + \gamma_{\mathrm{L}}(0), \tag{2.25}$$

where $\gamma_{\mathrm{L}}(0)$ is the acceleration at the locally defined origin. Because the flow is nondivergent, it can be shown that the tensor $\mathcal{V}_2^2 + \dot{\mathcal{V}}_2$ is the acceleration gradient tensor:

$$\mathcal{V}_2^2 + \dot{\mathcal{V}}_2 = \begin{pmatrix} \partial\gamma_x/\partial x & \partial\gamma_x/\partial y \\ \partial\gamma_y/\partial x & \partial\gamma_y/\partial y \end{pmatrix} \equiv \mathcal{A} \tag{2.26}$$

This acceleration gradient tensor can be recast into the following, convenient form:

$$\mathcal{A} = \begin{pmatrix} \frac{1}{4}(S^2 - \zeta^2) + \frac{1}{2}\dot{S}_n & \frac{1}{2}(\dot{S}_s - \dot{\zeta}) \\ \frac{1}{2}(\dot{S}_s + \dot{\zeta}) & \frac{1}{4}(S^2 - \zeta^2) - \frac{1}{2}\dot{S}_n \end{pmatrix}. \tag{2.27}$$

The eigenvalues for the matrix (2.27), which are hereafter referred to as Hua-Klein eigenvalues, are

$$\lambda_{\rm hk} = \left[\frac{1}{4}(S_n^2 + S_s^2 - \zeta^2) \pm \frac{1}{2}\sqrt{\dot{S}_n^2 + \dot{S}_s^2 - \dot{\zeta}^2}\right]^{\frac{1}{2}}. \tag{2.28}$$

The same result was obtained by Weiss (1991) from the approach of vorticity gradients. Because the second order equation for tracer gradients is more accurate, the Taylor expansion approach for the particle dispersion provides a more exact stirring criterion. Positive values of $\lambda_{\rm hk}$ correspond to regions of enhanced particle stirring and negative values imply particle containment.

Following a similar route as before, (2.28) may be expressed in polar coordinates. It can be shown that

$$\dot{S}_n^2 + \dot{S}_s^2 \equiv \dot{S}_n^2 + \dot{S}_s^2 - \dot{\zeta}^2 = \left(\dot{a} - \frac{2v_\theta b}{r}\right)^2 + \left(\dot{b} + \frac{2v_\theta a}{r}\right)^2, \tag{2.29}$$

where

$$a = \frac{\partial v_r}{\partial r} - \frac{v_r}{r} - \frac{\partial v_\theta}{r\partial\theta}, \tag{2.30}$$

and

$$b = \frac{\partial v_\theta}{\partial r} - \frac{v_\theta}{r} + \frac{\partial v_r}{r\partial\theta}. \tag{2.31}$$

Then, in the special case where $v_r = 0$ and the flow is axisymmetric,

$$\lambda_{\rm hk}^2 = -\frac{v_\theta}{r}\frac{\partial v_\theta}{\partial r} \pm \frac{v_\theta}{r}\left(\frac{\partial v_\theta}{\partial r} - \frac{v_\theta}{r}\right). \tag{2.32}$$

Eigenvalues associated with growing tracer gradients correspond with regions where the negative root is positive; namely,

$$\lambda_{\rm hk}^2 = \frac{v_\theta}{r}\left(\frac{v_\theta}{r} - 2\frac{\partial v_\theta}{\partial r}\right) > 0. \tag{2.33}$$

Finally, Hua and Klein (1998) showed that the eigenvalues $\lambda_{\rm hk}$ may be written in terms of the pressure field rather than in terms of Lagrangian derivatives. From (2.13) and (2.14), we obtain the nonlinear balance equation,

$$\nabla_2^2 p = \rho_0 f_0 \zeta - \frac{\rho_0}{2}\left(S_n^2 + S_s^2 - \zeta^2\right), \tag{2.34}$$

and the rate of strain equations, which are

$$\dot{S}_n - f_0 S_s + \frac{1}{\rho_0}\left(\frac{\partial^2}{\partial x^2} - \frac{\partial^2}{\partial y^2}\right) p = 0, \tag{2.35}$$

and

$$\dot{S}_s + f_0 S_n + \frac{2}{\rho_0}\frac{\partial^2 p}{\partial x \partial y} = 0. \tag{2.36}$$

Equations (2.34)–(2.36) and (2.15) allow $\mathcal{A}$ to adopt the form

$$\mathcal{A} = \begin{pmatrix} \frac{\partial}{\partial x}\left(f_0 v - \rho_0^{-1}\partial p/\partial x\right) & \frac{\partial}{\partial y}\left(f_0 v - \rho_0^{-1}\partial p/\partial x\right) \\ \frac{\partial}{\partial x}\left(-f_0 u - \rho_0^{-1}\partial p/\partial y\right) & \frac{\partial}{\partial y}\left(-f_0 u - \rho_0^{-1}\partial p/\partial y\right) \end{pmatrix}. \tag{2.37}$$

Defining $\hat{p} = p - \rho_0 f_0 \psi$, (2.37) can be written in terms of the Hessian, $[\hat{p}'']$, of the modified pressure, $\hat{p}$. Specifically,

$$\mathcal{A} = -\frac{1}{\rho_0}\begin{pmatrix} \frac{\partial^2 \hat{p}}{\partial x^2} & \frac{\partial \hat{p}}{\partial x \partial y} \\ \frac{\partial^2 \hat{p}}{\partial x \partial y} & \frac{\partial \hat{p}}{\partial y^2} \end{pmatrix} \equiv [\hat{p}'']. \tag{2.38}$$

We see the eigenvalues, λ_{hk}, are also equivalent to

$$\lambda_{\mathrm{hk}}^2 = \frac{1}{2\rho_0}\left[-\nabla_2^2 \hat{p} \pm \sqrt{\left(\frac{\partial \hat{p}}{\partial x^2} - \frac{\partial \hat{p}}{\partial y^2}\right)^2 + 4\left(\frac{\partial \hat{p}}{\partial x \partial y}\right)^2}\right]. \tag{2.39}$$

This expression is more convenient for our analysis of model output.

As noted earlier, the Okubo-Weiss and Hua-Klein eigenvalues are frequencies either associated with exponential or oscillatory solutions to the first- and second-order tracer gradient equations, respectively. Nonetheless, these eigenvalues fail to provide growth information about tracer gradient growth in uncurved, uniform shear flows. Such growth rates are applicable to the intrepretation of filamentation of horizontally-sheared convection 3D simulations in Chapter 4. In the 2D framework, a stirring criterion results from a relationship between the tracer gradient vector and the strain eigenvectors.

Following Dresselhaus and Tabor (1991), Lapeyre et al. (1999) develop equations for the evolution of passive tracer gradients in strain coordinates. They offer

a new stirring criterion — a ratio between effective rotation and the magnitude of strain, where effective rotation is defined as the sum of vorticity and the rotation of the principal axes of the strain-rate tensor. Assuming that these effective rotation and strain rates are slowly-varying along a Lagrangian trajectory (a valid assumption for axisymmetric vortices containing no radial flow), Lapeyre et al. find that tracer gradient growth in shear flow is algebraic. Furthermore, the growth rate is directly proportional to the rate of strain. Similarly, their method also predicts algebraic growth for axisymmetric vortices in response to the rotation of the strain axes. Whereas the Okubo-Weiss and Hua-Klein criteria are evaluated with instantaneous information about a given flow, we note the timescale used in Lapeyre et al. (1999) contains a Lagrangian history and is defined as

$$\tau = \int_0^t S(\xi) d\xi, \tag{2.40}$$

where S is the magnitude of strain, which is a function of the time t. Thus, this timescale would be long outside of the core of a strong vortex. Nonetheless, the implications of the algebraic growth prediction of tracer gradients in an axisymmetric vortex upon the following analysis should be resolved in future research.

2.3 Two-dimensional applications

We now apply our stirring criteria to TC-like vortices to diagnose regions kinematically unfavorable for deep, convective clouds. For now, we assume convection acts either like a passive tracer or vorticity and we only consider the Okubo-Weiss and Hua-Klein stirring criteria. The criteria are used to predict filamentation timescales for clouds in regions of horizontal strain.

To obtain a filamentation time, we note that regions of tracer gradient growth correspond to regions where stirring criteria are positive and real. Such eigenvalues correspond to exponential growth, while imaginary values are associated with oscillatory tracer gradient behavior. For the Okubo-Weiss criterion, strain-dominated

regions produce exponential growth of tracer and vorticity gradients, while vorticity-dominated regions generate oscillatory, nongrowing variations in the tracer gradient. The Hua-Klein eigenvalues typically produce a broader region of growth than predicted by the Okubo-Weiss criterion due to to the nonlocal effects of pressure [i.e., (2.39)].

Following Rozoff et al. (2006), we define a filamentation timescale for regions of tracer gradient growth as

$$\tau_{\text{fil}} = 1/\max\{\lambda_i\} \qquad \text{for} \qquad \lambda_i \in \mathbb{R}, \tag{2.41}$$

where λ_i represents either the Okubo-Weiss or Hua-Klein eigenvalues. As in Rozoff et al. (2006), we hypothesize cumulonimbus convection is distorted and potentially suppressed in regions where the filamentation time τ_{fil} is less than the time scale for deep, moist convection overturning, denoted here as τ_{conv}. A characteristic value for the convective overturning scale is $\tau_{\text{conv}} = 30$ min. This value for τ_{conv} is valid for a parcel traveling from the top of the boundary layer (600 m) to cloud top (15 km) with a typical updraft speed of 8 m s^{-1}, or for weaker updrafts of 3–4 m s^{-1} that extend slightly above freezing level before merging into a region of general mesoscale lift. The timescale is subjective and a rough characteristic of convective motions. Thus, a rapid filamentation zone is operationally defined as a region where $\tau_{\text{fil}} < \tau_{\text{conv}} = 30$ min. Following this hypothesis, we extend the primary analysis of rapid filamentation zones in the simple 2D, TC-like vortices of Rozoff et al. (2006) to the more accurate Hua and Klein (1998) criterion.

2.3.1 *Two-dimensional analytical examples*

As a first example, we consider a Rankine vortex, with angular velocity defined as

$$\omega(r) = \omega_0 \begin{cases} 1 & \text{if } 0 \leq r < a \\ (a/r)^2 & \text{if } r \geq a, \end{cases} \tag{2.42}$$

where $\omega = v_\theta / r$ is the angular velocity, a is the radius of maximum tangential wind and ω_0 is the constant angular velocity inside $r = a$. The axisymmetric value of the Okubo-Weiss eigenvalue for (2.42) is

$$\lambda_{ow}^2 = \omega_0^2 \begin{cases} -1 & \text{if } 0 \leq r < a \\ (a/r)^4 & \text{if } r > a. \end{cases} \tag{2.43}$$

In this Rankine vortex, there is a discontinuity from vorticity-dominated flow inside $r = a$ to strain-dominated flow outside of $r = a$. For the region of strain-dominated flow, the filamentation time for the Okubo-Weiss criterion is

$$\tau_{\text{fil}}(r) = \omega_0^{-1}(r/a)^2 \qquad \text{for} \qquad r > a. \tag{2.44}$$

On the other hand, the Hua and Klein (1998) criterion gives a filamentation time of

$$\tau_{\text{fil}}(r) = 3^{-\frac{1}{2}}\omega_0^{-1}(r/a)^2 \qquad \text{for} \qquad r > a. \tag{2.45}$$

Let us assume that $a = 15$ km and $\omega_0^{-1} = (50 \text{ m s}^{-1}/15 \text{ km})^{-1} = 300$ s. Then, according to the Okubo-Weiss criterion, τ_{fil} varies from 5 min at $r = 15$ km to 60 min at $r = 52$ km. Thus, the Okubo-Weiss rapid filamentation zone is the annular region defined by 15 km $< r <$ 37 km. On the other hand, the Hua-Klein parameter suggests that τ_{fil} varies from 2.9 min at $r = 15$ km to 60 min at $r = 68.4$ km. The Hua-Klein rapid filamentation zone is larger than the Okubo-Weiss counterpart and extends out to 48 km.

Next, in order to study a TC-like vortex in all its stages of intensity, we consider a family of Gaussian vortices with the tangential wind profile

$$v_\theta(r) = \frac{\Gamma}{2\pi r}\left(1 - e^{-r^2/b^2}\right), \tag{2.46}$$

where the constant Γ is the circulation at large radii and b is the e-folding distance of the vorticity distribution. The maximum tangential wind occurs at $r_{\max} \approx 1.121b$ and has the value $v_\theta(r_{\max}) \approx 0.638\Gamma/(2\pi b)$. The vorticity distribution associated with (2.46) is $\zeta(r) = [\Gamma/(\pi b^2)]\exp(-r^2/b^2)$. Then, for $\partial v_\theta/\partial r < 0$, the filamentation time corresponding to the Okubo-Weiss criterion is

$$\tau_{\text{fil}}(r) = \frac{2\pi b^2}{\Gamma}\left(\frac{r}{b}\right)^2\left(1 - e^{-r^2/b^2}\right)^{-1/2}\left[1 - \left(1 + \frac{2r^2}{b^2}\right)e^{-r^2/b^2}\right]^{-1/2} \tag{2.47}$$

With the choice $\Gamma/(2\pi) = 7.5 \times 10^5$ m^2 s^{-1}, Fig. 2.2 illustrates $v_\theta(r)$ and $\tau_{\text{fil}}(r)$ for various values of b. The values of b represent a tropical storm ($b = 20$ km) and category 1-5 (Saffir-Simpson scale) hurricanes (i.e., $b = 13.0$, 10.2, 8.5, 7.4, 6.3 km, respectively). Decreasing b increases the maximum tangential wind and decreases the radius of maximum wind. The sequence of curves in Fig. 2.2 can be interpreted as typical profiles that occur during intensification from a tropical storm to a category 5 hurricane. The filamentation times shown in Fig. 2.2b are defined in the region where $\partial v_\theta/\partial r < 0$. As r approaches the radius of maximum wind from the right, the filamentation time approaches infinity for each value of b. As r increases, all curves asymptotically approach one another and increase as r^2 [i.e., with the same far-field behavior as the Rankine vortex (2.44)]. The $\tau_{\text{fil}}(r)$ curve for the tropical storm lies above τ_{conv}. However, as the idealized Gaussian cyclone becomes stronger, the filamentation time dips well below τ_{conv} and the region affected by potentially detrimental strain grows. Within the rapid filamentation zone, patches of anomalous vorticity are expected to quickly filament into arbitrarily thin strip and subsequently disappear in the presence of diffusion.

Considering the axisymmetric Hua-Klein criterion (2.33), which is equal to the

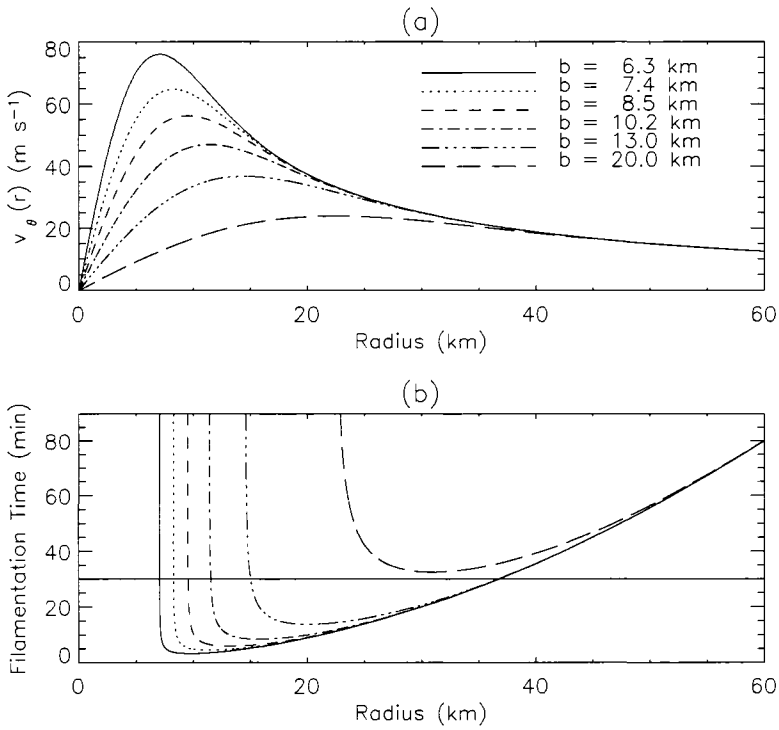

Figure 2.2: (a) Radial profiles of $v_\theta(r)$ as given in (2.46) for six different values of the parameter b. (b) Corresponding radial profiles of $\tau_{\rm fil}(r)$ as given in (2.47). The filamentation times $\tau_{\rm fil}(r)$ are plotted only in strain-dominated regions, where $S_n^2 + S_s^2 - \zeta^2 > 0$.

square root of (v_θ/r) $(v_\theta/r - 2\ \partial v_\theta/\partial r)$, the filamentation time associated with the Gaussian vortex is

$$\tau_{\rm fil}(r) = \frac{2\pi b^2}{\Gamma}\left(\frac{r}{b}\right)^2\left(1-e^{-r^2/b^2}\right)^{-1/2}\left[3-\left(3+\frac{2r^2}{b^2}\right)e^{-r^2/b^2}\right]^{-1/2}. \qquad (2.48)$$

Figure 2.3b displays the above filamentation times. Note that the ordinate of $\tau_{\rm fil}$ covers a smaller range than in Fig. 2.2. Once again, the Hua-Klein criterion produces substantially smaller filamentation times for all Gaussian vortices. Moreover, the weaker tropical storm also produces a notable rapid filamentation zone according to the operational $\tau_{\rm fil}$ threshold of 30 min. Because of nonlocal effects related to the pressure Hessian, the rapid filamentation zone extends within the radius of maximum wind (RMW).

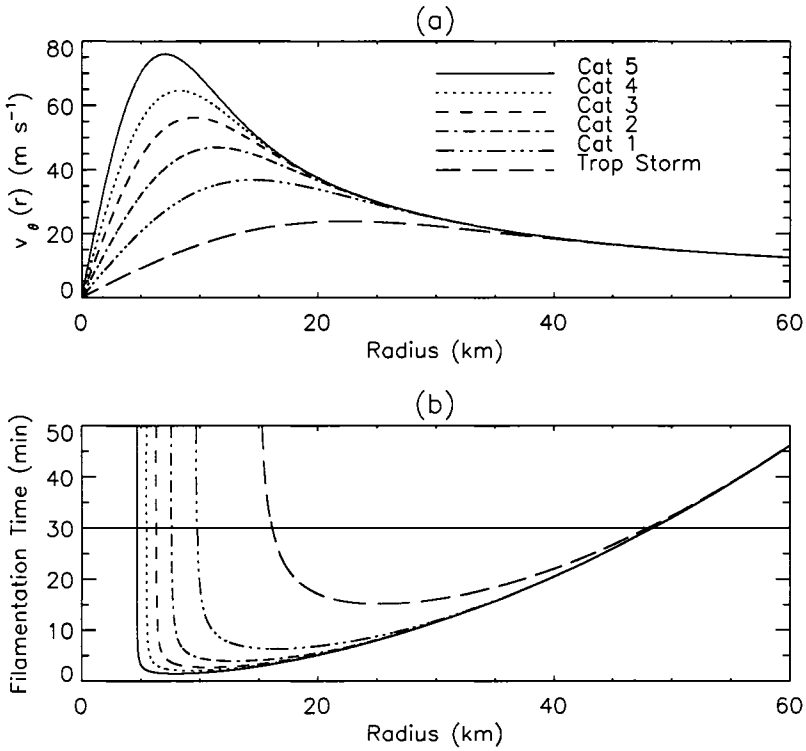

Figure 2.3: (a) Radial profiles of $v_\theta(r)$ as given in (2.46) for six different values of the parameter b. (b) Corresponding radial profiles of $\tau_{\rm fil}(r)$ according to the Hau-Klein criterion (2.48). The filamentation times $\tau_{\rm fil}(r)$ are plotted only where (v_θ/r) $(v_\theta/r - 2\ \partial v_\theta/\partial r) > 0$.

In real TCs, tangential wind profiles possess baroclinic structure. Specifically,

the strength of the tangential wind decreases with height. Assuming an axisymmetric vortex without a transverse circulation, filamentation times can be computed using (2.33). As one example, we reconsider the Gaussian vortex given in (2.46). Demanding Gaussian decay of the tangential winds with height, we have the following vortex structure:

$$v_\theta(r,z) = \frac{\Gamma}{2\pi r}\left(1 - e^{-r^2/b^2}\right) e^{-z^2/z_o^2}. \tag{2.49}$$

Using the parameters $b = 6.3$ km, $z_o = 15$ km, and $\Gamma/(2\pi) = 7.5 \times 10^5$ m^2 s^{-1}, Fig. 2.4 depicts (2.49) and the associated filamentation times, τ_{fil}, using the axisymmetric Hua-Klein criterion (2.49). In accordance to the vertical decay in v_θ, τ_{fil} also decreases in height. Nonetheless, the depth and width of the rapid filamentation zone ($\tau_{\text{fil}} < 30$ min) is significant. Thus, horizontal strain immediately outside of the vorticity core of a baroclinic vortex will act upon the entire depth of convective clouds.

As a final example of rapid filamentation zones in axisymmetric TCs, we consider an idealized TC-like vortex with a secondary eye wall. This profile is an approximation of Hurricane Gilbert (1988) on 14 September (c.f., Rozoff et al., 2006). We let the tangential wind for our parameterized TC with concentric eyewalls be

$$v_\theta(r) = \begin{cases} v_1(r/r_1) & \text{if } 0 \le r < r_1 \\ v_1(r_1/r)^{0.5} & \text{if } r_1 \le r < r_2 \\ [v_2(r_3 - r) + v_3(r - r_2)](r_3 - r_2)^{-1} & \text{if } r_2 \le r < r_3 \\ v_3(r_3/r)^{0.4} & \text{if } r \ge r_3, \end{cases} \tag{2.50}$$

where $r_1 = 10$ km, $r_2 = 50$ km, $r_3 = 60$ km, $v_1 = 70$ m s^{-1}, $v_2 = v_1(r_1/r_2)^{0.5}$, and $v_3 = 50$ m s^{-1}. The $r^{-0.5}$ wind structure in the moat is representative of decay in the tangential wind profiles outside of the RMW of typical TCs (Mallen et al., 2005). We note $\zeta^2 > S_n^2 + S_s^2$ in the regions $0 \le r < r_1$ and $r_2 < r < r_3$ because $dv_\theta/dr > 0$ and $v_\theta > 0$ in these regions. However, $S_n^2 + S_s^2 > \zeta^2$ in the regions $r_1 < r < r_2$ and $r > r_3$. Then, using the Okubo-Weiss criterion, the filamentation time corresponding

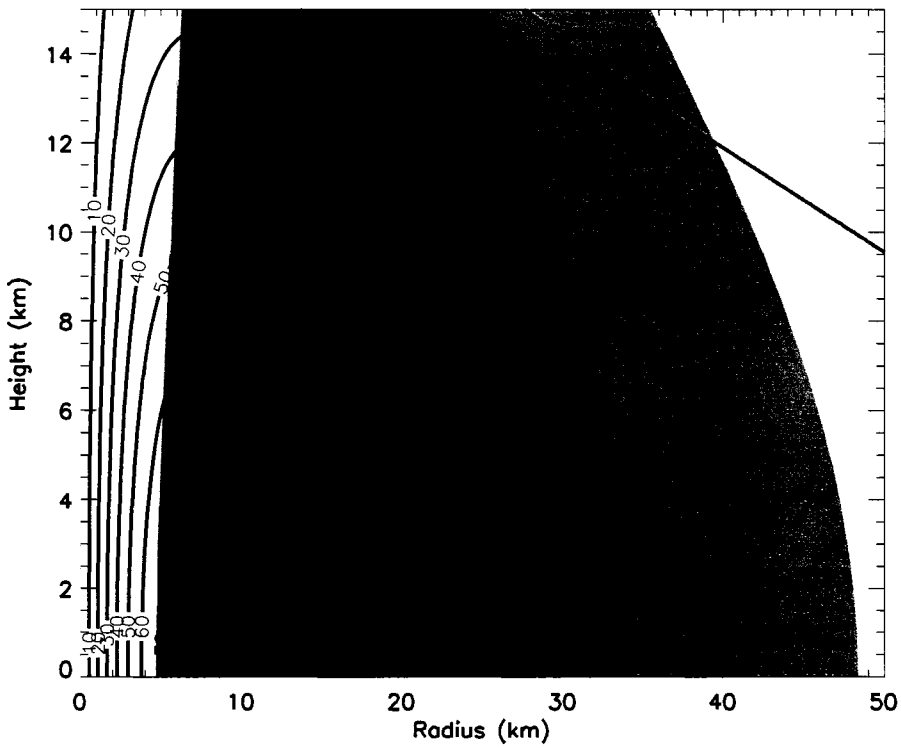

Figure 2.4: Radial-vertical distribution of $v_\theta(r, z)$ (contoured) as given in (2.49) for $b =$ 6.3 km and $z_o = 15$ km and corresponding Hua-Klein filamentation times (shaded), where the shaded regions are separated by filamentation times of 30, 15, 7.5, and 2.5 min, with darker shadings representing the smallest times.

to (2.50) is

$$\tau_{\text{fil}} = \begin{cases} (0.5)^{-1/2}(r_1/v_1)(r/r_1)^{1.5} & \text{if } r_1 < r < r_2 \\ (0.4)^{-1/2}(r_3/v_3)(r/r_3)^{1.4} & \text{if } r > r_3. \end{cases} \tag{2.51}$$

Both (2.50) and (2.51) are presented in Fig. 2.5. In the region between 10 and 43 km and the region just outside 60 km the filamentation times are less than 30 min. The effect of the secondary eye wall region is to provide a haven of rotation-dominated flow. Immediately outside of the secondary eyewall, the filamentation time is close to 30 min.

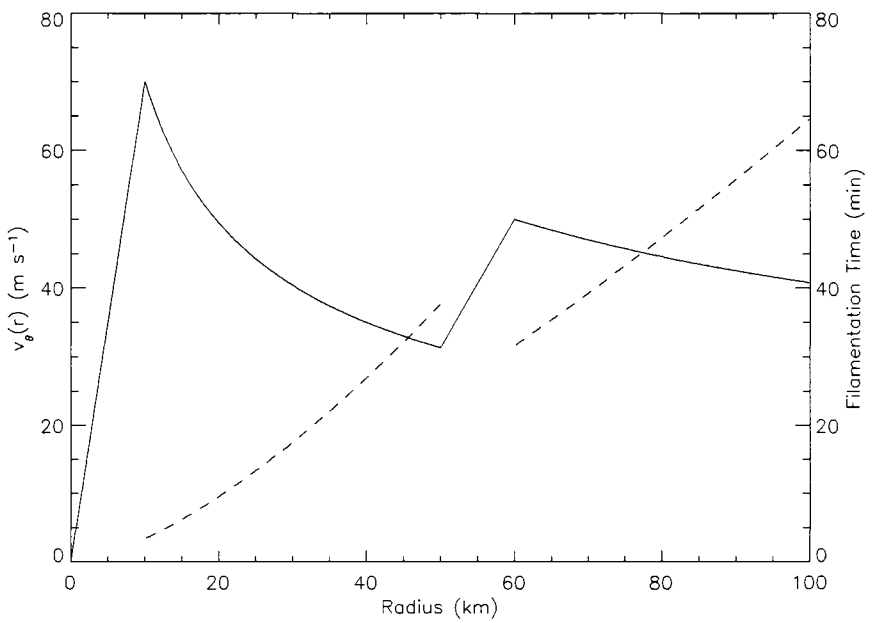

Figure 2.5: An idealized vortex with a secondary eye wall. The solid curve is $v_\theta(r)$ as given by (2.50), and the dashed curve is the filamentation time $\tau_{\text{fil}}(r)$, as given by (2.51). The filamentation time is plotted only in the regions where $S_n^2 + S_s^2 - \zeta^2 > 0$.

The Hua-Klein filamentation time associated with Fig. 2.50 is plotted in Fig. 2.6. Noting the change in scale on the τ_{fil} axis, the Hua-Klein filamentation time is considerably smaller than estimated by the Okubo-Weiss criterion. Moreover, a substantial rapid filamentation zone now exists outside of the secondary wind maximum according to the more accurate stirring criterion.

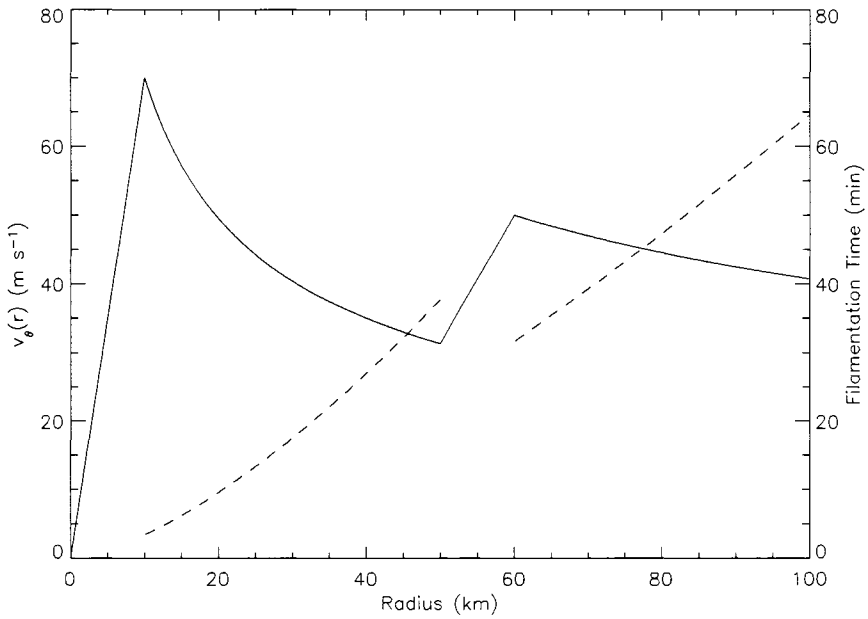

Figure 2.6: An idealized vortex with a secondary eye wall. The solid curve is $v_\theta(r)$ as given by (2.50) and the dashed curve is the filamentation time $\tau_{\text{fil}}(r)$, as given by (2.51). The filamentation time is plotted only in the regions where $(v_\theta/r)\ (v_\theta/r - 2\ \partial v_\theta/\partial r) > 0$.

2.3.2 *Two-dimensional numerical examples*

To further explore rapid filamentation, we perform numerical integrations of the nondivergent barotropic model. A pseudo-spectral version of (2.15) and (2.16) described in Schubert et al. (1999) is run incorporating a diffusion term on the right-hand side of (2.15), equal to $\nu\nabla^2\zeta$, to damp out accumulation of enstrophy at the highest wavenumbers.

At this point, we revisit the Gaussian vortex example considered in (2.46). The initial condition consists of a circular patch of high vorticity embedded within a stirred vorticity field biased toward cyclonic vorticity. Our experiments contain some anticyclonic vorticity in them, which is typically observed in small patches near strong convection in real TCs. The precise mathematical form of the initial condition is

$$\zeta(x,y,0) = \zeta_0 + \frac{\Gamma}{\pi b^2} e^{-r^2/b^2} + \zeta_{\text{turb}}(x,y) \begin{cases} 1 & \text{if } 0 \le r < r_1 \\ S[(r-r_1)/(r_2-r_1)] & \text{if } r_1 \le r < r_2 \\ 0 & \text{if } r_2 \le r, \end{cases} \quad (2.52)$$

where $r = (x^2 + y^2)^{1/2}$. With periodic boundary conditions, zero net circulation for the entire domain is desired, yet the two final terms on the right-hand side of (2.52) yield nonzero circulation. Therefore, ζ_0 in (2.52) is not a specified constant and is obtained from the circulation constraint $\int\int \zeta(x,y,0)dxdy = 0$. The second term on the right-hand side of (2.52) is the term for the Gaussian vortex. The constant Γ controls the amplitude of the vorticity in the Gaussian vortex and the constant parameter b governs the shape of the vortex profile with respect to r. Finally, the last term represents the stirred field of vorticity; $S(s) = 1 - 3s^2 + 2s^3$ is the basic cubic Hermite shape function satisfying $S(0) = 1$, $S(1) = 0$, and $S'(0) = S'(1) = 0$. The function $S(s)$ and the constants r_1 and r_2 control the size of the stirred vorticity disk. Here, S smoothly damps the turbulent vorticity amplitudes to zero between r_1

and r_2. The surrounding turbulent vorticity field is given by

$$\zeta_{\text{turb}}(x,y) = \sum_{k=-k_{\max}}^{k_{\max}} \sum_{l=-l_{\max}}^{l_{\max}} \zeta_{k,l} e^{i(2\pi/L)(kx+ly)}. \tag{2.53}$$

In (2.53), L is the domain size, $\zeta_{0,0}$ is a specified constant that determines the cyclonic bias of the surrounding turbulent vorticity field, and

$$\zeta_{k,l} = \hat{\zeta} e^{iR_{k,l}} \begin{cases} 0 & \text{if } 0 \le \kappa < \kappa_1 \\ S[(\kappa_2 - \kappa)/(\kappa_2 - \kappa_1)] & \text{if } \kappa_1 \le \kappa < \kappa_2 \\ 1 & \text{if } \kappa_2 \le \kappa < \kappa_3 \\ S[(\kappa - \kappa_3)/(\kappa_4 - \kappa_3)] & \text{if } \kappa_3 \le \kappa < \kappa_4 \\ 0 & \text{if } \kappa \ge \kappa_4, \end{cases} \tag{2.54}$$

with $\kappa = (k^2 + l^2)^{1/2}$ the total wavenumber, $\hat{\zeta}$ the amplitude of the turbulent vorticity fluctuations, and $R_{k,l}$ random numbers between zero and 2π. The constant specified wavenumbers κ_1, κ_2, κ_3, and κ_4 determine the spatial scales of the random vorticity elements in the stirred vorticity field.

In our experiments, we specify $\Gamma = 2\pi(7.5 \times 10^5)$ m^2 s^{-1}, $r_1 = 120$ km, $r_2 = 130$ km, $\kappa_1 = 0$, $\kappa_2 = 15$, $\kappa_3 = 30$, $\kappa_4 = 45$, $\zeta_{0,0} = 1 \times 10^{-4}$ s^{-1}, $\hat{\zeta} = 1.5 \times 10^{-5}$ s^{-1}, and run six experiments for the six values of b given in Figure 2.2. The horizontal scale of 600 km/κ is associated with the total wavenumber κ, so that the range of turbulence wavenumbers $0 \le \kappa \le 45$ corresponds to horizontal scales greater than 13 km. Most of the random vorticity elements have a scale between 20 and 40 km. These random elements can be interpreted as a result of vorticity generation by small groups of irregularly spaced cumulonimbus clouds. Tropical Rainfall Measuring Mission (TRMM) data show such scales are common in tropical convection near intensifying storms. Figure 2.7 shows the spatial distribution of the stirred vorticity field [i.e., the last term on the right-hand side of (2.52)].

The numerical integration of (2.52) is accomplished using 1024 × 1024 equally spaced collocation points on a doubly periodic domain size of 600 km × 600 km. The

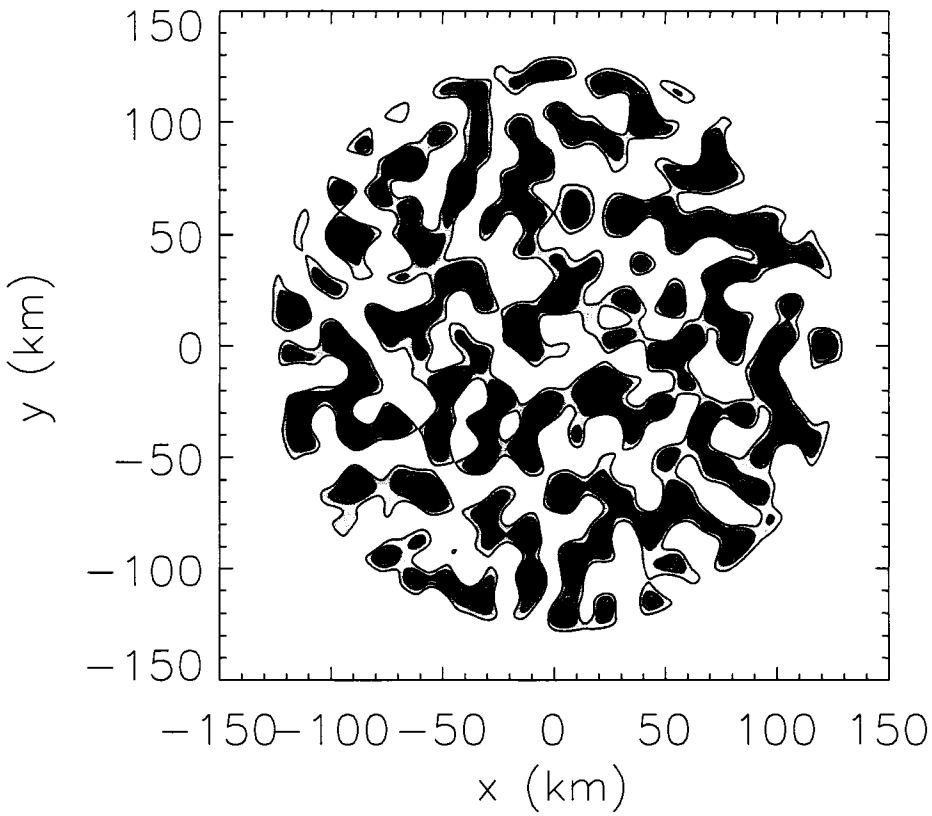

Figure 2.7: Contour plot of the turbulent part of the initial vorticity field [i.e., the last term on the right-hand side of (2.52)]. The model domain encompasses 600 km × 600 km but only the inner 300 km × 300 km is displayed. Vorticity contours are at 1.0×10^{-4}, 5.0×10^{-4}, and 10.0×10^{-4} s^{-1}, with the darkest shading representing the highest values of vorticity.

model is run with a dealiased calculation of the quadratic nonlinear terms in (2.15), resulting in 340 × 340 Fourier modes. The wavelength of the highest Fourier mode is 1.76 km. Time integration is accomplished via the standard fourth-order Runge-Kutta scheme, with a time step of 5 s. The value of viscosity is $\nu = 20$ m^2 s^{-1}. This yields a $1/e$ damping time of 1.1 h for all modes having total wavenumber 340.

To illustrate the effects of rapid filamentation, Fig. 2.8 shows the vorticity distribution at t = 30 min for each of the experiments described above. Regions of enhanced vorticity in Fig. 2.7 undergo merger events and simultaneously experience filamentation. In all of the panels in Fig. 2.8, the distribution of turbulent vorticity outside a radius of 40 km from the center are similar for all Gaussian vortex centers because the filamentation time is similar for all of the vortices at larger radii (c.f., Figs. 2.2, 2.3). On the other hand, it is clear from Fig. 2.8 that stronger vortices more readily deform and filament the turbulent vorticity at smaller radii. For the strongest Gaussian vortices, continued evolution of the vorticity field eventually leads to the formation of a weakly positive vorticity ring outside of a smooth, axisymmetric moat containing slightly negative vorticity.

Another interesting example of vortex interaction is the evolution of two initially circular vortex patches in close proximity. One patch with small area, but large vorticity can be considered the TC core. The other patch containing the larger area, but weaker vorticity, can be interpreted as a nearby weak storm or merely enhanced vorticity generated by surrounding asymmetric convection. Prieto et al. (2003) and Kuo et al. (2004) performed numerous barotropic model experiments with a range of vortex area ratios, peak vorticity ratios, and separation distances. They classified the resulting interactions using the scheme devised by Dritschel and Waugh (1992). An important conclusion of these papers is that one way to produce a halo of enhanced vorticity around an intense vortex is through a binary interaction in which the weaker vortex is completely strained out. This mode of interaction is most likely to occur

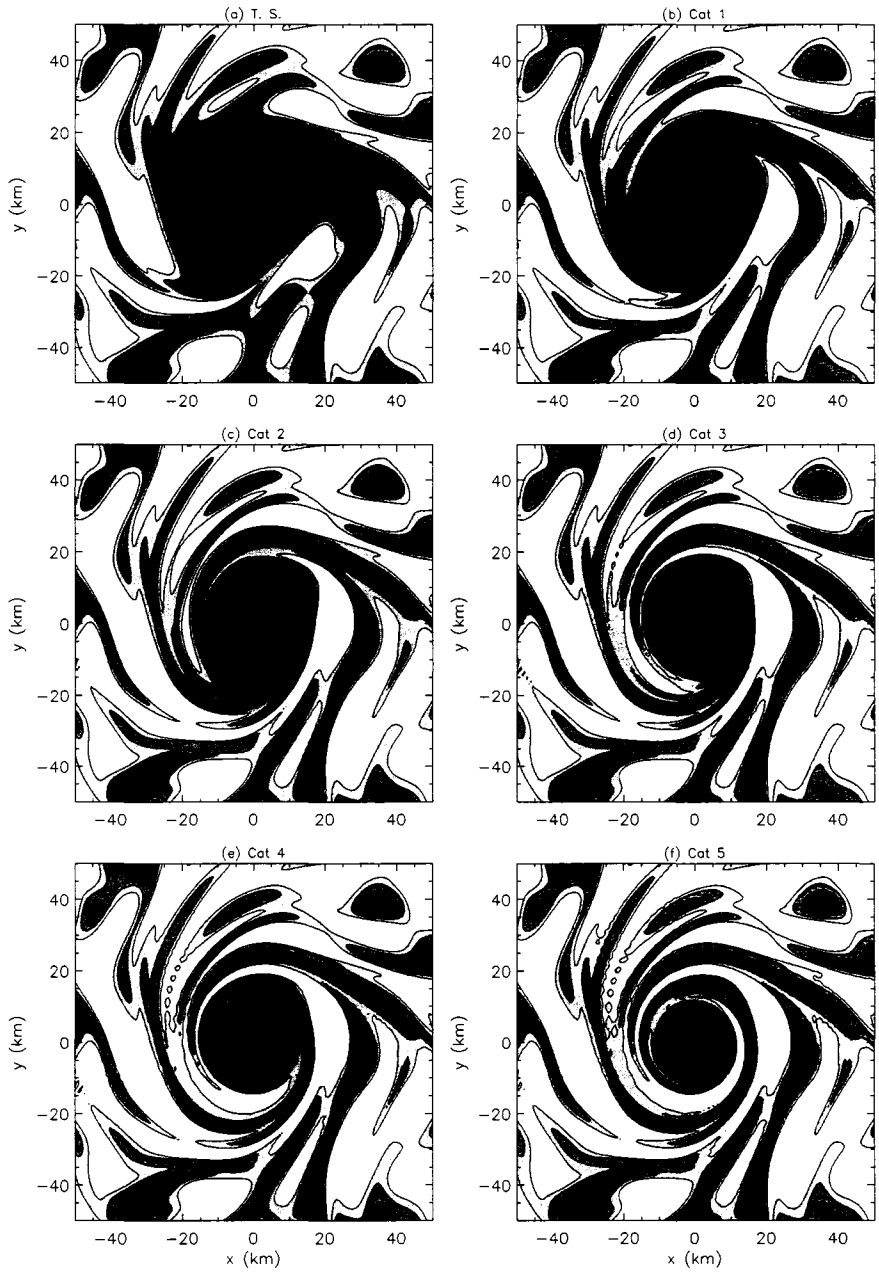

Figure 2.8: Barotropic model results at $t = 30$ min for the six Gaussian vortices with a superimposed turbulent vorticity field. Vorticity is plotted for (a) $b = 20$ km (tropical storm), (b) $b = 13$ km (category 1 TC), (c) $b = 10.2$ km (category 2), (d) $b = 8.5$ km (category 3), (e) $b = 7.4$ km (category 4), and (f) $b = 6.3$ km (category 5). Shaded regions are separated by the vorticity contours 1×10^{-4}, 5×10^{-4}, 10×10^{-4}, and 100×10^{-4} s^{-1}. The darker shading represents higher values of vorticity. The model domain encompasses 600 km $\times$ 600 km, but only the inner 100 km $\times$ 100 km is displayed.

when the peak vorticity in the strong vortex is at least 5 times the amount of vorticity in the weak vortex (Kuo et al. 2004, Fig. 10). To what extent vortex interactions are really relevant in concentric eyewall formation remains controversial at this time.

To understand how rapid filamentation zones evolve during these vortex interactions, we perform the experiments depicted in Fig. 2.9. In this experiment the domain size is 200 km $\times$ 200 km and the value of viscosity is set to $\nu = 6.5$ m^2 s^{-1}. The initial condition consists of two circular vortex patches with sharp edges. Initially, the small patch has a nearly uniform vorticity equal to 2.5×10^{-3} s^{-1} and a radius of 30 km. The distance between the vorticity centers is 50 km. As shown in Fig. 2.9a, the large, weak vortex has been completely strained out after 3 h. At 6 h (not shown), the tightly wound portion of the spiral acquires an irregular shape while the outer portion becomes very thin. By 12 h, the central core of high vorticity is surrounded by a moat of low vorticity, which in turn is surrounded by a ring of enhanced vorticity from the original weak vortex. Outside the halo is a region of irregular vorticity, associated with dissipating thin spiral bands.

The corresponding distributions of the filamentation time, computed from (2.39), are shown in Fig. 2.9b. The white areas represent regions where the flow is rotation-dominated. There are five shades of gray, indicating filamentation times $\tau_{\text{fil}} < 2.5$ min (black region), $2.5 < \tau_{\text{fil}} < 7.5$ min, $7.5 < \tau_{\text{fil}} < 15$ min, $15 < \tau_{\text{fil}} < 30$ min, and $30 < \tau_{\text{fil}}$ (lightest gray region). It is evident the Hua-Klein rapid filamentation zone encompasses much of the domain shown in Fig 2.9b. Consistent with the earlier analytical examples, the τ_{fil} is smaller here than those computed using the Okubo-Weiss criterion (c.f., Rozoff et al., 2006).

Can a strong vortex imposed upon a stirred field of vorticity lead to a halo of vorticity similar to those formed in the experiments of Kuo et al. (2004)? To find out, we revisit the unforced, turbulent vorticity experiments described earlier. In this case, however, the second Gaussian term in (2.52) is replaced with $\zeta_{\max} S[(r - r_3)/(r_4 - r_3)]$,

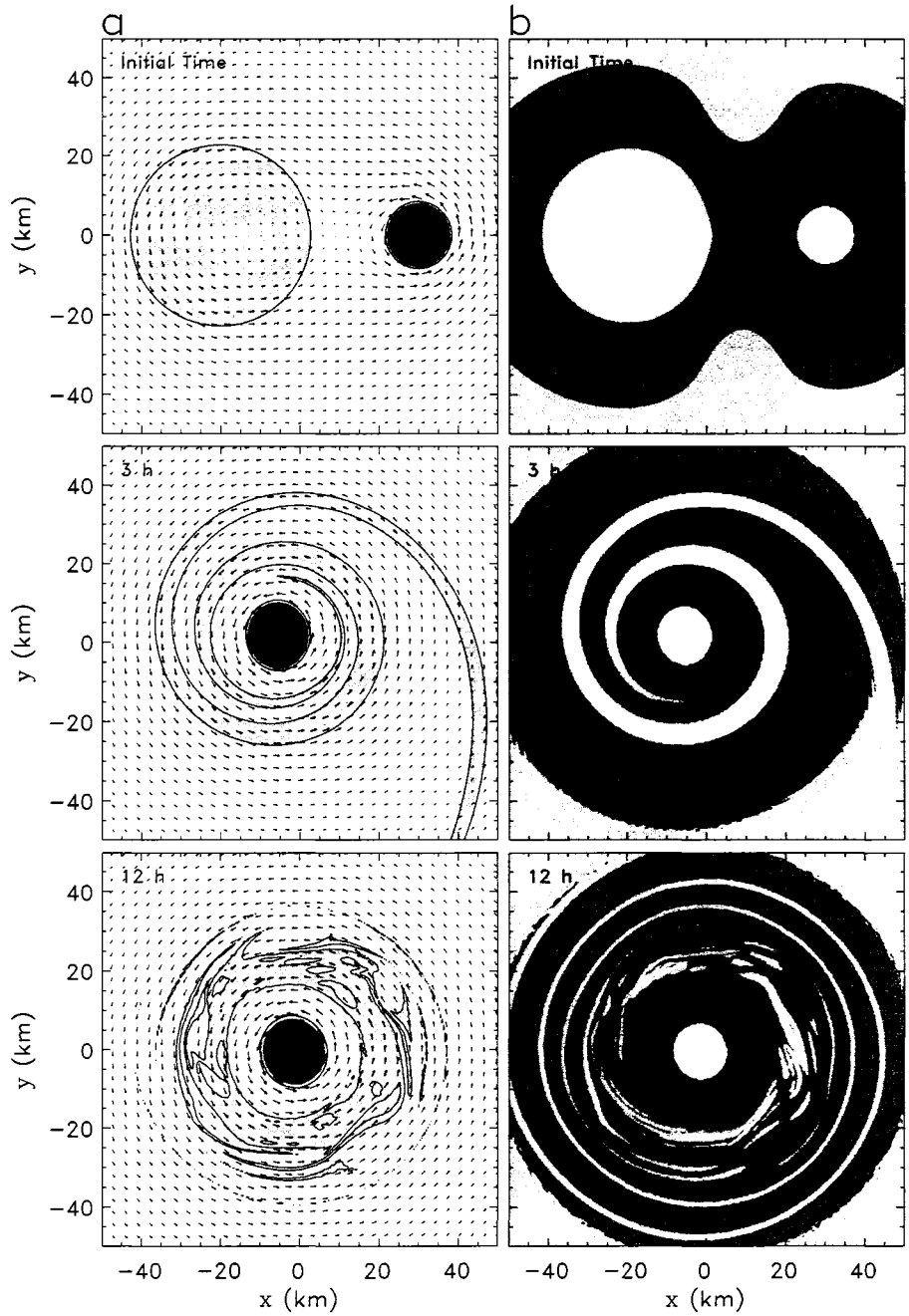

Figure 2.9: (a) Vorticity contour plots and horizontal wind vectors for the binary interaction experiment are shown in the left three panels. The contours are 10×10^{-4}, 50×10^{-4}, and 100×10^{-4} s^{-1}, with darker shading denoting higher vorticity. (b) Corresponding Hua-Klein filamentation times for the panels to the left. The shaded regions are separated by filamentation times of 30, 15, 7.5, and 2.5 min, with darker shadings representing the smallest times. The model domain encompasses 200 km × 200 km, but only the inner 100 km × 100 km is displayed.

where $S(x)$ is the basic cubic Hermite shape function defined earlier and r_3 and r_4 are defined to approximate an intense TC. The central vortex structure is approximately a Rankine vortex. Choosing $\zeta_{max} = 6.5 \times 10^{-3}$ s^{-1}, the central vortex represents a Category 5 hurricane with maximum tangential winds of 75.5 m s^{-1} near $r = 25$ km. The simulation is carried out as before, except this time, it continues for 48 h.

The results of this experiment are illustrated in Fig. 2.10. Figure 2.10a indicates how the strong vortex dominates the field of turbulent vorticity and preferentially filaments the vorticity closer to the core at 9 h, clearing much of the vorticity within a 30-km-wide annulus surrounding the core. Vorticity patches in the far-field are less dominated by the core's motions, and therefore, these patches have pronounced interaction with neighboring vorticity patches. Nevertheless, the far-field is still strain-dominated on average and after 45 h the outer vorticity patches have strained out, leaving a fairly axisymmetric vorticity distribution about the TC's center. Smaller filamentation times near the core, as presented in Fig. 2.10b, eliminate vorticity around the core. We note the small, white vortex features in the filamentation time fields are anticyclones generated by the randomly distributed anticyclonic vorticity in the initial condition. A halo of weak vorticity begins at a radius of about 70 km from the center. The magnitude of this vorticity halo is an order of magnitude less than the halo resulting from the binary interaction experiment. Initially, the magnitude of the central core is only one order greater than the surrounding, stirred vorticity field. Yet, after about 45 h, the difference is two orders of magnitude. Diffusion acts aggressively on the scales of the small vorticity elements because of the del-squared diffusion term in the numerical vorticity equation. At the same time, the larger and uniform vorticity patch seen in the binary vortex experiment remains relatively protected from diffusion. Forced experiments may alleviate the diffusive behavior in the organization of a stirred field of vorticity in the vicinity of a strong, central vortex.

As a set of final examples, we consider rapid filamentation zones during mesovor-

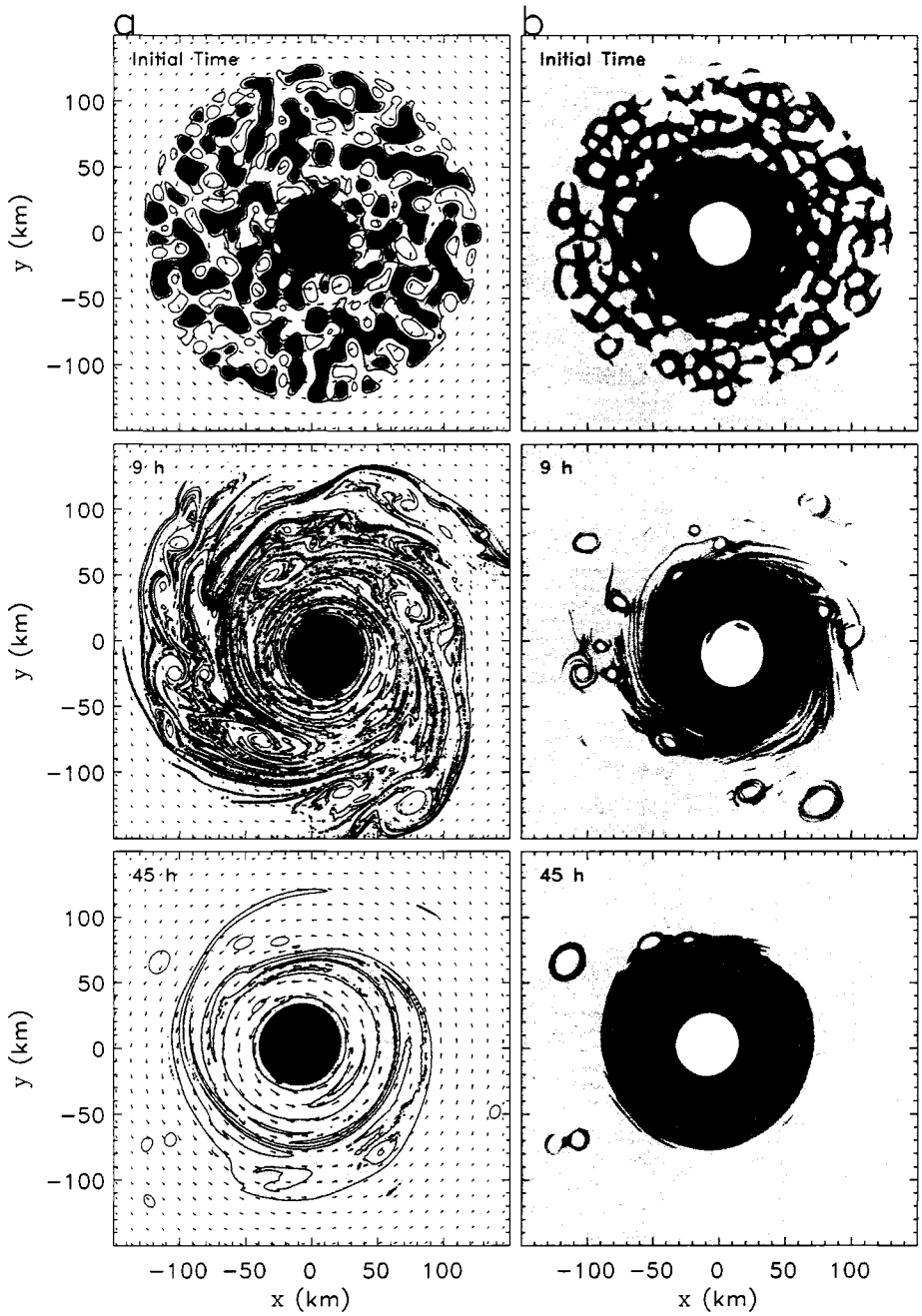

Figure 2.10: (a) Vorticity contour plots and horizontal wind vectors. The contours are 1×10^{-4}, 5×10^{-4}, 10×10^{-4}, and 50×10^{-4} s^{-1}. Darker shading denotes higher vorticity. (b) Corresponding Hua-Klein filamentation times for the panels to the left. The shaded regions are separated by filamentation times of 30, 15, 7.5, and 2.5 min, with darker shadings representing the smallest times. The model domain encompasses 600 km $\times$ 600 km, but only the inner 300 km $\times$ 300 km is displayed.

tex formation. Observed flows in intensifying TCs sometimes resemble an idealized circular flow with a thin annular ring of enhanced vorticity (Kossin and Eastin, 2001). These flows tend to be barotropically unstable and, in certain circumstances, the annulus of vorticity breaks down into a number of mesovortices (Kossin and Schubert, 2001, hereafter KS01; Montgomery et al., 2002; Kossin et al., 2002). The experiments presented in Figs. 2.11 and 2.12 provide some insight into the evolution of rapid filamentation zones during mesovortex formation. The initial condition for these two experiments is $\zeta(r,\theta,t=0)=\bar{\zeta}(r)+\zeta'(r,\theta)$, where $\zeta'(r,\theta)$ is a small perturbation of the axisymmetric vorticity field

$$\bar{\zeta}(r)=\begin{cases}\zeta_1 & \text{if } 0\le r<r_1,\\ \zeta_1 S[(r-r_1)/(r_2-r_1)]+\zeta_2 S[(r_2-r)/(r_2-r_1)] & \text{if } r_1\le r<r_2,\\ \zeta_2 S[(r-r_2)/(r_3-r_2)]+\zeta_1 S[(r_3-r)/(r_3-r_2)] & \text{if } r_2\le r<r_3,\\ \zeta_1 & \text{if } r_3\le r<r_4,\\ \zeta_1 S[(r-r_4)/(r_5-r_4)]+\zeta_3 S[(r_5-r)/(r_5-r_4)] & \text{if } r_4\le r<r_5,\\ \zeta_3 & \text{if } r\ge r_5,\end{cases} \tag{2.55}$$

where r_1, r_2, r_3, r_4, r_5, ζ_1, ζ_2, and ζ_3, are independently specified quantities, and $S(s)$ is the same basic cubic Hermite shape function used in (2.52). This initial condition is identical to that imposed in experiments 1 and 6 in KS01. In the present simulations, a slightly different initial random noise perturbation $\zeta'(r,\theta)$ is chosen, but as in KS01, it is also one percent of the local vorticity. A comparison of our results with KS01 reveals the sensitivity of our simulations to subtle changes in initial conditions—an expected result considering the chaotic behavior of this simple nonlinear system. For the results shown in Figs. 2.11 and 2.12, the nondivergent barotropic model is integrated with 512 × 512 collocation points on a 200 km × 200 km domain. The viscosity is chosen as $\nu=5\mathrm{m}^2\ \mathrm{s}^{-1}$ and the time step is 5 s.

For the experiment shown in Fig. 2.11, (r_1, r_2, r_3, r_4, r_5) = (13, 15, 17, 35,

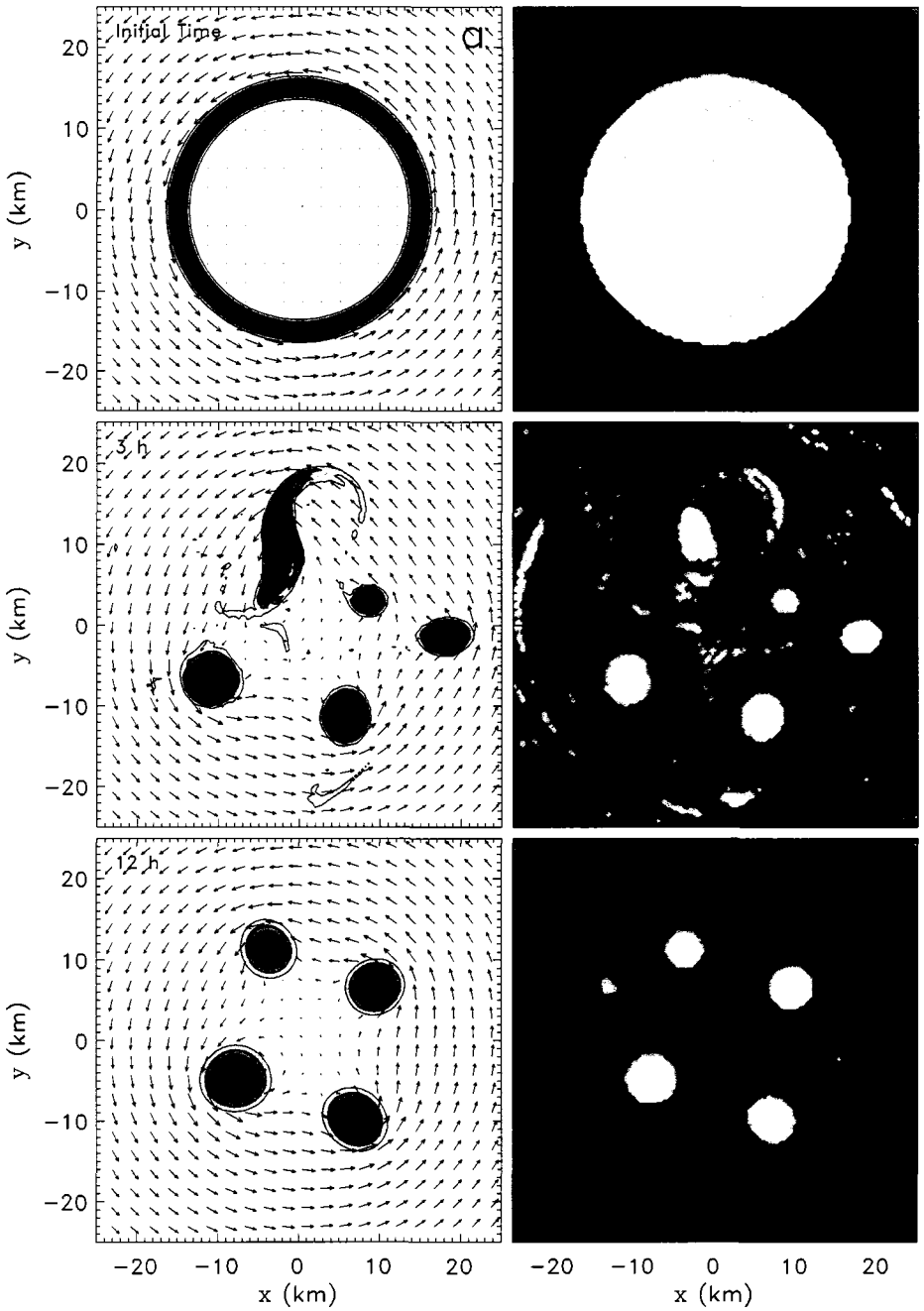

Figure 2.11: (a) Vorticity contour plots and horizontal wind vectors for the first thin annular vorticity ring experiment. The contours begin at 5×10^{-3} s^{-1} and they are incremented at 5×10^{-3} s^{-1}. Darker shading denotes higher vorticity. (b) Corresponding Hua-Klein filamentation times for the panels to the left. The shaded regions are separated by filamentation times of 30, 15, 7.5 and 2.5 min, with darker shadings representing the smallest times. The model domain encompasses 200 km $\times$ 200 km, but only the inner 50 km $\times$ 50 km is displayed.

45) km and $(\zeta_1, \zeta_2, \zeta_3) = (1.02, 248.52, -1.48) \times 10^{-4} s^{-1}$, which yield a vortex with maximum tangential winds of 45 m s^{-1} at $r = 17$ km. Figure 2.11a depicts vorticity and the associated wind field. The thin annulus experiences exponential growth of small initial perturbations, resulting in numerous mesovortices. Many have merged by $t = 3$ h. Eventually, a quasi-stable configuration of four vortices materializes. The prominent features include the persistent general cyclonic flow surrounding an interior region of relatively calm winds. This flow steers the mesovortices in a cyclonic orbit. Each mesovortex induces an asymmetric circulation about itself.

Given the particular wind distributions associated with the mesovortex configurations, it is valuable to study where rapid filamentation occurs. Figure 2.11b displays filamentation times for the corresponding plots on the left-hand side. Gibbs phenomena are noticeable in these experiments, especially in the τ_{fil} field. Rapid filamentation always occurs on the outside regions of all areas of higher vorticity. Consequently, it would be difficult to maintain weaker vorticity and convective clouds around each mesovortex perimeter.

For the second experiment, shown in Fig. 2.12, $(r_1, r_2, r_3, r_4, r_5) = (30, 30.5, 32, 40, 45)$ km and $(\zeta_1, \zeta_2, \zeta_3) = (1.02, 395.0, -1.48) \times 10^{-4}$ s^{-1}. This configuration result in an initial maximum wind of 74 m s^{-1} around $r = 33$ km. In Fig. 2.12a, vorticity and wind fields are plotted every 3 h starting at 12 h. As in KS01, six mesovortices maintain themselves in an alternating wavenumber-5 or -6 pattern as one vortex migrates in and out of the center. As in the previous mesovortices experiment, winds are relatively calm in the center and stronger and more cyclonic on the outskirts. Each mesovortex also induces its own asymmetric circulation about itself. In this case, however, when one vortex periodically migrates into the interior region, an asymmetric pattern in the wind field appears and stronger winds are carried into the eye.

Figure 2.12b shows filamentation times corresponding with Fig. 2.12a. Again,

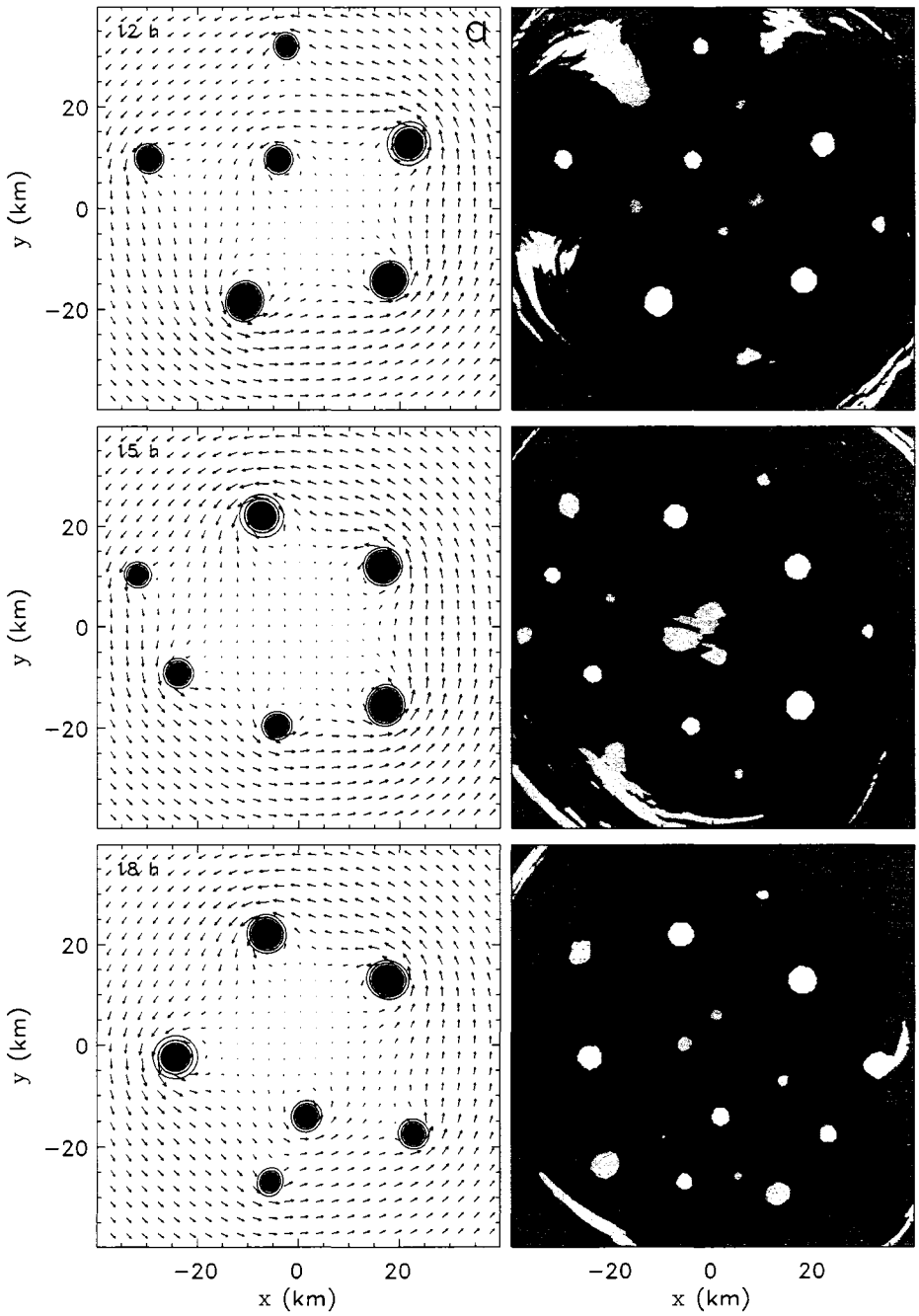

Figure 2.12: (a) Vorticity contour plots and horizontal wind vectors for the second thin annular vorticity ring experiment. The contours begin at 5×10^{-3} s^{-1} and they are incremented at 5×10^{-3} s^{-1}. Darker shading denotes higher vorticity. (b) Corresponding Hua-Klein filamentation times for the panels to the left. The shaded regions are separated by filamentation times of 30, 15, 7.5, and 2.5 min, with darker shadings representing the smallest times. The model domain encompasses 200 km $\times$ 200 km, but only the inner 80 km $\times$ 80 km is displayed.

each mesovortex is surrounded by a region of enhanced filamentation. In nature, if 2D nondivergent barotropic dynamics were the only physics at work, given sufficiently thin rings of vorticity, similar vorticity structures would be found in real TC inner cores.

2.4 Summary and discussion

We have defined a rapid filamentation zone as a region within strain-dominated flow where $\tau_{\text{fil}} < \tau_{\text{conv}}$, where τ_{fil} is based on either the Okubo-Weiss (Rozoff et al., 2006) or the Hau-Klein eigenvalues describing the evolution of tracer gradients, and where the moist convective overturning time is $\tau_{\text{conv}} = 30$ min. Rapid filamentation zones are less likely in weak tropical disturbances, but in stronger, symmetric TCs they tend to occupy an annular region 20–40 km wide just outside the radius of maximum wind. In symmetric, intense hurricanes with a secondary eyewall, another (but narrower) rapid filamentation zone can occur just outside of the secondary wind maximum. If mesovortices form and the storm becomes asymmetric, the rapid filamentation zone can extend into the eye, where strain rates can be very large despite weak flow. In the binary interactions, it appears the rapid filamentation zone outside of a more intense vortex can influence the development of a moat.

The Hua-Klein revisions to the Rozoff et al. (2006) results suggest that the 30 min criterion for a rapid filamentation zone in Rozoff et al. (2006) may coincide less well with the observed size of a moat. Also, considering the rotation of the strain axes (i.e., Lapeyre et al., 1999; Klein et al., 2000), tracer gradients are expected to grow algebraically in axisymmetric vortices. Because strain is implicit in the time coordinate of the Lapeyre et al. (1999) criterion, their method still predicts enhanced rapid filamentation in regions of stronger strain. Moreover, the nonlinear and nonpassive character of convective plumes are anticipated to substantially modify the properties of simple 2D rapid filamentation zones. Future theoretical work should

extend these concepts to vortices with convection.

We hypothesized that both subsidence and rapid filamentation are relevant in the formation and maintenance of a moat. The relative importance of these two processes cannot be determined from the simple 2D arguments presented in this chapter. As a result, observations and 3D modeling efforts, which include both idealized convection simulations and analysis of concentric eyewall formation in full hurricanes, are needed to uncover the most important factors related to the formation of a moat. Furthermore, these efforts can help us develop a more accurate definition of a rapid filamentation zone. In the following chapters, we perform observational case studies and idealized cloud modeling experiments to help address these ambiguities.

Chapter 3

MOAT OBSERVATIONS

3.1 Introductory remarks

We recall from Chapter 2 that rapid filamentation zones surround sufficiently strong vortices. In this chapter, we will see that moats in concentric eyewall situations exist in rapid filamentation zones. Nonetheless, the detrimental effects of horizontal deformation on convective clouds may be irrelevant when moat regions cannot produce convective clouds due to sufficiently strong stable stratification.

Rozoff et al. (2006) pointed out that Hurricane Gilbert's (1988) moat formed in a region of rapid filamentation. Still, their observational analysis, in agreement with the lower-level moat subsidence diagnosed by Dodge et al. (1999), also showed that Gilbert's moat exhibited sizeable dewpoint depressions at 700 hPa. We will now briefly review their results before considering more recent observational case studies.

Figures 3.1a,d (from Rozoff et al., 2006) show 133- and 123-min composites of the horizontal radar reflectivity for Hurricane Gilbert on 13 and 14 September 1988. These radar composites were originally presented in Black and Willoughby (1992). On 13 September, Gilbert attained its peak intensity with a central minimum sea level pressure (MSLP) at 888 hPa. During this period, Gilbert contained a very compact eyewall between 8 and 20 km from the center. On 14 September, Gilbert's MSLP rose to 895 hPa as an ERC was underway. In Fig. 3.1b, the inner eyewall is still between 8- and 20-km radius and the new outer eyewall is located between 55- and 100-km radius. In between these regions, a 35-km weak-echo moat is indicated in the radar

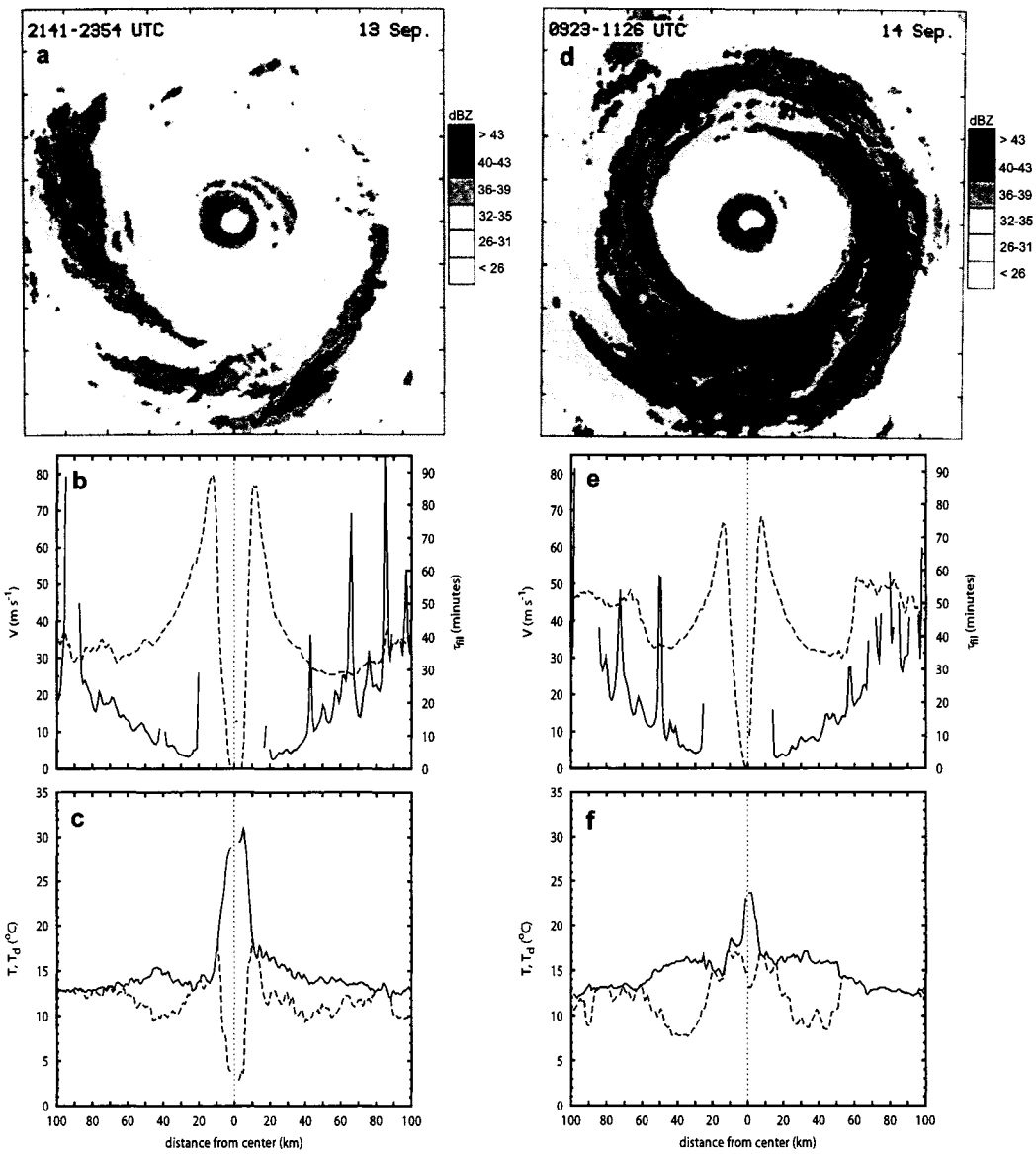

Figure 3.1: Composite horizontal reflectivity of Hurricane Gilbert for (a) 2141–2354 UTC 13 September 1988 and (d) 0923–1126 UTC 14 September 1988. (The radar composites are from Black and Willoughby 1992.) Also, flight-level tangential wind, v_θ (dashed), and filamentation time (solid), as computed from (2.23), for the 700-hPa flights for (b) 13 and (e) 14 September; corresponding temperature and dewpoint temperature along the same flight track on (c) 13 and (f) 14 September. This figure is taken from Rozoff et al. (2006).

composite. Figures 3.1b,e are radial profiles of flight-level (700 hPa) tangential wind, v_θ, from the National Oceanographic and Atmospheric Administration (NOAA) WP-3D aircraft during the period of the composites. On 13 September, the v_θ maximum was 75–80 m s^{-1} at 10-km radius. Note that v_θ increased slightly with radius near the outer convective bands as seen in Fig. 3.1a. By 14 September, the inner v_θ maximum was 66–69 m s^{-1} at 10-km radius, while the outer v_θ maximum was 49–52 m s^{-1} at 61–67-km radius.

Corresponding to Gilbert's forming moat on 13 September and its mature moat on 14 September, there were marked dewpoint depressions throughout this observational period. On 13 September, the 700 hPa dewpoint depressions in the moat reached 5°C (Fig. 3.1c). On 14 September, the dewpoint depressions in the moat were approximately 8°C (Fig. 3.1f), which are nearly as large as in the eye. Moreover, this region warmed by 1–2°C from 13 to 14 September. These dewpoint depressions are consistent with the subsidence analyzed in Dodge et al. (1999) in the lower troposphere of Gilbert's moat on 14 September.

Rozoff et al. (2006) also computed Okubo-Weiss filamentation times, $\tau_{\text{fil}}(r)$, for Gilbert's v_θ data using Eq. (2.23) (Figs. 3.1b,e). Within Gilbert's forming moat, small filamentation times were achieved on both 13 and 14 September, with τ_{fil} reaching as low as 5 min closer to the primary eyewall. This rapid filamentation zone remained nearly unchanged between the two days even though the inner eyewall begins to decay on 14 September.

While the case study presented in Rozoff et al. (2006) demonstrated that the moat region, both during its formation and mature stage, can have sizeable dewpoint depressions, it is unclear whether such moat thermodynamic conditions are ubiquitous to all concentric eyewall situations. Thus, we present additional data from two recent, well-observed Atlantic hurricanes to show the existence of variability in the low-level thermodynamic conditions during various stages of an ERC. Both dropsondes and

flight-level data are incorporated to get a broad picture of the low-level troposphere. Although deep-layer profiles are rare for the inner-core region of a hurricane due to flight-level restrictions, the low-level profiles at least suggest when and where surface-based convection is thermodynamically unlikely.

3.2 Methodology

In our current study, two intense, Atlantic hurricanes with concentric ERCs are analyzed: Hurricanes Frances on 30 August 2004 and Rita on 21 and 22 September 2005. Observations from Frances were taken in a mature concentric eyewall situation and Rita had relatively dense observational coverage at times before, during, and after concentric eyewall formation. On 30 August 2004, flight-level and dropsonde data from the NOAA 43 WP-3D (N43) aircraft and operational flight-level data from a United States Air Force (USAF) C130 aircraft are incorporated into analysis of a mature moat. For Rita, data from two NOAA P3s (N42 and N43), the USAF C130, and a Naval Research Laboratory (NRL) P3 are used to study thermodynamic and kinematic conditions during the different stages of Rita's concentric eyewall formation.

Quality-checked 1-s flight-level temperature, dewpoint, and wind data from NOAA P3s, provided by NOAA's Hurricane Research Division (HRD), are used to obtain radial profiles and composites of kinematic and thermodynamic data. Instrument wetting errors are common in saturated regions (Zipser et al., 1981; Eastin et al., 2002). Therefore, the correction technique described in Zipser et al. (1981) is made. Namely, in regions where dewpoint temperature exceeds the temperature, the temperature is re-adjusted to the average of the temperature and dewpoint and this air is assumed to be saturated. Analysis by Eastin et al. (2002) suggests that this method reduces temperature and water vapor errors from 1.0°C and 0.8 g kg^{-1} to 0.6°C and 0.5 g kg^{-1}.

National Center for Atmospheric Research (NCAR) Global Positioning System

(GPS) dropwindsondes (dropsondes) were released from all available P3s, USAF, and NOAA G-IV (relatively far from the moat region) for both Frances and Rita. Dropsondes provide pressure, temperature, relative humidity, and horizontal wind speed at 2 Hz resolution in time. These dropsondes fall at about 12–15 m s^{-1} in the lower troposphere and data are sampled approximately at 5 m intervals in the vertical direction. Typical errors for pressure, temperature, humidity, and wind speed are within 1.0 hPa, 0.2 °C, 5 %, and 2 m s^{-1}, respectively (Hock and Franklin, 1999). For Frances, all sondes were edited with NCAR's Atmospheric Sounding Processing Environment (ASPEN) software, while ASPEN and HRD Editsonde software were used for dropsondes in Rita (HRD provided processed NOAA P3 data for this research). The ASPEN software was applied to raw data to compare with HRD's software and the results are qualitatively similar.

All data are transformed into a cyclindrical coordinate system centered around the geographical center of the moving TC. Consequently, accurate determination of the storm center is needed as a function of time for each storm. We utilize an optimal, although somewhat subjective, selection of successive centers deduced from the method of Willoughby and Chelmow (1982). The Willoughby and Chelmow method incorporates both pressure and wind information from the flight-level data and has an estimated accuracy within about 3 km. All flight tracks that passed near the center of a given storm are used to obtain as many center estimates as possible. All center estimates are corrected for the storm motion so that our centers are "storm relative." NOAA's "best track" data are utilized to bracket center estimates obtained during an intensive observational period (IOP). Linear interpolation is used between the selected center fixes as it produces more realistic center fixes than cubic splines interpolation. It worth pointing out that the Willoughby and Chelmow (1982) method assumes a radially monotonic pressure and wind variation within the radius of maximum winds, while many TCs exhibit mesovortices (e.g., Schubert et al., 1999) within

their eyes and attendant multiple pressure and wind minima (Kossin and Schubert, 2001). Mesovortices, which often have scales of 5 to 20 km, can lead to center errors of the same order in the Willoughby and Chelmow (1982) method. This may explain why some of our discarded center estimates produce poor results in the coordinate transformation.

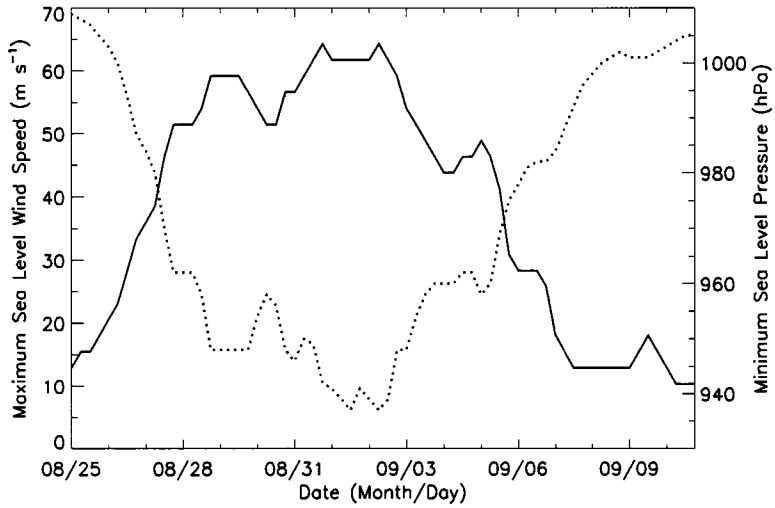

Figure 3.2: National Hurricane Center Best Track intensity for Hurricane Frances (2004) throughout the storm's lifecycle. The maximum surface wind speed (m s^{-1}) is depicted by the solid curve, while the minimum sea-level central pressure (hPa) is represented by the dotted line.

The primary goal of this chapter is to explore the thermodynamic and kinematic variability outside of a primary eyewall before and during ERCs. One way to address this goal is to construct composite azimuthal means (e.g., Bell and Montgomery, 2007) using an objective interpolation technique (e.g., Barnes, 1973). A certain amount of error is inherent in such a technique, especially because of the steady-state and axisymmetric assumptions that are typically made. In addition, small-scale variability can be easily averaged out. Furthermore, due to the relatively few dropsondes in the moat and pre-moat regions in Rita, and especially in Frances, it is instructive to analyze individual dropsondes and radially composited dropsondes over shorter time periods to investigate the lower tropospheric thermodynamic structure of the moat

and pre-moat environments. In order to resolve the radial kinematic gradients of interest, the high-resolution radial data from aircraft is more amenable for accurate radial derivative estimation than estimating radial derivatives from radially sparse dropsonde data. The most preferable 3D kinematic analysis derives from the dual-Doppler capabilities of the P3 aircraft, which is currently underway for Rita (Michael Bell, personal communication).

Both individual and composited flight-legs and dropsondes are presented in our analysis. Composites are constructed by averaging each flight-level data field or selected dropsonde data, $\eta(\xi)$, into bins in the coordinate ξ. (Here, ξ can represent radius or the pressure p.) Averaging data into each bin is done through a weighted mean,

$$\bar{\eta}(\xi_o) = \frac{\int_{\xi_o-\delta\xi}^{\xi_o+\delta\xi} \eta(\xi) K(\xi) d\xi}{\int_{\xi_o-\delta\xi}^{\xi_o+\delta\xi} K(\xi) d\xi}, \tag{3.1}$$

where ξ_o is the physical location of the given bin, $\delta\xi$ is a specified averaging interval, and the weight $K(\xi)$ is defined by

$$K(\xi) = \begin{cases} 0 & \text{if } \xi < \xi_o - \delta\xi, \\ (\xi - \xi_o + \delta\xi)/\delta\xi & \text{if } \xi_o - \delta\xi \le \xi < \xi_o, \\ (\xi_o - \xi + \delta\xi)/\delta\xi & \text{if } \xi_o \le \xi < \xi_o + \delta\xi, \\ 0 & \text{if } \xi \ge \xi_o + \delta\xi. \end{cases} \tag{3.2}$$

Variance is calculated via the function

$$V[\eta(\xi_o)] = \frac{\int_{\xi_o-\delta\xi}^{\xi_o+\delta\xi} (\eta(\xi) - \bar{\eta}(\xi))^2 K(\xi) d\xi}{\int_{\xi_o-\delta\xi}^{\xi_o+\delta\xi} K(\xi) d\xi}. \tag{3.3}$$

For the v_θ composites (i.e., $\eta = v_\theta$), filamentation times, τ_{fil}, are computed from these composites using the formula given by (2.33). Such fields are still noisy, so a box car filter is applied to τ_{fil} over an interval of three gridpoints.

3.3 Hurricane Frances (2004) observations

Hurricane Frances (2004) was an intense TC that reached a peak intensity of category 4 on the Saffir-Simpson Hurricane Scale. Frances arose from a tropical wave that moved off the western coast of Africa on 21 August (Beven, 2004). The National Hurricane Center (NHC) classified this system as a tropical depression at 0000 UTC 25 August. The subsequent intensity timeline for Frances is shown in Fig. 3.2, which has been adapted from the NHC Best Track data archive. By 1800 UTC on 28 August, the storm had quickly intensified and attained an estimated maximum surface wind speed of 60 m s^{-1} and minimum sea-level pressure (MSLP) of 948 hPa. As Frances passed to the north of the Leeward and Virgin Islands on 30 August, the first of its three ERCs commenced, with concentric eyewalls clearly evident in the N43 aircraft radar and wind observations. During this ERC, the maximum surface wind speed decreased to 51 m s^{-1} and the minimum surface pressure rose to 958 hPa. As the initial, inner eyewall diminished and the outer eyewall contracted, the storm began its course toward its highest sustained surface wind speed of 64 m s^{-1} and lowest MSLP of 937 hPa on 31 August to 1 September. Thereafter, an environment of increasing vertical shear of the horizontal wind impeded the storm from regaining its previous maximum intensity, and the storm made landfall on the central, eastern coast of Florida around 0430 UTC 5 September as a Category 2 hurricane.

Figure 3.3 shows radar reflectivity and radial profiles of v_θ, temperature, and dewpoint temperature collected from the N43 during a 3.25 hour interval on 30 August. During this time period, Frances possessed concentric eyewalls, with a 100 km diameter outer eyewall and a 30 km diameter inner eyewall that became increasingly asymmetric in time (Figs. 3.3a,c,e). A consistent asymmetric structure also shows up in both the v_θ profiles (Figs. 3.3b,d,f) and the moat between concentric eyewalls. Dewpoint depressions as large as 6°C appeared in the northeast sector at 640 hPa (Fig. 3.3d), suggestive of enhanced subsidence there. The most striking aspects of

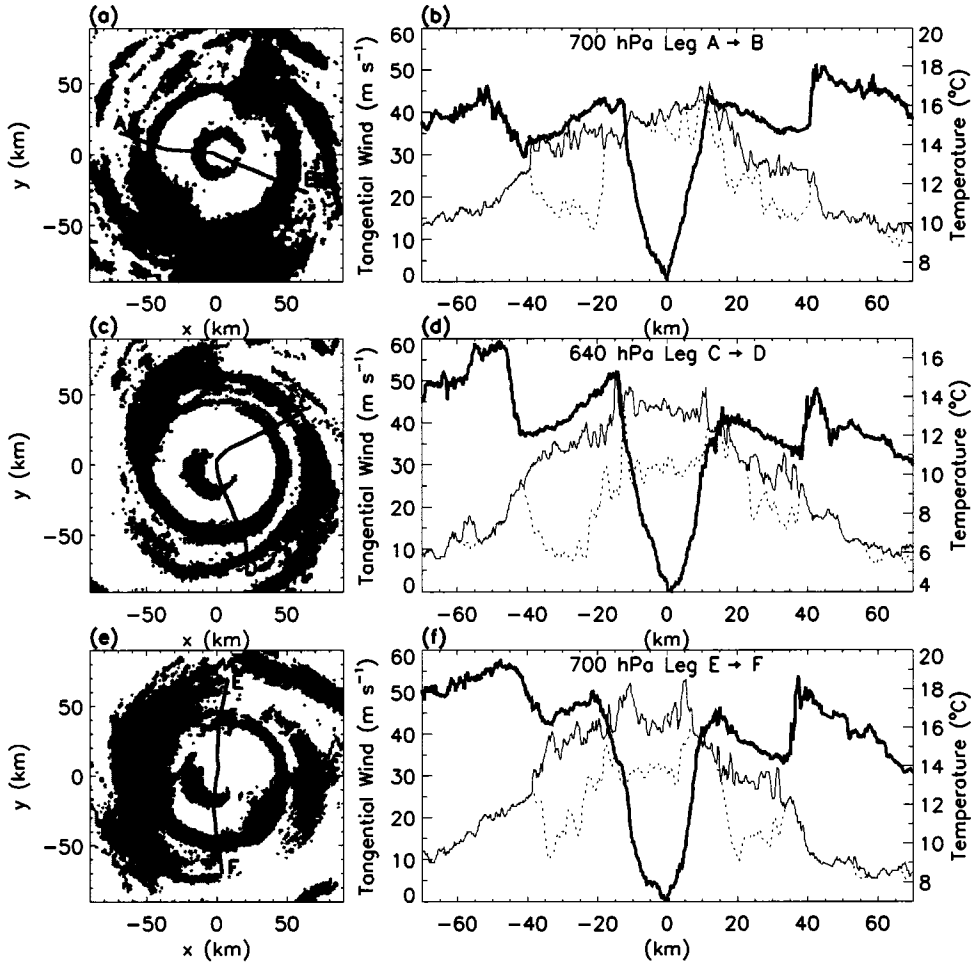

Figure 3.3: Composite radar reflectivity and radial profiles of flight-level tangential wind (m s^{-1}; thick solid), temperature (°C; thin solid), and dewpoint temperature (°C; dashed) for Hurricane Frances from 1804–1822 UTC (Leg A→B), 1924–1943 UTC (Leg C→D), and 2108–2126 UTC (Leg E→F) on 30 August 2004. The radar imagery incorporated into this figure was provided by HRD.

these observations are the warm-core structure and dewpoint depressions which encompassed the entire region inside the outer eyewall. Within the primary eyewall, particularly elevated temperatures were observed. In fact, the Leg E→F radial profile reveals a warm ring structure (Schubert et al., 2007) just inside the inner eyewall. Overall, these observations suggest that Frances was well into its ERC.

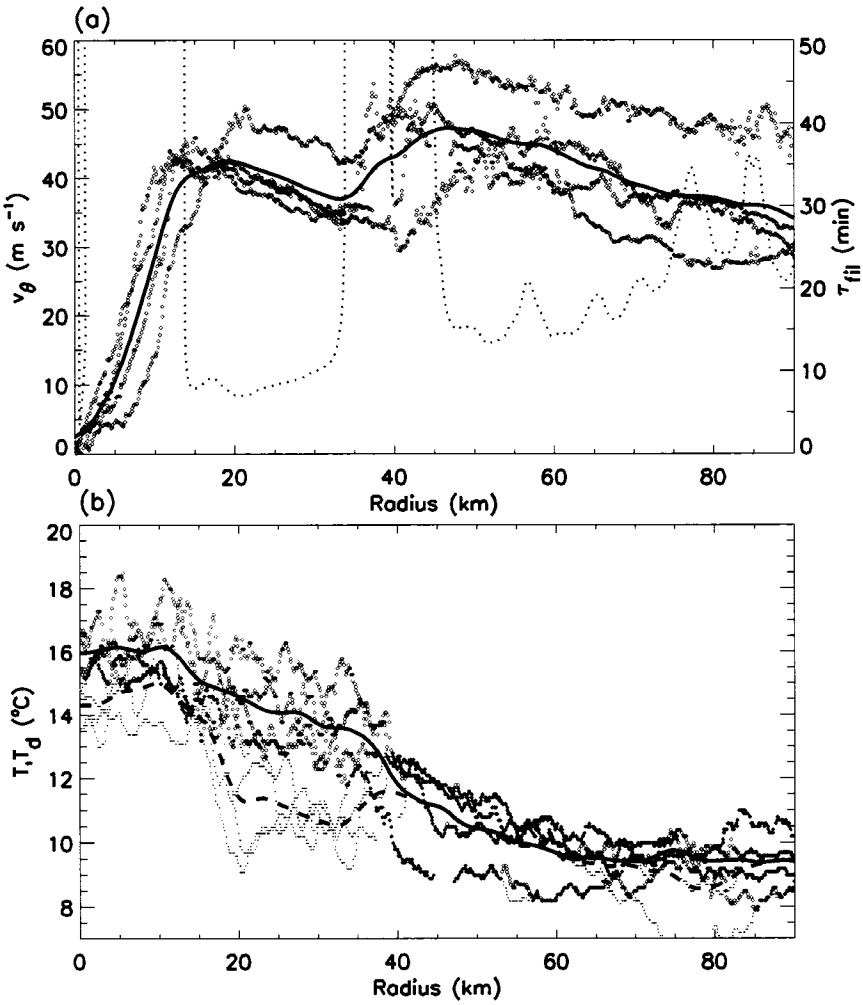

Figure 3.4: Hurricane Frances (2004) (a) composite radial profiles of 700 hPa flight-level tangential wind, v_θ (m s^{-1}; solid black), and individual v_θ observations (blue dots), and (b) 700 hPa composite temperature (°C; solid black) and individual temperature observations (red dots) and composite dewpoint temperature (°C; dashed black) and individual dewpoint measurements (green dots) on 30 August. In (a), the filamentation time (red dotted curves), τ_{fil}, is computed for the composite v_θ profile.

Figure 3.4 shows v_θ and temperature and dewpoint composites at 700 hPa.

These particular profiles are for the time periods of 1802–1824 UTC and 2105–2128 UTC, where data are gridded into Δr = 250 m intervals and an averaging window, 2 δr, of 6 km is chosen. Consistent with the individual passes, it is clear the secondary eyewall dominated in strength during this IOP (Fig. 3.4a). Asymmetries and the secondary eyewall's 5 km contraction create spread in the v_θ and temperature composites. For example, the average standard deviation of temperature is 5.9°C. Also, a rapid filamentation zone within the moat is associated with the v_θ profile in Fig. 3.4a) during this IOP, where the composite τ_{fil} reaches 10 min. Lower values of τ_{fil}, below 20 min, exist outside the secondary eyewall. In Fig. 3.4b, the composite temperatures and dewpoints reaffirm the eye-like warm core and enhanced dewpoint depressions inside the outer eyewall seen in the individual flight passes.

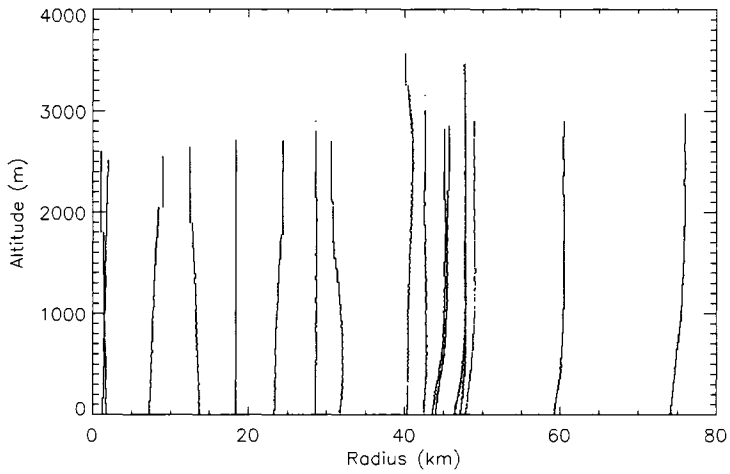

Figure 3.5: Dropsonde data points with respect to radius and height for the Hurricane Frances N43 IOP on 30 August 2004.

Nineteen dropsondes were successfully processed from the N43 Frances IOP on 30 August. However, as seen in Fig. 3.4, only three dropsondes were apparently dropped within the moat. Therefore, we do not attempt a composite sounding here. Individual dropsondes still show some variability in the lower tropospheric stability (Fig. 3.6). Dropsondes released between 1810 and 1816 UTC at radii of 24 and 29 km

(Fig. 3.6a,b), respectively, show eye-like profiles, with a temperature inversion and 4–5°C dewpoint depressions located above a moist boundary layer. The sounding in Fig. 3.6 does not contain positive available low-level buoyancy. (Here, buoyancy is proportional to $T - T_{\text{env}}$, where T and T_{env} are the temperatures of a hypothetical, lifted surface-based parcel and the local environmental temperature, respectively.) Despite what is likely a subsidence inversion, there is some available buoyancy in the sounding depicted in Fig. 3.6b. Another moat sounding (Fig. 3.6c), dropped around 2121 UTC at $r = 32$ km, is fairly moist, but provides little confidence in the likelihood of surface-based convection at that point in time.

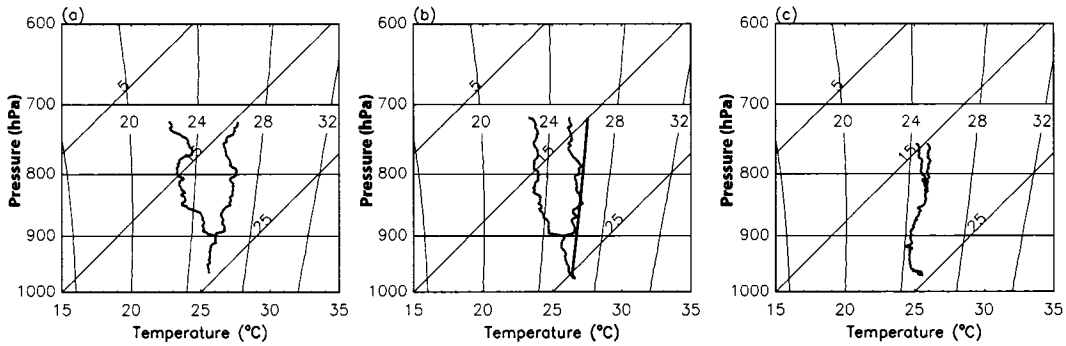

Figure 3.6: Individual dropsondes in the moat of Frances on 30 August 2004. The dropsondes are at about (a) $r = 24$ km (1810 UTC), (b) $r = 29$ km (1816 UTC), and (c) $r = 32$ km (2121 UTC). In (b), a hypothetical surface-based parcel path temperature profile is added to indicate available low-level buoyancy.

Overall, the low-level dropsondes and flight-level data in Hurricane Frances indicate marginal available low-level buoyancy. These thermodynamic conditions also coincide with a rapid filamentation zone. The individual dropsondes do not rule out the possibility of convection, but it is difficult to infer too much without full tropospheric profiles of temperature and dewpoint in the moat. Nonetheless, the moat of Frances presents a hostile environment for convective clouds. Since the IOP in Frances took place during a mature phase of an ERC with a well-established moat, it is desirable to have data before and during secondary eyewall formation. Such comprehensive data was collected in Hurricane Rita (2005)

3.4 Hurricane Rita (2005) observations

Hurricane Rita was just one of many powerful north Atlantic hurricanes in the anomalous 2005 hurricane season. Rita also had a well observed concentric eyewall formation thanks to the serendipitously timed field campaign, the Hurricane Rainband and Intensity Change Experiment (RAINEX) (Houze et al., 2006). Rita achieved the fourth lowest pressure ever recorded in the Atlantic with an MSLP of 895-hPa (Fig. 3.7). Rita began on 16–17 September as a westward moving wave from Africa that intersected a remnant cold front north of Puerto Rico (Knabb et al., 2006). The storm developed into a tropical depression by 0000 UTC 18 September over the northwestern Caribbean Sea. Just south of Florida on 1200 UTC 20 September, Rita became a hurricane and it rapidly intensified on its westward journey, especially as it traversed over the relatively deep, warm waters associated with the Loop Current in the eastern Gulf of Mexico. Rita strengthened to a Category 5 storm from its tropical storm status in less than 36 hours. When Rita reached its peak intensity of 80 m s^{-1} around 0300 UTC 22 September, signs of an ERC began to appear. After the commencement of Rita's eyewall cycle, the storm started weakening on 22 September. Increased environmental vertical shear of the horizontal wind and subsequent dry air interference with Rita prevented it from achieving its former Category 5 status again.

RAINEX was dedicated to observing rainbands and concentric eyewalls. As such, the large quantity of in situ flight data and dropsondes gathered in RAINEX allow for detailed examination of the thermodynamic and kinematic state of Rita's moat in various stages of development. In order to focus on the formation of a secondary eyewall and attendant moat, the following sections focus on 21 and 22 September 2005. On these two days, particularly on 21 September, vertical shear was less of a factor in the storm evolution and many of the changes in the storm were most likely related to internal dynamics and the storm's reaction to favorable atmospheric and oceanic conditions.

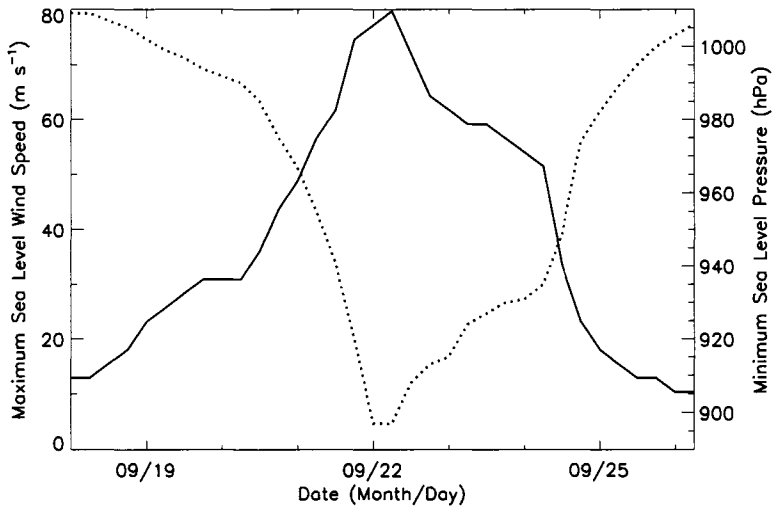

Figure 3.7: National Hurricane Center Best Track intensity for Hurricane Rita (2005) throughout the storm's lifecycle. The maximum surface wind speed (m s^{-1}) is depicted by the solid curve, while the minimum sea-level central pressure (hPa) is represented by the dotted line.

3.4.1 21 September 2005

In coordination with RAINEX, the N43, the NRL P3, and USAF aircraft gathered observations of Rita's core and rainbands on 21 September. The P3 aircraft collected Doppler radar data, in situ observations, and dropsondes, while the USAF aircraft collected flight-level and dropsonde data. On 21 September, Rita was rapidly intensifying toward its Category 5 intensity. A concentric eyewall was not yet clearly apparent during this particular RAINEX IOP.

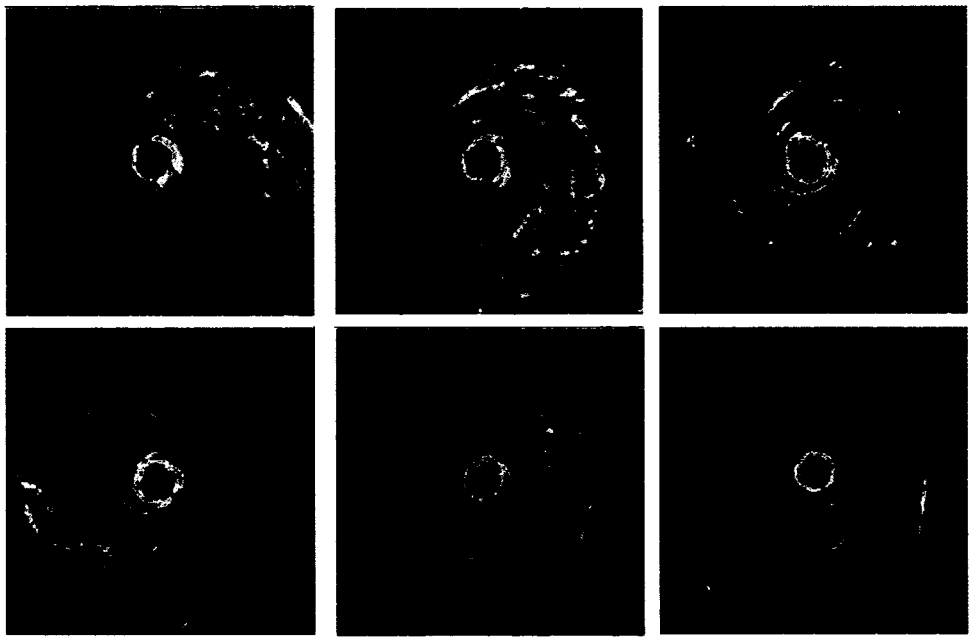

Figure 3.8: Individual N43 LF reflectivity (dBZ) sweeps during the RAINEX IOP on 21 September for (a) 1459 UTC, (b) 1510 UTC, (c) 1517 UTC, (d) 1538 UTC, (e) 1917 UTC, and (f) 1936 UTC. The grid box size is 360 × 360 km. Blue reflectivity colors span 20–25 dBZ, green is 25–30 dBZ, yellow is 30–35 dBZ, orange is 35–40 dBZ, and red is 40–45 dBZ. This imagery is provided from HRD.

Individual N43 lower fuselage (LF) radar reflectivity sweeps provide a qualitative description of Rita's structural evolution during the 21 September IOP. The LF radar's wavelength is 5.6 cm (5.3 GHz). The beamwidth is 1.1° in the horizontal and 4.1° in the vertical (Marks, 1985). The sweeps shown in Fig. 3.8 are over 30 s intervals and are presented in a storm relative sense. Stratiform precipitation is not

well detected within about 60 km of the P3. Hence, circular gray regions of "deleted" stratiform precipitation follow the airplane position in the individual sweeps, but major convective structures, such as spiral rainbands and the eyewall, are still captured. This artifact is a result of the 4.1° vertical angle of the radar beam missing the bright-band, which is above the N43 in these images. Thus, the apparent echo-free moat surrounding the eyewall in Figs. 3.8e,f is largely an artifact of the radar sweep missing stratiform precipitation.

Overall, Rita maintained a well-defined eyewall during the 21 September IOP (Fig. 3.8). Several stronger cells and polygonal features within the primary eyewall may indicate vigorous edge waves or even mesovortices (e.g., Figs. 3.8b,c,d). Small, tightly wound, spiral rainbands were common near the eyewall on 21 September, with marked, filamented rainbands detected around 1538 UTC and 1936 UTC. Some outer bands at about 100–115 km had a strong convective, cellular nature to them, especially during the beginning of the IOP. Consistent with the composite radar reflectivity of Gilbert on 13 September 1988 (e.g., Black and Willoughby 1992; Fig. 3.1a above), vigorous convective activity was somewhat limited between the primary eyewall and the outer convective bands throughout this IOP. Also, even though radar reflectivity was artificially suppressed in Figs. 3.8e,f, it is apparent, throughout the IOP, that as the P3 approached and left the center the areal average of reflectivity decreased in intensity to about 20–25 dBZ within the region just outside of the eyewall (figures not shown).

Figure 3.9 is a composite of v_θ measured from the N43 throughout its 21 September IOP. Here, we choose the same averaging windows used in Frances. The top panel of Fig. 3.9 shows observations at 640 hPa that were taken over the period of 1855–1956 UTC. The bottom panel presents data associated with the 700 hPa radial passes during an earlier time period of 1507–1616 UTC. Although there is some intrinsic error in the center finding routine (note the rather odd loops within Rita's eye), Rita was

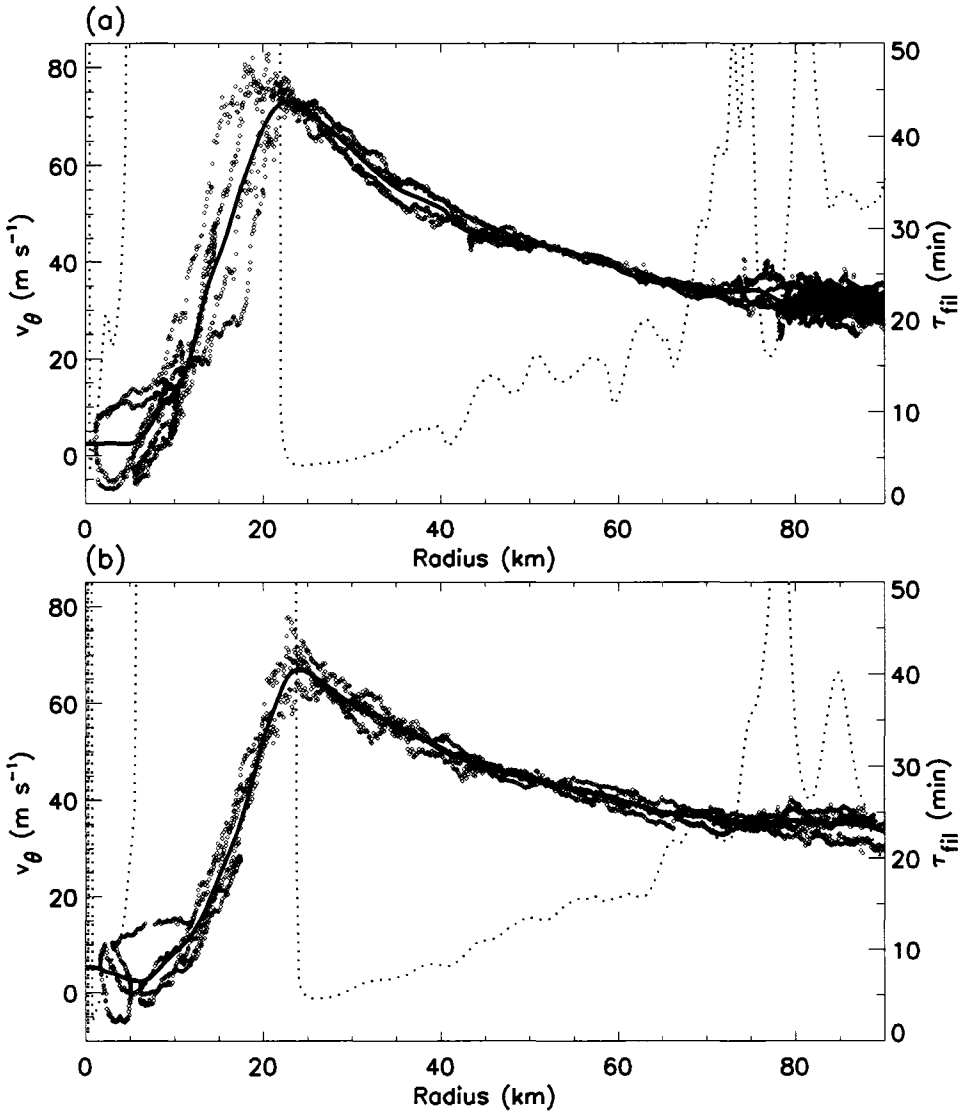

Figure 3.9: Hurricane Rita (2005) (a) composite radial profiles of flight-level tangential wind, v_θ (m s^{-1}; solid black), and individual v_θ observations (blue dots) at (a) 640 hPa (1855–1956 UTC), and (b) 700 hPa (1507–1616 UTC) on 21 September. Some measurements taken of rainbands over the period of 1647–1842 UTC appear at $r > 75$ km in the 640 hPa panel. The filamentation time (red dotted curves), $\tau_{\rm fil}$, is computed for each composite profile.

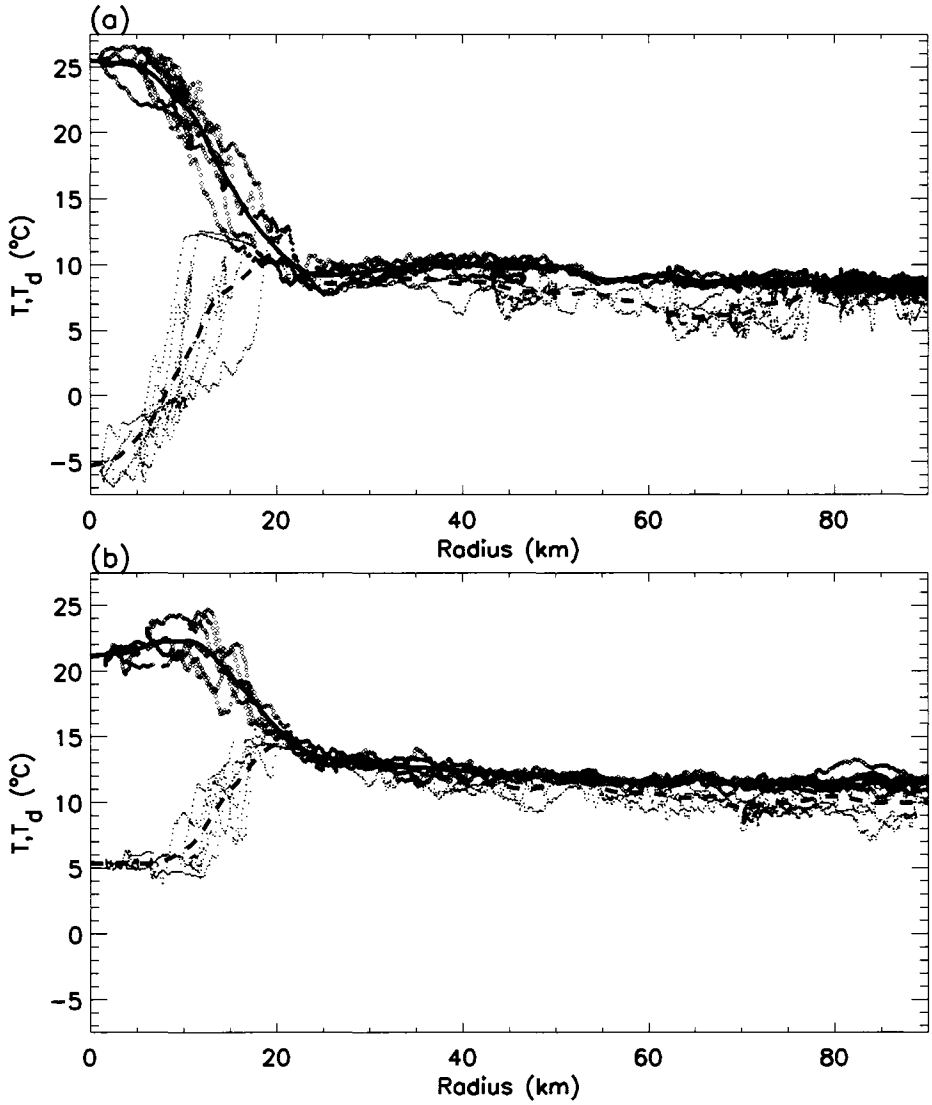

Figure 3.10: Hurricane Rita composite radial profiles of flight-level temperature, T (°C; solid black), and dewpoint, T_d (°C; dashed black) and individual temperature and dewpoint observations (red and green dots, respectively) at (a) 640 hPa (1855–1956 UTC) and at (b) 700 hPa (1507–1616 UTC) on 21 September 2005. Some rainband measurements collected over the period of 1647–1842 UTC appear in the 640 hPa panel at $r > 75$ km.

a remarkably axisymmetric hurricane. The composite structure shows a "U-shaped" profile within the eye, which is suggestive of depressed relative vorticity in the storm center relative to the eyewall. Moreover, there is an abrupt drop in v_θ outside of the radius of maximum winds. Such deformation leads to a rapid filamentation zone in the region from $25 \leq r \leq 70$ km, with τ_{fil} reaching as low as 5 min. While the two panels are for two different heights, some evolution of the storm structure is evident. It looks as though the eyewall has contracted, as the RMW moves inward 2–5 km from Fig. 3.9b to Fig. 3.9a. Since this storm consistently showed outward tilt with height in the P3 tail radar during this IOP, it is probable that the overall eyewall contraction was greater than indicated in these panels. Also, assuming a warm-cored, baroclinic vortex with decreasing winds with height, the maximum winds in Rita appear to had strengthened in comparing the 700 hPa and 640 hPa composites.

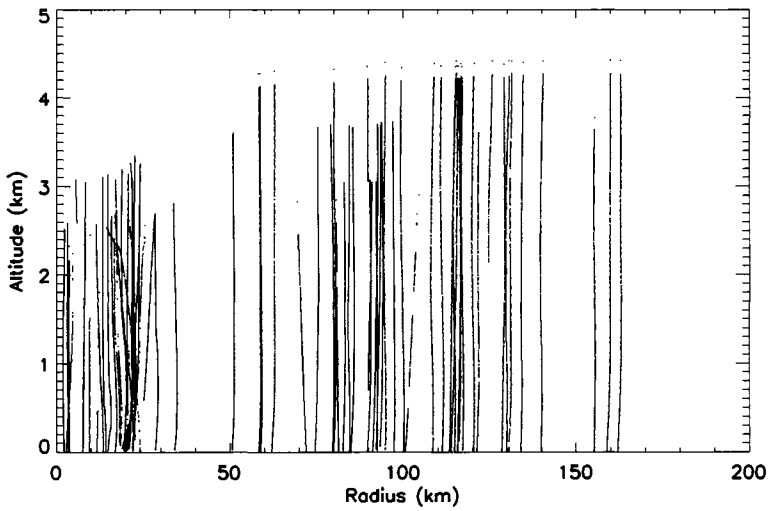

Figure 3.11: Dropsonde data points with respect to radius and height for Hurricane Rita on 21 September 2005.

Rita's temperature and dewpoint profiles are presented in Fig. 3.10. The two panels in Fig. 3.10 are for the same times and pressure levels presented in Fig. 3.9 and we once again use the same compositing parameters. Overall, Rita possessed a well-defined warm core at both 700 and 640 hPa. This warm core was located within

the RMW. Perhaps the most notable feature in Rita's eye is the extreme dewpoint depression of 30°C in the 640 hPa composite (Fig. 3.10). The flat and tremendous dewpoint depressions are consistent with uniform and enhanced eye subsidence within the eye. Such an eye subsidence distribution may be indicative of lower inertial stability within the eye (Schubert et al., 2007), so these profiles would be dynamically consistent with the v_θ profiles shown in Fig. 3.9. Outside the RMW, temperatures and dewpoints are roughly constant in space in Fig. 3.10a,b, with relatively moist conditions throughout a broad radial region. Dewpoint depressions of 1 to 3°C are shown in the 640 hPa leg outside the eyewall.

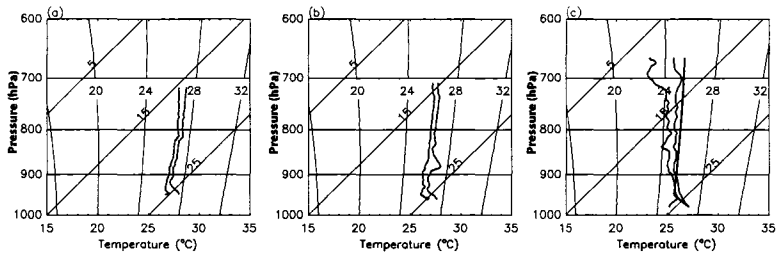

Figure 3.12: Individual Rita (2005) dropsondes at (a) $r = 29$ km and 1525 UTC, (b) $r = 34$ km and 1526 UTC, and (c) $r = 51$ km and 1907 UTC on 21 September. In (c), a hypothetical surface-based parcel path temperature profile is added to indicate the potential available low-level buoyancy.

Between the NOAA and NRL P3s, over 70 dropsondes were released into the lower troposphere of Rita on 21 September (Fig. 3.11). While a large number of dropsondes were released in the eye, eyewall, and outer rainbands, only a limited number of these sondes were released immediately outside Rita's RMW. Nonetheless, 5 sondes fell between $r = 25$ and 55 km. Figure 3.12 provides three individual dropsonde profiles outside Rita's RMW at $r = 28$, 34, and 51 km around 1525, 1526, and 1907 UTC, respectively. The temperature profiles in Figs. 3.12a,b roughly follow moist adiabats, suggesting that the region just outside of Rita's RMW was convectively neutral at lower levels at these times. This region was nearly saturated, consistent with an environment experiencing precipitation. Later on at 1907 UTC, at

$r = 51$ km (Fig. 3.12c), a slightly drier but more unstable situation was documented.

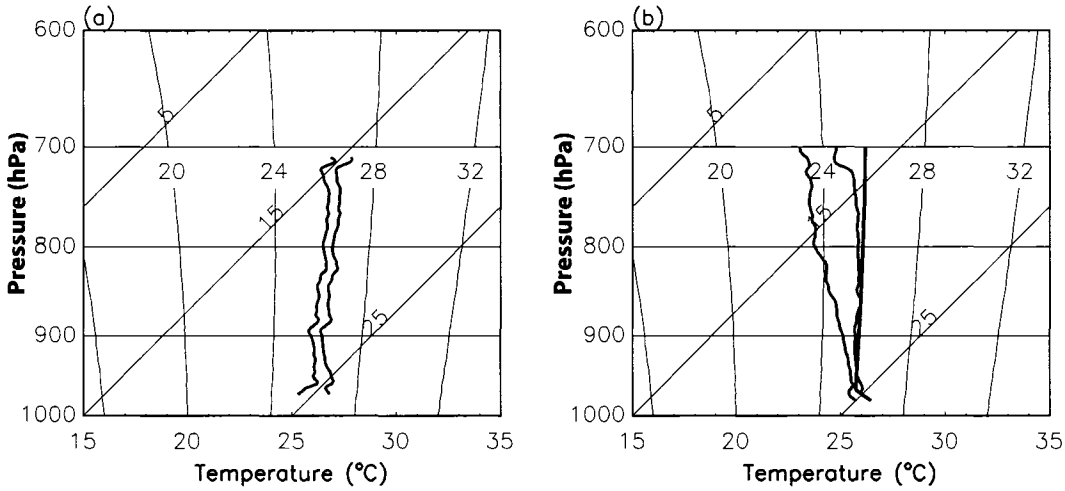

Figure 3.13: Dropsonde composites for (a) 25 km $\leq r \leq$ 55 km, and (b) 55 km $\leq r \leq$ 85 km.

Using (3.1) and (3.2), composite dropsondes are constructed for two radial zones: 25 km $\leq r \leq$ 55 km and 55 km $\leq r \leq$ 85 km (Fig. 3.13). In these composites, data are binned into 0.5 hPa intervals and an averaging window of 2 $\delta p = 10$ hPa is chosen. Five dropsondes are included in the composite given in Fig. 3.13a and 11 dropsondes are incorporated into the composite shown in Fig. 3.13b. The average standard deviation of the temperature and dewpoint for the inner composite sonde is 0.8°C and 0.9°C, respectively, while the average standard deviation for the same variables in the outer region is 1.1°C and 0.8°C. Consistent with the individual soundings, the composite for the inner region is moist and closely follows a moist adiabat, while the outer region presents marginal low-level buoyancy. As indicated in Fig. 3.13b, the dewpoint depressions were greater in the outer region. While the composite sounding analysis suggests convection is thermodynamically unlikely between the RMW and $r = 55$ km, occasional filamentary convection appeared in the radar sweeps (Fig. 3.8), suggesting there was either enough forcing and/or pockets of sufficiently favorable thermodynamic conditions to allow convective clouds to intermittently form in this region. The thin, filamentary nature of the convection is

consistent with τ_{fil} of 5 to 10 min in this region.

3.4.2 22 September 2005

Another extensive RAINEX IOP took place in Rita on 22 September. The storm developed a concentric eyewall configuration on this date immediately after achieving its maximum intensity of 80 m s^{-1} that morning. Following overnight and morning flight missions from the USAF C130, the N42, N43, and the NRL P3 gathered observations in Rita's inner-core during the concentric eyewall situation. The N43 conducted extensive "figure four" patterns at 700 hPa into Rita's eye and obtained extensive coverage of both eyewalls. The NRL P3's mission was dedicated to taking measurements of the secondary eyewall and the N42 made several eyewall passes at 1500 and 2150 m height levels. Each plane had dual Doppler radar coverage.

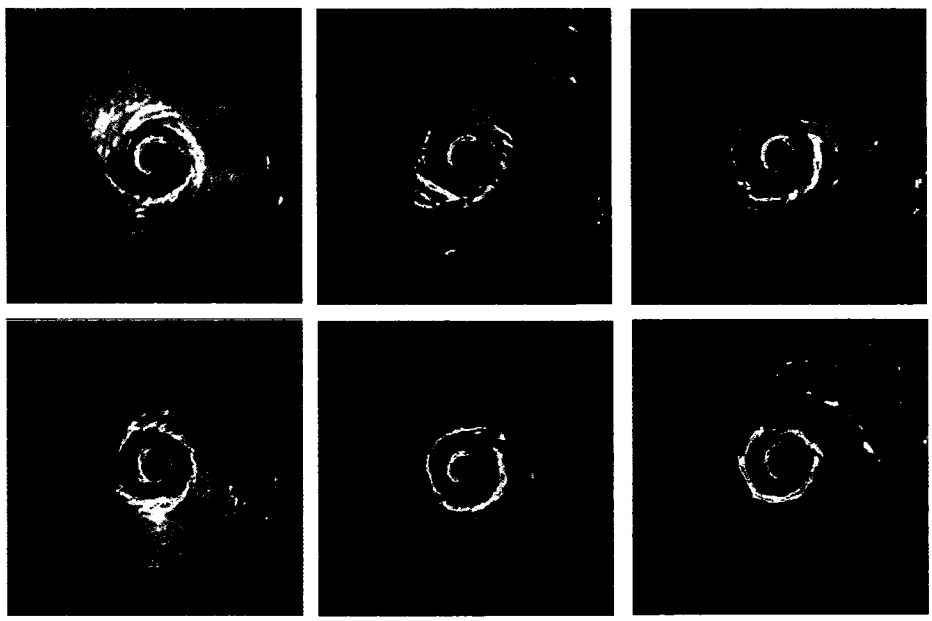

Figure 3.14: Individual N43 LF reflectivity (dBZ) sweeps during the RAINEX IOP on 22 September for (a) 1457 UTC, (b) 1612 UTC, (c) 1623 UTC, (d) 1752 UTC, (e) 1911 UTC, and (f) 2041 UTC. The grid box size is 360 × 360 km. Blue reflectivity colors represent 20–25 dBZ, green is 25–30 dBZ, yellow is 30–35 dBZ, orange is 35–40 dBZ, and red is 40–45 dBZ. This imagery is provided by HRD.

The evolution of N43 LF reflectivity on 22 September shows there was a maturing concentric eyewall configuration (Fig. 3.14). Throughout this period, the concentric eyewall continually gained intensity in reflectivity, with a nearly solid ring of 40 dBZ by 2041 UTC. The secondary eyewall generally maintained some ellipticity. Also, the central eyewall possessed a notable wavenumber-1 asymmetry. The moat was characterized by weak-echoes of stratiform precipitation. Nonetheless, certain radar images indicate that relatively transient, filamentary, convective rainbands formed within the moat. Also, the secondary eyewall occasionally produced vivid, small-scale convective banding (e.g., Figs. 3.14b,c,d) within the axisymmetric mean convective ring. Outside of the secondary eyewall, stratiform precipitation was widespread. The coverage of actively convective rainbands was decidedly sparse on 22 September in comparison to the outer rainbands observed on 21 September. The relatively weak rainbands that did form immediately outside of the secondary eyewall were highly filamentary.

Using the same averaging parameters as before, we obtain the composite flight-level v_θ profiles shown in Fig. 3.15. The top panel of Fig. 3.15 contains all of the N43 flight data at 700 hPa (10 radial passes) and the associated composite over the period 1437–2057 UTC. Figure 3.15b presents all N42 flight-level v_θ data and composite at 2100 m (2 radial passes), while Fig. 3.15c contains all of the N42 flight-level v_θ data and associated composite at 1500 m. Secondary eyewalls appear in all three composites to various degrees. In each instance, the composite wind profile suggests a rapid filamentation zone, nearly comparable in strength with the one observed on 21 September, was present in Rita's moat. Moreover, as seen in Gilbert and Frances, a rapid filamentation zone existed outside of the secondary wind maximum.

At first glance, it may be noted that these composite profiles appear inconsistent with one another. The composites in Figs. 3.15a,b show a smoothed secondary wind maximum in comparison with Fig. 3.15c and the composite secondary wind maximum

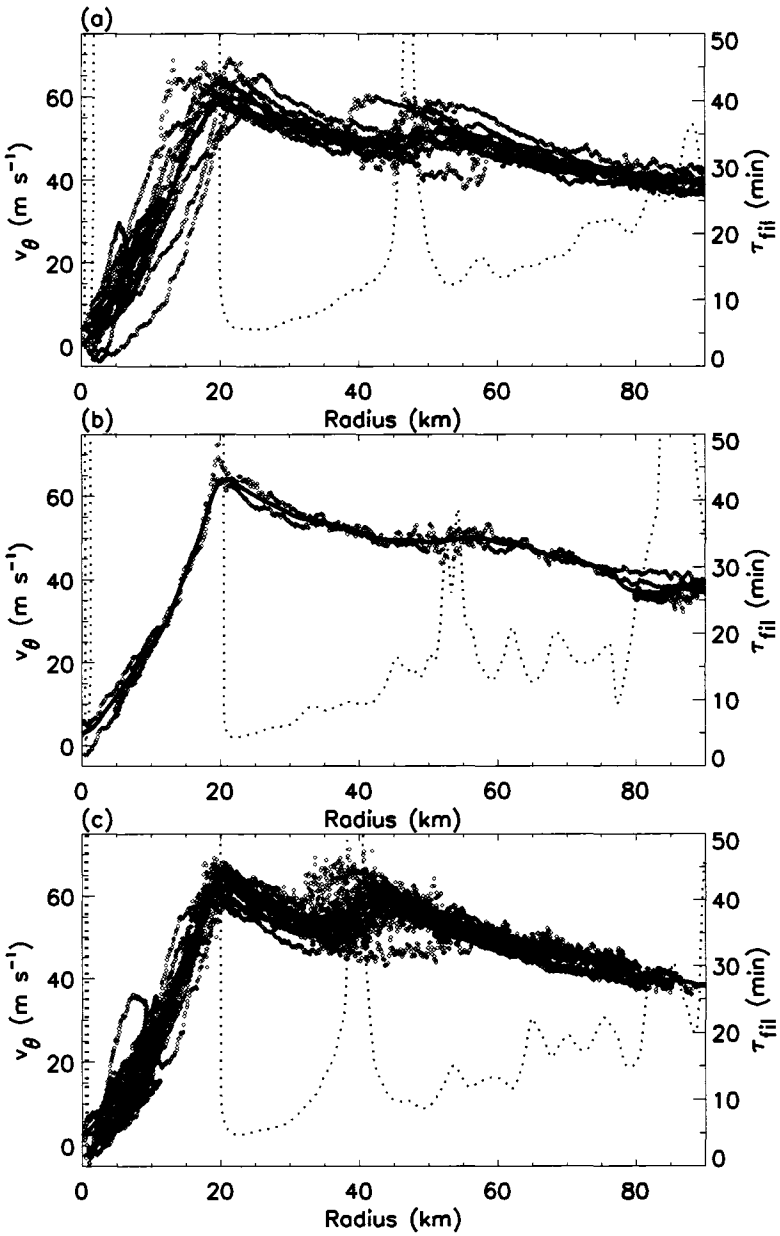

Figure 3.15: Hurricane Rita (2005) composite radial profiles of flight-level tangential wind, v_θ (m s^{-1}; solid black) and individual wind observations (blue dots) for (a) the N43 mission at 700 hPa, which covers 10 radial passes over 1437–2057 UTC, (b) the N42 mission at 2100 m, which covers 2 radial passes over 1705–1735 UTC, and (c) the N42 mission at 1500 m, which covers 16 radial passes over 1754–2213 UTC on 22 September. The filamentation time (red dotted curves), τ_{fil}, is computed for each composite profile.

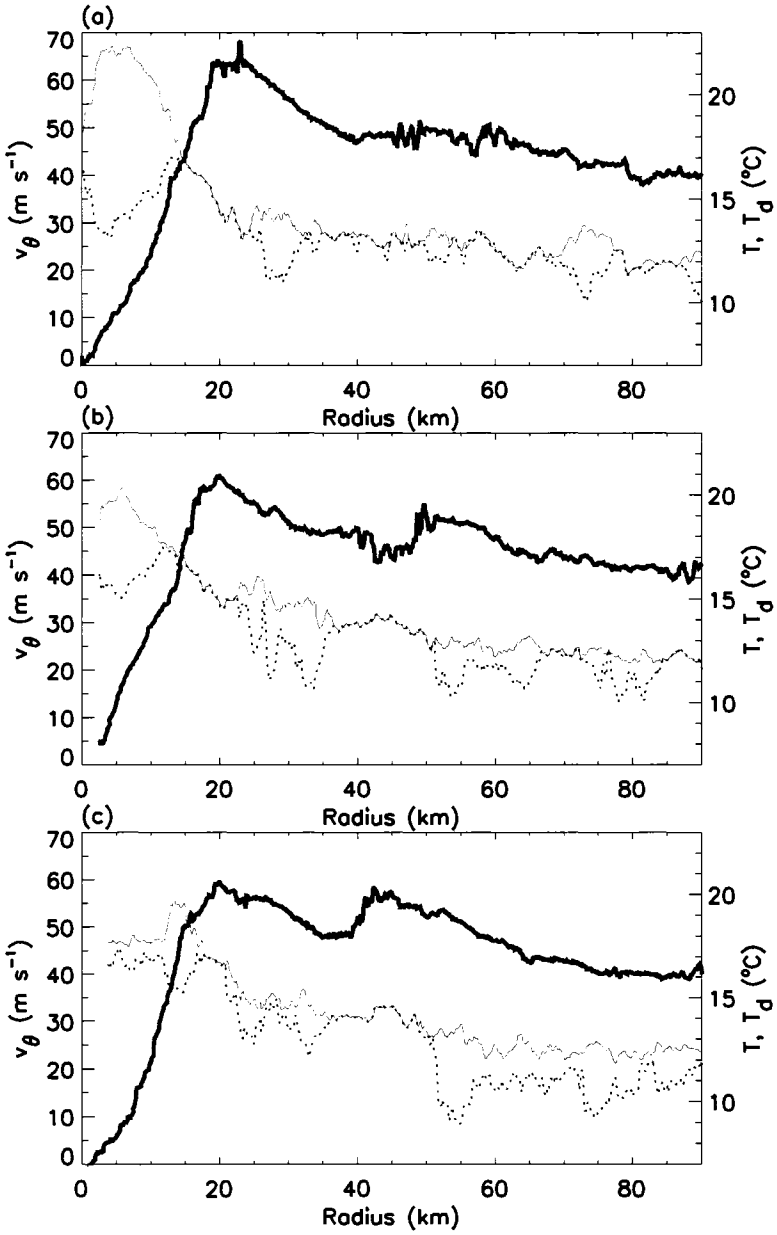

Figure 3.16: Individual N43 radial passes of v_θ (m s^{-1}; blue), temperature (°C; red), and dewpoint (°C; green dotted) in Hurricane Rita on 22 September 2005. The radial passes are over time periods (a) 1437–1449 UTC, (b) 1602–1616 UTC, and (c) 2030–2043 UTC.

in Fig. 3.15c is located considerably inward from the ones shown in Figs. 3.15a,b. These results indicate that the secondary eyewall was contracting inward throughout the IOP. While large azimuthal asymmetries are evident in the individual radial flight passes, individual passes demonstrate the growth and rapid contraction of the secondary eyewall during the 22 September IOP. Figure 3.16 displays individual N43 radial profiles of v_θ, temperature and dewpoint over the time periods of 1437–1449, 1602–1616, and 2030–2043 UTC. At the beginning of this IOP, a secondary ring started to emerge in the radar and a maximum in v_θ developed between $r = 40$ and 65 km (Fig. 3.16a). By 1616 UTC, a secondary maximum exceeding 50 m s^{-1} formed around 50–55 km from center. This secondary eyewall's contraction is quite noticeable by 2043 UTC in Fig. 3.16b, where the concentric eyewall's RMW was around 45 km. Throughout this period, contraction of the primary eyewall is not discernable. However, a weakening trend in the primary eyewall's maximum v_θ is recognizable. The temperature and dewpoint profiles in Fig. 3.16 evolve in tandem with the wind fields. Along with decreasing v_θ in the primary eyewall, the central warm core appears to have weakened during this period. However, consistent with a vortex near thermal wind balance, the radial extent of the warm core slightly broadened as the secondary eyewall strengthened and contracted. In the moat, substantial dewpoint depressions variations of 0–4°C were observed. Perhaps more obvious in the time evolution of data is the emergence of drier air outside of the secondary eyewall later in the IOP.

Individual N42 passes at 1500 m height further exemplify the rapid evolution of the concentric eyewall configuration (Fig. 3.17). Overall, these profiles are consistent with the radial location of the wind maxima presented in Fig. 3.16. By 2043 UTC, the secondary eyewall maximum had contracted inward to around 30–35 km (Fig. 3.17c). Temperatures were locally depressed within the eyewalls. It is unclear if this temperature pattern resulted from instrumental error (Eastin et al., 2002) or was physical cooling. Either way, precipitation may have played some role in this locally "cool"

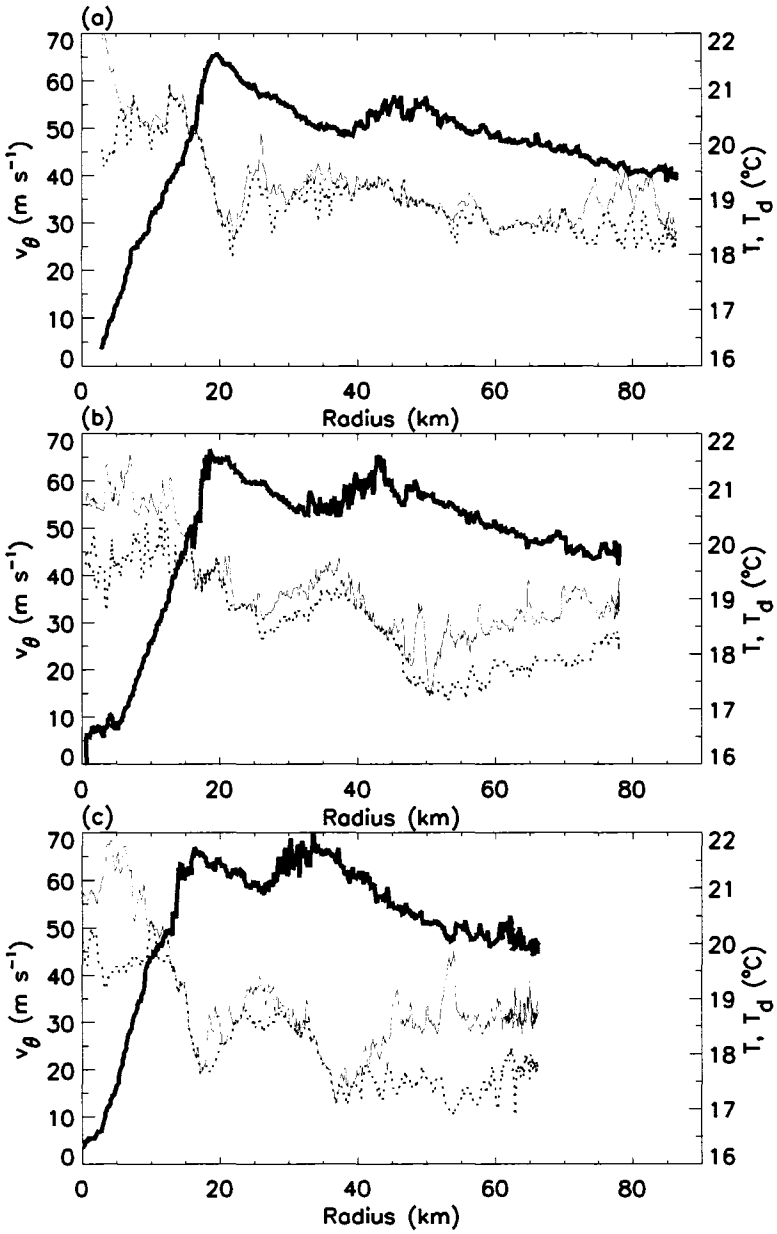

Figure 3.17: Individual N42 radial passes, at 1500 m, of v_θ (m s^{-1}; blue), temperature (°C; red), and dewpoint (°C; green dotted) in Hurricane Rita on 22 September 2005. The radial passes are over time periods (a) 1809–1820 UTC, (b) 1959–2013 UTC, and (c) 2126–2139 UTC.

area. Dewpoint depressions were also enhanced outside of the secondary eyewall in the N42 data at later times. These are signs environmental dry air may have been impinging into Rita's core late in the day on 22 September.

Using the same compositing parameters as before, Fig. 3.18 recasts all of the individual profiles into a composite analysis. Little new infomation results from this composite, but the azimuthally averaged structure provides some confidence that the balanced structure of the vortex changed in response to the development and contraction of the secondary eyewall. Namely, the warm core weakened and expanded during the ERC. Also, in comparison with 21 September (Fig. 3.10), dewpoint depressions in the eye were not as remarkable as they were on 22 September. In particular, the average eye dewpoint depression at 700 hPa was around 4°C on 22 September, whereas the 700 hPa values were over 15°C just a day earlier. On 22 September, the dewpoint depressions within the moat, which range between 1°C at 1500 m and 1–2°C at 700 hPa, were comparable to those observed in the same radial region on 21 September.

In contrast with 21 September, many dropsondes were released from all three P3s into the moat and elsewhere in Rita on 22 September (Fig. 3.19). However, the majority of moat dropsondes were released after 1600 UTC. In order to evaluate time evolution of the low-level thermodynamic conditions in Rita, we create composite soundings for two annular regions for two different time periods. Our annular regions are constructed for radial intervals of 25–40 km (moat) and 50–65 km (exterior to the secondary eyewall) for the time periods 1600–1900 UTC and 1900–2200 UTC. The same composite parameters used on 21 September are utilized in the current analysis. In the 1600–1900 UTC composite, 5 and 10 dropsondes from the inner and outer regions are available for analysis, while only 5 dropsondes are available for both radial regions in the period 1900–2200 UTC.

The composite dropsondes for both time periods are fairly similar. According to the composite soundings, the moat region contained marginal convective instability,

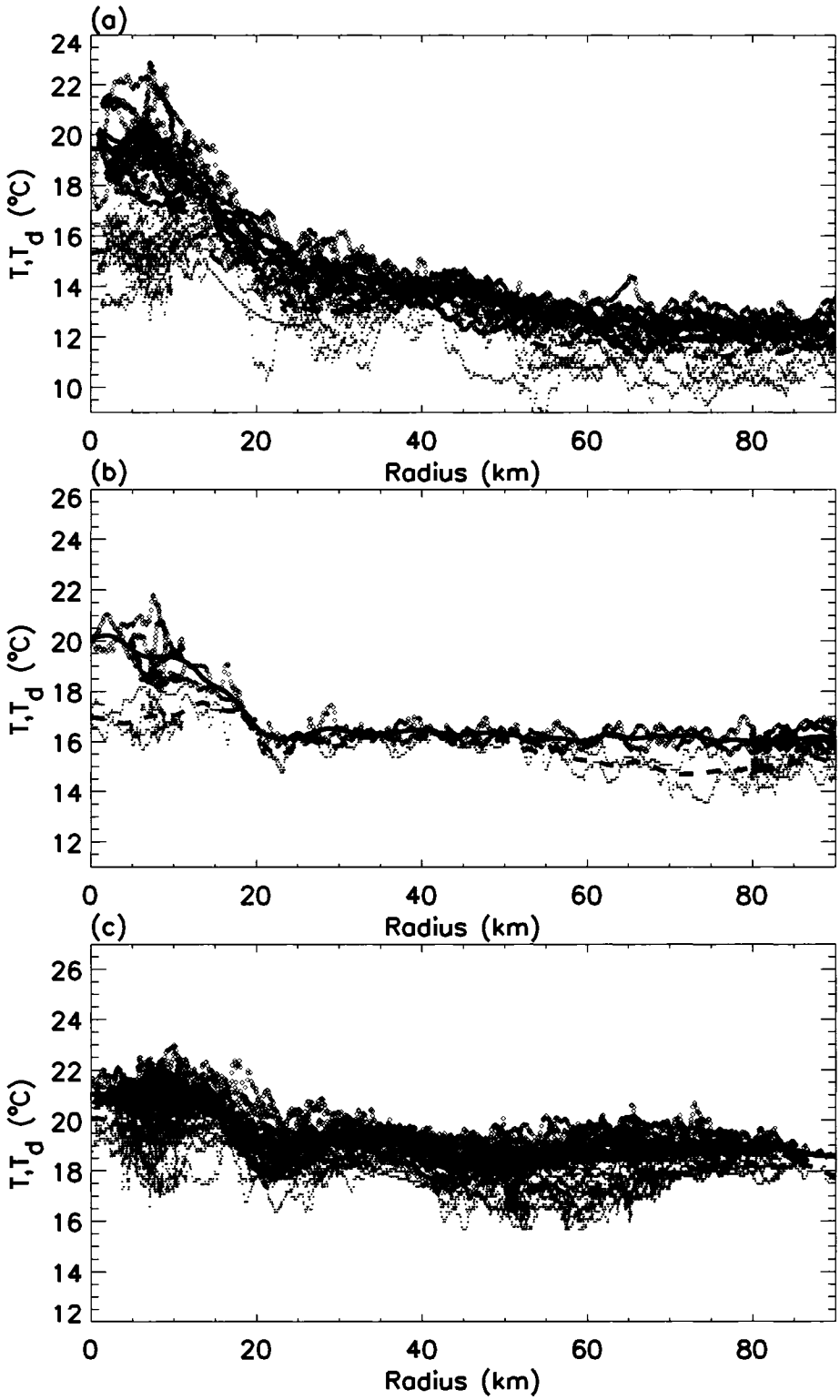

Figure 3.18: Hurricane Rita composite radial profiles of 700 hPa flight-level temperature, T (°C; solid black), and dewpoint, T_d (°C; dashed black) and individual temperature and dewpoint observations (red and green dots, respectively), for the (a) 700 hPa N43 passes (1437–2057 UTC), (b) the N42 passes at 2.1 km (1705–1735 UTC), and (c) the N42 passes at 1.5 km (1754–2213 UTC) on 22 September 2005.

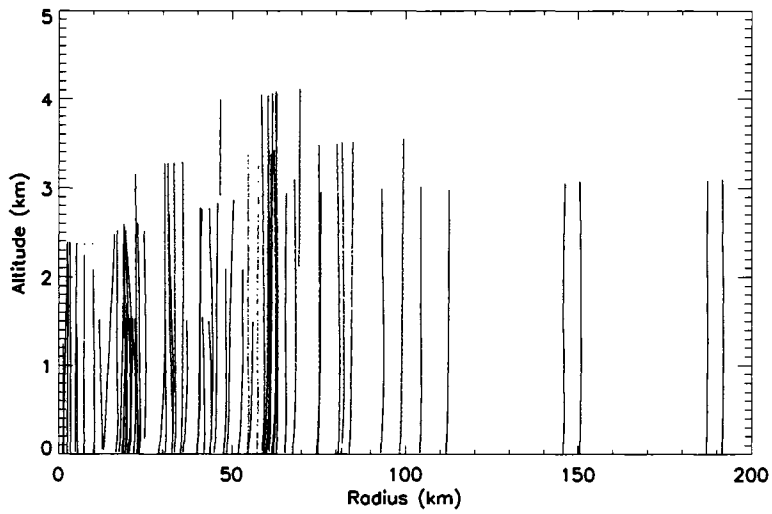

Figure 3.19: Dropsonde data points with respect to radius and height for Hurricane Rita on 22 September 2005.

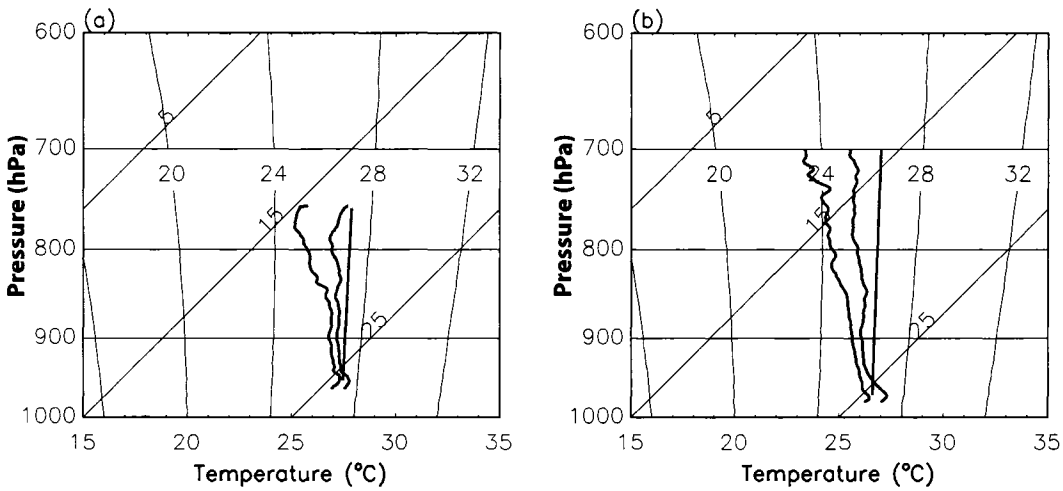

Figure 3.20: Composite dropsondes for Rita in the regions (a) $25 \leq r \leq 40$ km and (b) $50 \leq r \leq 65$ km during the period 1600–1900 UTC on 22 September 2005.

although the 1600–1900 UTC composite suggests there was at least some low-level instability available. It should be noted that several spiral convective bands briefly appeared in the moat during this period. The region outside of the secondary eyewall contained more low-level potential convective instability with its steeper lapse rates.

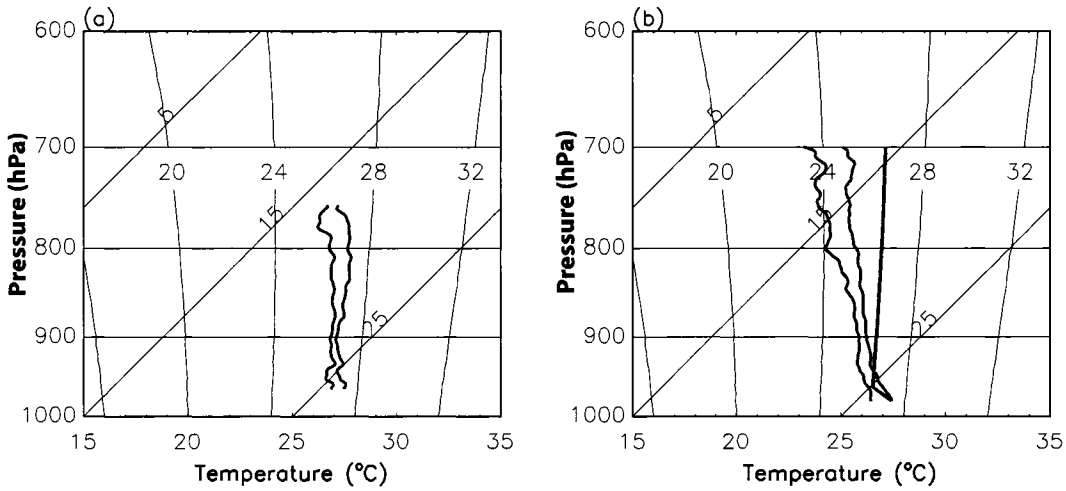

Figure 3.21: Composite dropsondes for Rita in the regions (a) $25 \leq r \leq 40$ km and (b) $50 \leq r \leq 65$ km during the period 1900–2200 UTC on 22 September 2005.

3.5 Summary and discussion

Each of the above case studies explored the composite structure of winds and potential convective instability with the aid of dropsondes and high-resolution flight-level data. Rapid filamentation zones were found outside both the inner and outer eyewalls of the analyzed hurricanes. Hurricane Frances (2004) showed a very well-developed moat, with eye-like soundings in the moat. A warm-core was building within the moat during that period. Rita showed marginal convective conditions outside of its RMW throughout 21 and 22 September, but radar data confirmed transient convective bands appeared intermittently next to the primary eyewall, strongly suggesting that localized regions of favorable conditions for convection periodically appeared within the forming moat. These bands were highly filamentary.

Soon after the above observational analysis was completed, Houze et al. (2007)

appeared with a very similar analysis of Rita on 22 September. Using the NRL Eldora and N43 radars, their analysis includes an azimuthally-averaged cross section of winds in the moat. In contrast to Dodge et al. (1999), they showed downward motion is prevalent throughout much of the depth of Rita's moat on 22 September. Furthermore, they remarked upon the fact that some individual moat soundings showed eye-like qualities. Their results are very consistent with the above analysis.

Supposing the recent Doppler analyses of downward motion in Rita on 22 September is commonplace in all well-formed moats, then it is likely rapid filamentation theory plays little, if any role, in maintaining the moat's weak-echo character. However, given marginal convective instability, it was hypothesized earlier that convection, and thus filamentation, may be essential in the incipient stages of the moat. Moreover, rapid filamentation may help prevent secondary eyewalls from forming too close to the primary eyewall (e.g., Kossin et al., 2000).

From a balanced-vortex perspective, we now show that convection in a moat is increasingly less likely thermodynamically as a secondary eyewall develops and matures. Along a similar path taken in Schubert and Hack (1982) and Schubert et al. (2007), we seek idealized, analytical solutions of the Sawyer-Eliassen transverse circulation with an idealized radial distribution of inertial stability and diabatic heating. In the following analysis, we consider positive diabatic heating associated with two eyewalls but neglect the impacts of momentum sources. Physical processes that help generate secondary eyewall formation may qualify as momentum sources, but it is not immediately clear how their induced transverse circulations explain typical moat subsidence distributions. Nonetheless, assuming decreasing background density with height, the upper-level subsidence and warming resulting from a positive momentum source near a forming secondary eyewall would be expected to increase the stability of the moat in tandem with the stabilizing circulation induced by diabatic heating (see Figs. 12 and 13 in Shapiro and Willoughby, 1982). How typical momentum sources

exactly modulate subsidence in the moat should be the subject of future research.

In order to obtain analytical solutions to an idealized Sawyer-Eliassen equation, we consider inviscid, axisymmetric, quasi-static, quasi-gradient motions of a stratified, compressible atmosphere on an f-plane. As the vertical coordinate we use $z_p = H\ln(p_0/p)$, where $H = RT_0/g$ is the constant scale height and where $p_0 = 100$ kPa and $T_0 = 300$ K are constant reference values of pressure and temperature. The governing equations for this balanced vortex model are

$$\begin{gathered}\left(f+\frac{v_\theta}{r}\right)v_\theta = \frac{\partial\phi}{\partial r}, \qquad \frac{Dv_\theta}{Dt}+\left(f+\frac{v_\theta}{r}\right)v_r = 0, \qquad \frac{\partial\phi}{\partial z_p} = \frac{g}{T_0}T, \\ \frac{\partial(rv_r)}{r\partial r}+\frac{\partial w_p}{\partial z_p}-\frac{w_p}{H} = 0, \qquad c_p\frac{DT}{Dt}+\frac{RT}{H}w_p = Q,\end{gathered} \tag{3.4}$$

where $w_p = Dz_p/Dt$ is the "log-pressure vertical velocity," ϕ is the geopotential, T is the temperature, f is the constant Coriolis parameter, Q is the diabatic heating, and $D/Dt = \partial/\partial t + v_r(\partial/\partial r) + w_p(\partial/\partial z_p)$ is the material derivative.

To derive a Sawyer-Eliassen equation to diagnose a secondary circulation of a vortex, we first note that, because of the continuity equation, the transverse circulation (v_r, w_p) can be expressed in terms of the streamfunction ψ such that $e^{-z_p/H}v_r = -\partial\psi/\partial z_p$ and $e^{-z_p/H}w_p = \partial(r\psi)/r\partial r$. We next note that the thermal wind equation, derived from the hydrostatic and gradient wind equations, is $[f+(2v_\theta/r)](\partial v_\theta/\partial z_p) = (g/T_0)(\partial T/\partial r)$. Differentiating this thermal wind equation with respect to time, we obtain $(\partial/\partial z_p)\{[f+(2v_\theta/r)](\partial v_\theta/\partial t)\} = (g/T_0)(\partial/\partial r)(\partial T/\partial t)$, which shows the tendencies $\partial v_\theta/\partial t$ and $\partial T/\partial t$ are related by the constraint of continuous thermal wind balance. The diagnostic equation for ψ is obtained by eliminating the local time derivatives in the tangential wind equation and the thermodynamic equation through the use of this constraint. The resulting transverse circulation equation is

$$\frac{\partial}{\partial r}\left(A\frac{\partial(r\psi)}{r\partial r}+B\frac{\partial\psi}{\partial z}\right)+\frac{\partial}{\partial z}\left(B\frac{\partial(r\psi)}{r\partial r}+C\frac{\partial\psi}{\partial z}\right) = \frac{g}{c_pT_0}\frac{\partial Q}{\partial r}, \tag{3.5}$$

where the static stability A, the baroclinity B, and the inertial stability C are defined

by

$$A = e^{z_p/H}\frac{g}{T_0}\left(\frac{\partial T}{\partial z_p} + \frac{\kappa T}{H}\right), \tag{3.6}$$

$$B = -e^{z_p/H}\frac{g}{T_0}\frac{\partial T}{\partial r} = -e^{z_p/H}\left(f + \frac{2v_\theta}{r}\right)\frac{\partial v_\theta}{\partial z_p}, \tag{3.7}$$

$$C = e^{z_p/H}\left(f + \frac{2v_\theta}{r}\right)\left(f + \frac{\partial(rv_\theta)}{r\partial r}\right). \tag{3.8}$$

Only vortices with $AC - B^2 > 0$ everywhere are considered, which ensures (3.5) is an elliptic equation. As for boundary conditions on (3.5), it is required ψ vanish at $r = 0$ and at the bottom and top isobaric surfaces $z_p = 0, z_T$, and $r\psi \to 0$ as $r \to \infty$.

In the following discussion, we focus on the question of how the spatial variability of the inertial stability C affects the transverse circulation when diabatic forcing takes place in a double eyewall structure. To isolate this effect we consider a barotropic vortex ($B = 0$) in which the static stability is given by $A = e^{z_p/H}N^2$, where the square of the Brunt-Väisälä frequency, N^2, is a constant. The inertial stability (3.8) can then be written in the form $C = e^{z_p/H}\hat{f}^2$, where $\hat{f}(r) = \{[f + (2v_\theta/r)][f + \partial(rv_\theta)/r\partial r]\}^{1/2}$ is the "effective Coriolis parameter." Neglecting baroclinity still adequately represents the radial impacts of inertial stability variations upon the secondary circulation (Schubert et al., 2007). Now, considering the first vertical, internal mode (e.g., Schubert and Masarik, 2006), the diabatic heating $Q(r, z_p)$, the vertical velocity $w_p(r, z_p)$, and the streamfunction $\psi(r, z_p)$ have the separable forms $Q(r, z_p) = \hat{Q}(r)\exp[z_p/(2H)]\sin(\pi z_p/z_T)$, $w_p(r, z_p) = \hat{w}_p(r)\exp[z_p/(2H)]\sin(\pi z_p/z_T)$, and $\psi(r, z_p) = \hat{\psi}(r)\exp[-z_p/(2H)]\sin(\pi z_p/z_T)$, equation (3.5) reduces to

$$r^2\frac{d^2\hat{\psi}}{dr^2} + r\frac{d\hat{\psi}}{dr} - \left(\mu^2 r^2 + 1\right)\hat{\psi} = \frac{gr^2}{c_p T_0 N^2}\frac{d\hat{Q}}{dr}, \tag{3.9}$$

where $\mu(r) = [\hat{f}(r)/N][(\pi/z_T)^2 + (2H)^{-2}]^{1/2}$ is the inverse Rossby length, and $\hat{w}_p = d(r\hat{\psi})/rdr$. Thus, the original task of solving (3.5) has been reduced to the task of solving (3.9).

To treat radial variations of $\mu(r)$ in a simple manner, we consider the specific barotropic vortex where the square of the absolute angular momentum is given by

$m^2(r) = [rv_\theta(r) + \frac{1}{2}fr^2]^2 = [r_j v_\theta(r_j) + \frac{1}{2}fr_j^2]^2 + \frac{1}{4}\hat{f}_j^2(r^4 - r_j^4)$ for $r_j \le r \le r_{j+1}$. Here we consider a five-region model ($j = 0, 1, 2, 3, 4$) with $r_0 = 0$ representing the origin, r_1 and r_2 representing the bounding radii of the inner eyewall, r_3 and r_4 representing the bounding radii of the outer eyewall, and $r_5 = \infty$. The five specified constants $\hat{f}_j$ ($j = 0, 1, 2, 3, 4$) give the effective Coriolis parameters in the five regions. Since, for each interval $r_j < r < r_{j+1}$,

$$\hat{f}(r) = \left(\frac{\partial m^2}{r^3\,\partial r}\right)^{1/2} = \left[\left(f + \frac{2v_\theta}{r}\right)\left(f + \frac{\partial(rv_\theta)}{r\partial r}\right)\right]^{1/2} = \hat{f}_j, \tag{3.10}$$

the inverse Rossby length has the piecewise constant form

$$\mu(r) = \frac{\hat{f}(r)}{N}\left(\frac{\pi^2}{z_T^2} + \frac{1}{4H^2}\right)^{1/2} = \begin{cases} \mu_0 & \text{if } 0 \le r < r_1 \text{ (eye)}, \\ \mu_1 & \text{if } r_1 < r < r_2 \text{ (inner eyewall)}, \\ \mu_2 & \text{if } r_2 < r < r_3 \text{ (moat)}, \\ \mu_3 & \text{if } r_3 < r < r_4 \text{ (outer eyewall)}, \\ \mu_4 & \text{if } r_4 < r < \infty \text{ (far-field)}. \end{cases} \tag{3.11}$$

Similarly, we assume that the diabatic heating occurs only in concentric eyewalls, with the particular piecewise constant form

$$\hat{Q}(r) = \begin{cases} 0 & 0 \le r < r_1 \text{ (eye)}, \\ Q_1 & r_1 < r < r_2 \text{ (inner eyewall)}, \\ 0 & r_2 < r < r_3 \text{ (moat)}, \\ Q_3 & r_3 < r < r_4 \text{ (outer eyewall)}, \\ 0 & r_4 < r < \infty \text{ (far-field)}, \end{cases} \tag{3.12}$$

where Q_1 and Q_3 are constants. Only five of the six constants $r_1, r_2, r_3, r_4, Q_1, Q_3$ are independently specified. The six constants are constrained by the assumption that

$$(Q_1/c_p)\left(r_2^2 - r_1^2\right) + (Q_3/c_p)\left(r_4^2 - r_3^2\right) = 125\,\text{K day}^{-1}(50\text{ km})^2. \tag{3.13}$$

A rough interpretation of this constraint is the implied, area-averaged rainfall is fixed as we vary any five of the six parameters $r_1, r_2, r_3, r_4, Q_1, Q_3$. The particular values chosen in the last equality in (3.13) give reasonable values of vertical motion and area-averaged rainfall, although the exact value on the right hand side of (3.13) is not important to our radial structure arguments since (3.5) and (3.9) are linear equations for the streamfunction.

The jump conditions, derived by integrating (3.9) across narrow intervals straddling the points $r = r_1, r_2, r_3, r_4$, are

$$\left[\frac{d(r\hat{\psi})}{r\,dr}\right]_{r_j^-}^{r_j^+} = \frac{g}{c_p T_0 N^2}\left[\hat{Q}(r_j^+) - \hat{Q}(r_j^-)\right] \qquad \text{for} \quad j = 1,2,3,4. \tag{3.14}$$

Under the assumptions (3.11) and (3.12), the solution of the ordinary differential equation (3.9) consists of linear combinations of the modified Bessel functions $I_1(\mu r)$ and $K_1(\mu r)$ in each of the five regions. Because $\hat{\psi} = 0$ at $r = 0$, we discard the $K_1(\mu r)$ solution in the inner region. Similarly, because $r\hat{\psi} \to 0$ as $r \to \infty$, we discard the $I_1(\mu r)$ solution in the outer region. The solution of (3.9) can then be written as

$$\hat{\psi}(r) = \begin{cases} \hat{\psi}_1 I_1(\mu_0 r)/I_1(\mu_0 r_1) & 0 \le r \le r_1, \\ [\hat{\psi}_1 F_1(r, r_2) + \hat{\psi}_2 F_1(r_1, r)]/F_1(r_1, r_2) & r_1 \le r \le r_2, \\ [\hat{\psi}_2 F_2(r, r_3) + \hat{\psi}_3 F_2(r_2, r)]/F_2(r_2, r_3) & r_2 \le r \le r_3, \\ [\hat{\psi}_3 F_3(r, r_4) + \hat{\psi}_4 F_3(r_3, r)]/F_3(r_3, r_4) & r_3 \le r \le r_4, \\ \hat{\psi}_4 K_1(\mu_4 r)/K_1(\mu_4 r_4) & r_4 \le r < \infty, \end{cases} \tag{3.15}$$

where $F_j(x, y) = I_1(\mu_j x)K_1(\mu_j y) - K_1(\mu_j x)I_1(\mu_j y)$ for $j = 1, 2, 3$, and $\hat{\psi}_1$, $\hat{\psi}_2$, $\hat{\psi}_3$, $\hat{\psi}_4$ are constants to be determined by the four jump conditions (3.14). We write (3.15) in such a way that $\hat{\psi}(r)$ is continuous at $r = r_1, r_2, r_3, r_4$. Using the derivative relations $d[rI_1(\mu r)]/rdr = \mu I_0(\mu r)$and $d[rK_1(\mu r)]/rdr = -\mu K_0(\mu r)$, differentiation of (3.15)

yields

$$\hat{w}_p(r) = \frac{d(r\hat{\psi})}{r\,dr} = \begin{cases} \mu_0\hat{\psi}_1 I_0(\mu_0 r)/I_1(\mu_0 r_1) & 0 \le r < r_1, \\ \mu_1[\hat{\psi}_1 G_1(r,r_2) - \hat{\psi}_2 G_1(r,r_1)]/F_1(r_1,r_2) & r_1 < r < r_2, \\ \mu_2[\hat{\psi}_2 G_2(r,r_3) - \hat{\psi}_3 G_2(r,r_2)]/F_2(r_2,r_3) & r_2 < r < r_3, \\ \mu_3[\hat{\psi}_3 G_3(r,r_4) - \hat{\psi}_4 G_3(r,r_3)]/F_3(r_3,r_4) & r_3 < r < r_4, \\ -\mu_4\hat{\psi}_4 K_0(\mu_4 r)/K_1(\mu_4 r_4) & r_4 < r < \infty, \end{cases} \tag{3.16}$$

where $G_j(x,y) = I_0(\mu_j x)K_1(\mu_j y) + K_0(\mu_j x)I_1(\mu_j y)$ for $j = 1, 2, 3$.Use of (3.16) in the jump conditions (3.14) leads to four algebraic equations that determine $\hat{\psi}_1, \hat{\psi}_2, \hat{\psi}_3, \hat{\psi}_4$, which can be solved analytically, or more practically, through a simple tri-diagonal solver.

From our five-region analytical model, we can learn more about the balanced vortex secondary circulation, (v_r, w_p), in different concentric eyewall situations. As a prototypical example, we revisit Hurricane Frances on 30 August 2004. Figure 3.22a shows the flight-level data from the period of 2117–2126 UTC (see Fig. 3.3f). Assuming $f = 5 \times 10^{-5}$ s^{-1}, $(N/f)[\pi^2 z_T^{-2} + (2H)^{-2}]^{-1/2} = 1000$ km, $N = 1 \times 10^{-2}$ s^{-1}, and applying the parameterized heating in (3.13), we specify our piecewise constant values of the "effective Coriolis force" in (3.10) by setting $(r_1, r_2, r_3, r_4) = (8, 15, 34, 40)$ km and $(v_\theta(r_1), v_\theta(r_2), v_\theta(r_3), v_\theta(r_4)) = (36, 46, 36, 55)$ m s^{-1}. The resulting v_θ profile is also plotted in Fig. 3.22a. Then, noting that the radial part of the temperature tendency equation, for a barotropic vortex, is

$$\frac{\partial \hat{T}}{\partial t} = \frac{\hat{Q}}{c_p} - \frac{T_0 N^2}{g}\hat{w}, \tag{3.17}$$

we obtain the temperature tendencies presented in Fig. 3.22b. While a barotropic vortex is cold-core along constant physical height surfaces, the temperature tendencies suggest, that over time, the vortex tends toward a warm-core structure, with radial structure similar to Fig. 3.22b. The radial structure of the temperature tendencies,

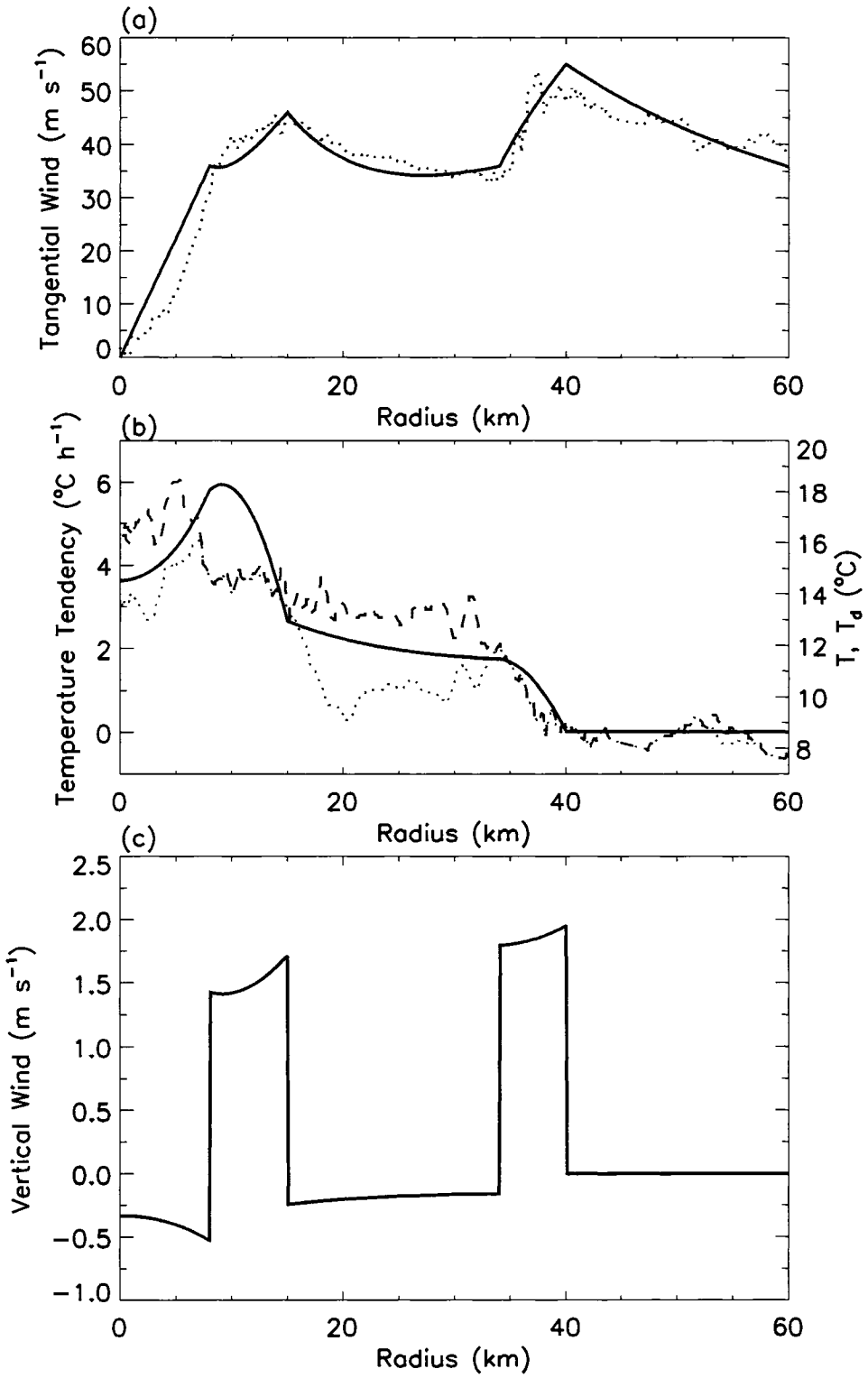

Figure 3.22: The five-region model approximation of the 700 hPa Frances radial pass between 2117–2126 UTC. (a) Observed (dotted gray) and analytical (solid black) v_θ (m s^{-1}), (b) observed temperature (dashed gray; °C), dewpoint (dotted gray; °C), and analytical temperature tendency (solid black; °C h^{-1}), and (c) resulting analytical vertical wind (m s^{-1}).

in fact, resembles the radial distribution of the flight-level temperature and dewpoint depression profiles. Hence, within the moat and the eye, a mature concentric eyewall situation leads to warming at radii within the secondary eyewall. This warming and its possible role in creating increased static stability in the moat have been qualitatively noted in earlier literature (e.g., Willoughby, 1990). Of course, the warming in the moat and eye is the result of subsidence associated with the balanced, transverse circulation. The analytical model diagnoses the vertical motion field shown in Fig. 3.22c. Due to large inertial stability throughout the eye, downward motion is somewhat restricted to the inner edge of the primary eyewall (Schubert et al., 2007). Throughout the moat, there is gentler subsidence of 0.2–0.25 m s^{-1}. These values of subsidence are sufficient to produce temperature tendencies of about 2°C h^{-1} within the moat.

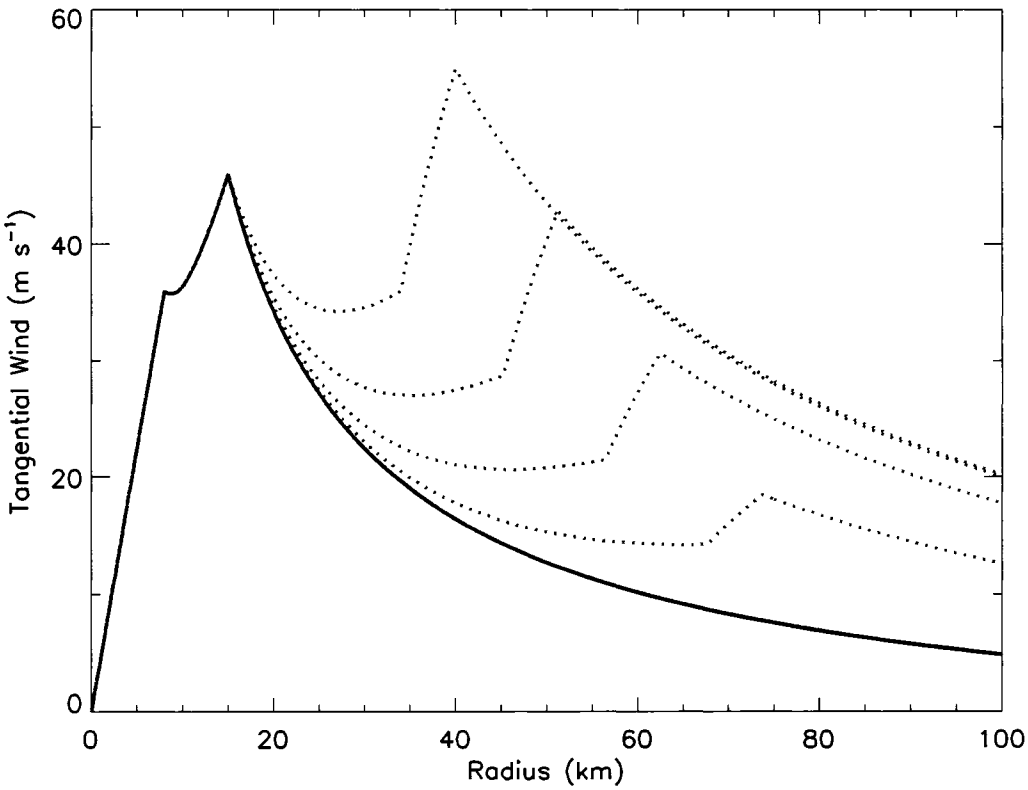

Figure 3.23: Five select v_θ profiles illustrating the range of double eyewall configurations to diagnose the downward mass flux partition during an eyewall replacement cycle.

Now, it is of interest to calculate the percentage of the total downward mass flux occurring in the eye, the moat, and the far-field during an ERC. From the streamfunction solution (3.15) it can be shown that, on any isobaric surface,

$$\sigma_{\text{eye}} = \frac{\text{Downward Mass Flux in Eye}}{\text{Total Downward Mass Flux}} = \frac{r_1\hat{\psi}_1}{r_1\hat{\psi}_1 + r_3\hat{\psi}_3 - r_2\hat{\psi}_2 - r_4\hat{\psi}_4}, \tag{3.18}$$

$$\sigma_{\text{moat}} = \frac{\text{Downward Mass Flux in Moat}}{\text{Total Downward Mass Flux}} = \frac{r_3\hat{\psi}_3 - r_2\hat{\psi}_2}{r_1\hat{\psi}_1 + r_3\hat{\psi}_3 - r_2\hat{\psi}_2 - r_4\hat{\psi}_4}, \tag{3.19}$$

$$\sigma_{\text{far-field}} = \frac{\text{Downward Mass Flux in Far} - \text{Field}}{\text{Total Downward Mass Flux}} = 1 - \sigma_{\text{eye}} - \sigma_{\text{moat}}. \tag{3.20}$$

This downward mass flux partition does not depend on the magnitude of heating in (3.18), but on the radial structure of heating. Now, we apply these concepts to an idealized ERC in Hurricane Frances. Figure 3.23 shows some select v_θ profiles to illustrate the range of wind profiles we choose to compute (3.18)–(3.20). The parameter r_4 ranges between $r = 85$ km (no secondary wind maximum) to $r = 40$ km (mature and contracted secondary wind maximum), r_3 is determined by keeping the distance $r_4 - r_3$ constant, and the heating constraint in (3.18) is always maintained. The most mature double eyewall structure used in our analysis is the Frances profile summarized above in Fig. 3.22. For simplicity, we assume that r_1 and r_2 are fixed. For the case of no secondary wind maximum, heating is still applied to the region between r_3 and r_4. This heating could be thought of as being the result of concentrated rainband activity in the region of an incipient concentric eyewall. Using these assumptions, we diagnose the subsidence distribution throughout much of a hypothetical ERC in our analytical model.

Figure 3.24 contains profiles of σ_{moat} and σ_{eye} as r_4 varies from $r = 85$ to $r = 40$ in our mock Frances ERC. The downward mass flux in the moat increases monotonically as the secondary eyewall matures and contracts. In other words, more of the outflow from the inner eyewall is forced to subside in the moat as the inertial stability associated with a contracting outer eyewall builds. In addition, a portion of the moat subsidence comes from the secondary eyewall as well, although most of

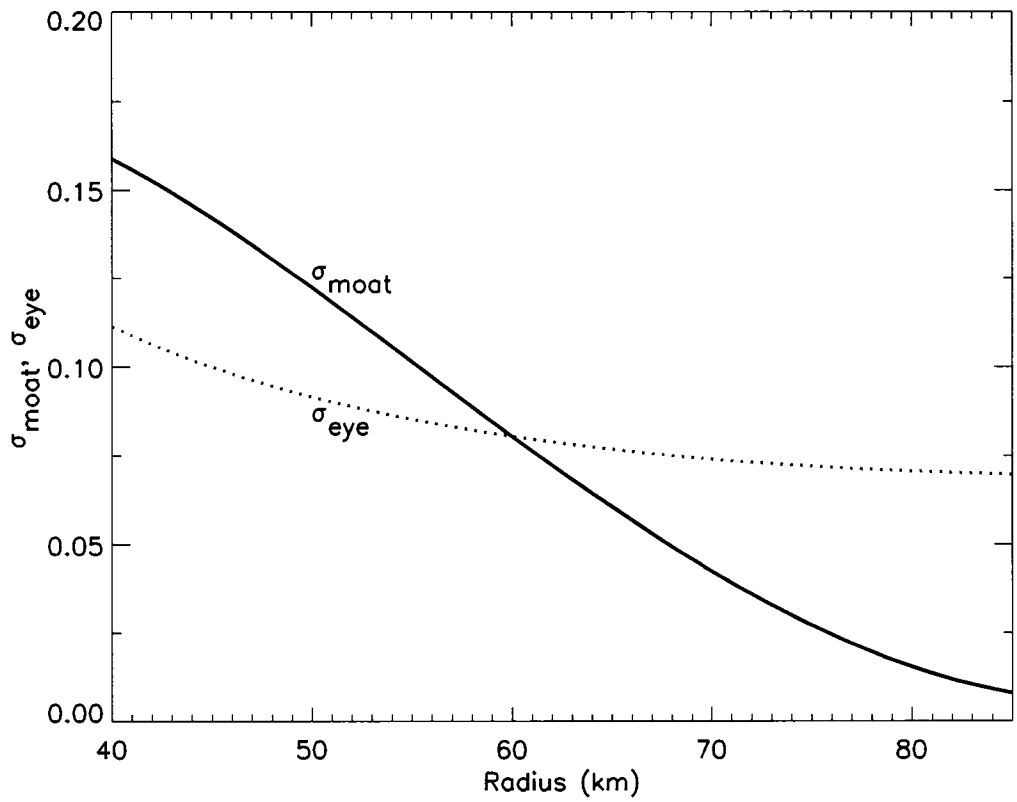

Figure 3.24: Values of the fraction of downward mass flux in the moat, σ_{moat} (solid black), and the fraction of downward mass flux in the eye, σ_{eye} (dotted gray) for the range of wind profiles shown in Fig. 3.23. The abscissa denotes the variable 5-region model parameter r_4.

the moat's mass flux originates from the outflow associated with the primary eyewall (figure not shown). As the secondary eyewall contracts to $r = 60$ km, the fraction of downward mass flux in the moat is equivalent to the eye. Eventually σ_{eye} noticeably increases as the secondary eyewall contracts inward of $r = 60$ km. As depicted in Fig. 3.25, the downward mass flux in the far-field decreases substantially as our hypothetical ERC progresses.

That our 5-region model rapidly produces an enhanced downward mass flux in the moat as our idealized ERC takes place suggests that the eye-like dropsondes in Frances' moat and in Rita's moat, as summarized above and in Houze et al. (2007), are expected once a secondary wind maximum becomes established. Thus, the eye-like character of a mature moat can be explained through the dynamics associated with an axisymmetric, quasi-balanced TC. This analysis further suggests rapid filamentation is probably less (more) of a player after (before) a secondary eyewall really starts to form and contract, although convection that can form in well-formed moat is all the more challenged because of strong filamentation, as we will now demonstrate in Chapter 4.

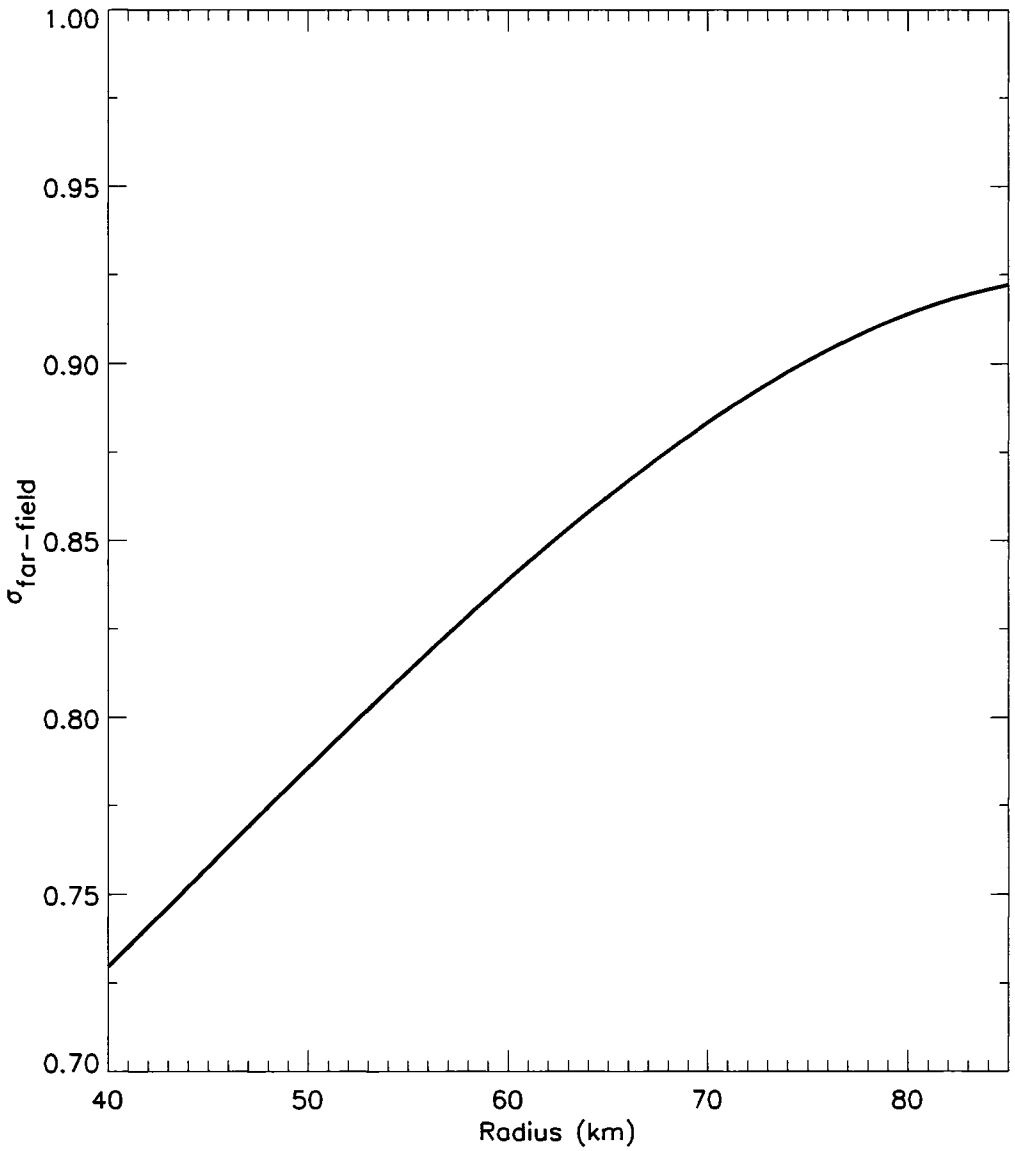

Figure 3.25: Values of the fraction of downward mass flux in the far-field, $\sigma_{\text{far-field}}$ for the range of wind profiles shown in Fig. 3.23. The abscissa denotes the variable 5-region model parameter r_4.

Chapter 4

IDEALIZED CLOUD MODEL EXPERIMENTS

4.1 Introduction

In Chapters 2 and 3, we applied a simple, 2D rapid filamentation theory to vorticity and passive tracers and explored observations of forming and mature TC moats. However, our rapid filamentation hypothesis and experiments still leave questions surrounding how actual deep, convective clouds interact with the local kinematic and thermodynamic environments that lead to moats. To help address these issues, idealized cloud-resolving mesoscale model simulations are discussed in this chapter.

We will specifically explore the impact of hurricane-like horizontal and vertical shears and thermodynamics on convective clouds. For maximal simplicity, we only consider shears of the tangential wind. In real TCs containing one eyewall, tangential wind profiles exhibit both horizontal and vertical shears outside of the primary eyewall in accordance with a warm-core vortex structure and thermal wind balance. For example, Fig. 4.1 provides isopleths of the axisymmetric tangential winds derived from flight-level data taken at five different levels in Hurricane Hilda (1964) (Schubert and Hack, 1983). Outside of the primary eyewall, which is near the radius of maximum wind (RMW), negative vertical shear exists throughout the depth of the troposphere and is particularly pronounced above 800 hPa. Anticyclonic, horizontal shear also exists throughout the troposhere outside of the RMW. Finally, while shear of the tangential wind results from the axisymmetric vortex structure, shear can result from rainbands and other asymmetries, as well.

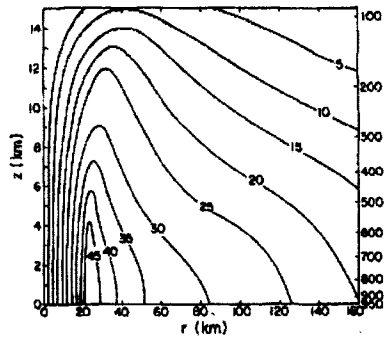

Figure 4.1: Azimuthal profile of tangential wind (m s^{-1}) based on aircraft data collected at five levels in Hurricane Hilda (1964). This figure was taken from Schubert and Hack (1983) and originally based on data described in Hawkins and Rubsam (1968).

The secondary circulation associated with a TC vortex usually features strong inflow, often exceeding 25 m s^{-1}, near the surface and this low-level inflow adds significant low-level vertical shear to the kinematic environment produced by a strong TC. Throughout the troposphere, inflows covering deeper layers and a typical broad layer of outflow aloft also add to this radial component of vertical shear. As an example of real-world complexity, Powell (1990a) plotted flight-level Doppler radar derived, rainband-relative wind hodographs from hurricane rainband regions (Fig. 4.2). (The tangent of a hodograph curve gives the vertical shear of the horizontal wind.) Powell's hodographs are constructed over 40 × 40 × 10 km sections surrounding significant rainbands in Hurricanes Josephine (1984) (Fig. 4.2a) and Earl (1986) (Fig. 4.2b). Although these bands spiral inward, they are strongly parallel to the azimuthal flow. The substantial crossband component of the wind implies that radial flows can contribute greatly to the vertical shear experienced by convective elements in rainbands. Nonetheless, for simplicity in our exploratory convection study, vertical shear of the radial wind is neglected. Adding this component of shear to our experimental setup will be the subject of future research.

Because of broad societal interests in predicting and understanding severe mid-latitude convective storms (e.g., Wilhelmson and Wicker, 2001) and climatologically

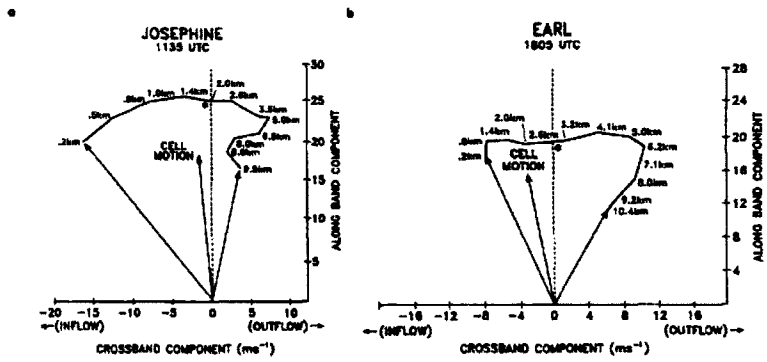

Figure 4.2: Flight-level Doppler radar-derived, band-relative hodographs of the wind from regions asurrounding rainbands in Hurricanes (a) Josephine (1984) and (b) Earl (1986). This figure was taken from Powell (1990a).

important tropical convective systems, the response of convection to vertical shears has been documented at length by the convective storms modeling community over the last four decades. For example, Rotunno and Klemp (1982; 1985) showed that sufficiently strong unidirectional vertical shear can split supercells through dynamic pressure perturbations (Schlesinger, 1980) associated with midlevel rotation. Such rotation originates from the tilting of the horizontal vorticity associated with the ambient vertical shear. Curved hodographs favor the dominance of one cell after a split (e.g., Rotunno and Klemp, 1982). Small tornadic supercells are often found in outer TC rainbands in high-shear, low convective available potential energy (CAPE) environments (e.g., McCaul, 1987; McCaul and Weisman, 1996). McCaul and Weisman (1996) demonstrated that nearly moist adiabatic lapse rates can support intense low-level updrafts because of dynamic pressure gradient accelerations. The morphology of squall lines is also shown to strongly depend on vertical shear (e.g., Rotunno and Weisman, 2004), where low-level shear and cold pool strength, in particular, are essential factors governing the severity of squall lines.

Because of the relatively restricted applicability, much less attention has been paid to the study of convection in horizontal shear and in the dual presence of horizontal and vertical shears. Published material has focused on idealized convection

and has yet to explicitly address deep, convective clouds in deep-layer horizontal shear. Davies-Jones (1971) found that thermal convection in a horizontal plane Couette flow organizes convection into longitudinally elongated cells nearly parallel to the flow. A more recent study along similar lines addressed a phase space of conditions that lead to different convective regimes including cellular modes, transverse bands, and longitudinal bands (Yoshikawa and Akitomo, 2003). Yoshikawa and Akitomo found that, with horizontal shear, rapidly rotating regimes can support transformation of cellular convection to longitudinal bands via transverse bands. Another idealized, theoretical investigation by Hart (2000) revealed that weak convection is suppressed in sufficiently strong cyclonic, horizontal shear near a strong vortex core, but can be enhanced by inertial instability outside an RMW because of anticyclonic shear and centrifugal accelerations, although his study was not applied to full nonlinear, 3D cloudy convection. Some applications have studied deep, moist convection in regions of low-level horizontal shear to study the development of misocyclones and subsequent non-supercell tornadoes (e.g., Lee and Wilhelmson, 1997). In Lee and Wilhelmson's numerical simulations, shearing and convective instabilities along a region of strong low-level horizontal shear drove misocyclone development, which ultimately contributed to deep convection and tornado development. However, little was revealed about the morphology of convection in an environment of deeper, hurricane-like horizontal shears.

As a somewhat disparate community, TC scientists are interested in the fundamental dynamics governing TC rainbands since rainbands are known to both intensify and weaken TCs through myriad known and proposed physical mechanisms. Typical spiral rainbands often consist of large stratiform precipitation regions with smaller-scale convective cells possessing various degrees of organization (Barnes et al., 1991; May, 1996). Such bands are often associated with midlevel jets (Willoughby et al., 1984; Jorgensen, 1984; Marks, 1985; May et al., 1994; Samsury and Zipser, 1995).

Rainbands are noted to be associated with enhanced PV (e.g., Guinn and Schubert, 1993; May and Holland, 1999) and may therefore help spin up a secondary eyewall. As pointed out in the introduction, rainband activity can signify convectively-coupled vortex Rossby waves, which can help accelerate the mean flow outside of a primary eyewall at preferred radii.

Many essential rainband dynamics have been connected to their extensive stratiform regions. In fact, many similarities between rainbands and tropical mesoscale convective systems have been pointed out. Much like the trailing stratiform regions in tropical MCSs (Gamache and Houze, 1982; May and Rajopadhyaya, 1996), rainband stratiform regions exhibit mesoscale updrafts above the melting level and downdrafts below. Similar to the convective mesoscale vortex study of Raymond and Jiang (1990), it has been proposed that heating in the stratiform region of rainbands provides a mechanism for PV production (May et al., 1994), which could be important in the formation of a mid-level jet. Using a full-physics simulation of a TC, Franklin et al. (2006) demonstrated that upward tilting of horizontal vorticity by diabatic heating gradients, including convective elements in the rainband, induces a PV dipole that accelerates tangential flow and a mid-level jet. Through sensitivity experiments, they found that evaporative cooling is necessary for the generation of enhanced anticyclonic vorticity and a mid-level jet. Further, Franklin et al. (2006) show that the vorticity patterns created by convective dynamics modulate the storm's mean PV gradient and can generate vortex Rossby waves.

The following results add new, fundamental insights into the general dynamics of horizontally sheared convection. Furthermore, previously unexplored PV generation mechanisms in TCs are revealed in the context of secondary eyewall and moat formation. In this Chapter, the idealized model setup describing the background kinematic and thermodynamic fields and our methods of analysis are described in Section 4.2. Results of our experiments showing the response of convection to ver-

tical and horizontal shears are summarized in Section 4.3. Finally, the sensitivities of sheared convection to background thermodynamic conditions is presented in Section 4.4.

4.2 Methodology

4.2.1 Mesoscale model

We chose the Regional Atmospheric Modeling System (RAMS) version 4.3 (Cotton et al., 2003) for our idealized convection study. Used extensively in cloud dynamics studies, RAMS is 3D, nohydrostatic, and compressible. RAMS is formulated on the Arakawa staggered C grid (Arakawa and Lamb, 1981). Wind advances in time via the leapfrog scheme while scalars are integrated with the forward scheme. Perturbation Exner function tendencies incorporate a time split scheme similar to Klemp and Wilhelmson (1978a).

In all convective experiments, one grid is chosen to prevent the errors inherent to nesting. Grid spacing of 500 m is utilized over one 125 km wide horizontal grid on the f-plane. In the vertical, a stretched Cartesian coordinate is employed over a depth of 25 km, which contains a grid spacing of 160 m near the surface; spacing is progressively stretched by a factor of 1.065 between overlying gridpoints until vertical grid spacing of 500 m is achieved. The time step is 2 s. All simulations use a seven-species, one-moment microphysics scheme (Walko et al., 1995). The microphysical species are water vapor, cloud water, rain, pristine ice, snow, aggregates, graupel, and hail. For maximum simplicity, we neglect radiation and assume a free slip lower boundary condition in all simulations. A Rayleigh friction layer is used for the top five levels of the model domain to limit reflection of gravity waves off the rigid model lid. Lateral boundaries use the Klemp-Wilhelmson condition, which means the normal velocity component is specified at the lateral boundary. However, we force the tendency of the zonal wind at the east and west boundaries to zero in order to eliminate spurious inflow

that occurs with purely meridional flow. Such inflow is amplified by the fact the time splitting scheme is not mass conserving. Subgrid-scale turbulence is parameterized according to a Smagorinsky (1963) scheme with stability modifications of Lilly (1962) and Hill (1974).

4.2.2 Initialization and experiments

The initial thermodynamic profile is composited from four dropsondes obtained outside the core of Category 5, Hurricane Isabel (2003) on 13 September. To account for the upper levels, a proximity sounding from San Juan, Puerto Rico is carefully blended into the upper portion of the thermodynamic profile. The dropsonde data were relegated to altitudes below 700 hPa and were taken at distances between 150 and 250 km from the center. The resulting composite vertical profile of temperature, dew point, and a hypothetical undilute surface-based parcel path temperature is provided in Fig. 4.3. In this sounding, the surface-based CAPE is 2067 J kg^{-1} and the convective inhibition (CIN) is only 1 J kg^{-1}. It also important to note there is dry, unstable air aloft and nearly moist-neutral low-levels. There is some uncertainty in how representative this thermodynamic sounding is to the outer core of a strong hurricane, especially in middle and upper levels, but we the general morphology of sheared convection to be applicable to multitudinal thermodynamic environments. After carrying out a suite of control experiments with this sounding, we perform some sensitivity experiments by making changes to the sounding's moisture profile and low-level instability. These results are summarized in Section 4.4.

In the idealized spirit of this study, cumulonimbus convection is initialized with a warm bubble. For the initial 200 s of each experiment,

$$H(x,y,z) = \begin{cases} \alpha \cos^4\left(\frac{\pi r}{2r_o}\right) \sin\left(\frac{\pi z}{z_o}\right) & \text{if } r \le r_o \text{ and } z \le z_o \\ 0 & \text{otherwise} \end{cases} \tag{4.1}$$

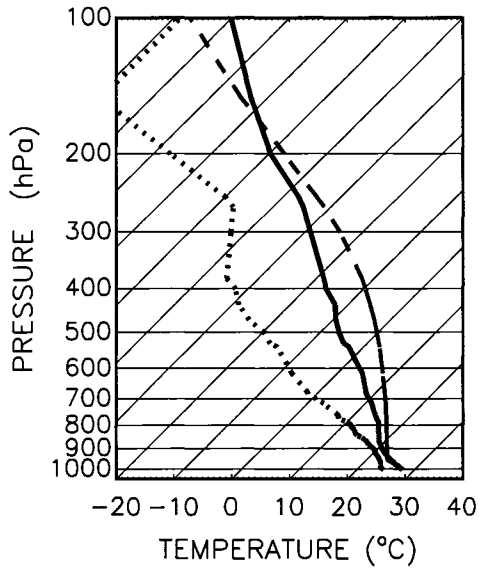

Figure 4.3: Composite vertical profile of dew point (dashed; °C), temperature (solid; °C) and hypothetical, undilute, surface-based parcel path temperature (dotted; °C).

is added to the ice-liquid potential temperature tendency, where $r = \sqrt{x^2 + y^2}$ is the horizontal radius from the center of the warm bubble, z is the physical height above the surface, $r_o = 27.5$ km, $z_o \approx 1.2$ km, and $\alpha = 0.01$, yielding a net 2 K bubble. Future research may consider more sophisticated storm initiation techniques such as simulating the effects of vortex Rossby wave forcing or some other low-level forcing mechanisms representative of low-level convergence areas in real TCs.

Using the thermodynamic profile shown in Fig. 4.3, we complete a suite of numerical experiments by systematically varying vertical and horizontal hurricane-like shear profiles. These shears may be interpreted as approximate shears of the tangential wind due to a mean TC vortex. The shear could also be equally thought of as being composed of both a vortex contribution and a contribution from convective concentration of tangential winds by radial inflow (outflow) and low-levels (upper-levels) (e.g., Franklin et al., 2006). Regardless, the initial wind profile takes the form

$$v(x, y, z) = v_z z + v_x x + v_{\text{ref}}, \tag{4.2}$$

where v_z is the vertical wind shear, which remains constant up to 15 km and vanishes at higher altitudes, v_x is the constant horizontal wind shear, and v_{ref} is the wind offset formulated to minimize storm motion from the domain center. The 16 experiments vary v_z over the values of 0, 5, 10, and 20 m s^{-1} per 15 km and v_x takes on the values 0, -2, -4, and -6 $\times$ 10^{-4} s^{-1}. For notational convenience, these experiments are hereafter labeled as vXXhY, where XX=00, 05, 10, and 20 denotes the different values of v_z normalized by (15 km)$^{-1}$, and Y=0, 2, 4, and 6 represents the magnitudes of v_x normalized by -1×10^{-4}. Hereinafter, all simulations described so far define what will be referred to as the control experiments. The additional sensitivity experiments that are conducted by modifying either the temperature or dewpoint profile in the control sounding (Fig. 4.3) are carried out for cases v00h0, v20h0, v00h6, and v20h6. Further details regarding the modified soundings are provided in Section 4.4.

All experiments are initialized in geostrophic balance, where the horizontal shear

is introduced to the initial perturbation variables in RAMS and the vertical shear is applied to the model's basic state variables. These details are now elaborated upon. Leaving out turbulence and other source terms for the sake of discussion, the RAMS equations of motion and continuity are

$$\frac{\partial u}{\partial t} = -\mathbf{u}\cdot\nabla u - \theta_{vo}\frac{\partial \pi'}{\partial x} + f(v - v_z z - v_{\text{ref}}), \tag{4.3}$$

$$\frac{\partial v}{\partial t} = -\mathbf{u}\cdot\nabla v - \theta_{vo}\frac{\partial \pi'}{\partial y} - fu, \tag{4.4}$$

$$\frac{\partial w}{\partial t} = -\mathbf{u}\cdot\nabla w - \theta_{vo}\frac{\partial \pi'}{\partial z} + B, \tag{4.5}$$

and

$$\frac{\partial \pi'}{\partial t} + \frac{R\pi_o}{c_v\rho_o\theta_{vo}}\nabla\cdot(\rho_o\theta_{vo}\mathbf{u}) = 0, \tag{4.6}$$

where u, v, and w are the two horizontal and vertical components, respectively, of the 3D wind, $\mathbf{u}$, $\theta_{vo} = \theta_{vo}(z)$ is the background virtual potential temperature, π' is the perturbation Exner function where $\pi = \pi_o(z) + \pi' = c_p(p/p_{oo})^{\kappa}$ is the total Exner function, $\pi_o = \pi_o(z)$ is the background Exner function, c_v and c_p are the specific heats at constant volume and pressure for dry air, respetively, p is the pressure, $p_{oo} = 10^5$ Pa is the reference pressure, $\kappa = R/c_p$, R is the gas constant for dry air, f is the constant Coriolis force, $B = g[\theta_v'/\theta_{vo} - (r_T - r_v)]$ is the buoyancy, g is the constant acceleration of gravity, θ_v' is the perturbation potential temperature, r_T and r_v are the total water and water vapor mixing ratios, and $\rho_o = \rho_o(z)$ is the background density. The vertical shear component of the flow is seen on the right-hand side of (4.3). The horizontal shear is introduced to the perturbation variables in (4.3)–(4.6). Assuming geostrophic balance,

$$fv_h \equiv fv_x x = \theta_{vo}\frac{\partial \pi_h'}{\partial x} \tag{4.7}$$

for the initial horizontal flow $v_h(x) = v_x x$, then the balanced component of the perturbation Exner function belonging to the horizontal shear, namely π_h', can be found. Integrating (4.7) from the left-hand side of the domain, at x_L, we obtain

$$\pi_h'(x,z) = \frac{1}{2\theta_{vo}} fv_x\left(x^2 - x_L^2\right). \tag{4.8}$$

In addition, the initial horizontal flow is assumed to be in hydrostatic balance; that is,

$$\frac{\partial \pi'_h}{\partial z} = g\frac{\theta'_{vh}}{\theta^2_{vo}}, \tag{4.9}$$

thus,

$$\theta'_{vh} = -\frac{1}{2g} f v_x \left(x^2 - x_L^2\right) \frac{d\theta_{vo}}{dz}. \tag{4.10}$$

The initial horizontal gradients, including shear, are well maintained throughout the simulations.

In all experiments, the simplifying assumption that the background absolute vorticity $\zeta_a = v_x + \bar{\zeta} + f$ is equal to the constant 1×10^{-4} s^{-1} is made, thus ensuring inertial stability, where v_x is the parameter described in (4.2), $\bar{\zeta}$ is the constant, local background hurricane vorticity, and $f = 5 \times 10^{-5}$ s^{-1}. This is done to guarantee that convection in each experiment experiences the same absolute vorticity.

The assumption of constant background absolute vorticity requires adjusting the model's constant Coriolis parameter when horizontal shear is added to the initial condition. Careful interpretation of the model equations is necessary under this assumption. Adjusting the Coriolis force is equivalent to putting the model grid in a reference frame rotating at the rate $\mathbf{\Omega} = \bar{\zeta}/2\hat{\mathbf{k}}$ around a circular vortex center at a radius where the average relative vorticity is $\bar{\zeta}$ and where $\hat{\mathbf{k}}$ is the upward pointing unit vector. Noting $\mathbf{u}_I = \mathbf{u}_R + \mathbf{\Omega} \times \mathbf{r}$, where $\mathbf{u}_I$ and $\mathbf{u}_R$ are the 3D wind vectors in the inertial and rotating reference frames, respectively, and $\mathbf{r}$ is the horizontal position vector, and further assuming a steady-state background vortex, the original inertial frame of reference can be related to the new rotational frame of reference:

$$\left(\frac{D\mathbf{u}_I}{Dt}\right)_I = \left(\frac{D\mathbf{u}_R}{Dt}\right)_R + \bar{\zeta}\hat{\mathbf{k}} \times \mathbf{u}_R - \frac{1}{4}\bar{\zeta}^2\mathbf{r}, \tag{4.11}$$

where $D/Dt = \partial/\partial t + \mathbf{u} \cdot \nabla$ is the material derivative in the inertial or rotating reference frames (e.g., Pedlosky 1987). Since the basic state in the current formulation of RAMS depends only on height, the centripetal term, $-(1/4)\bar{\zeta}^2\mathbf{r}$, can be

absorbed into the pressure gradient and buoyancy terms in the equations of motion. Future research should incrementally increase the level of sophistication in environmental conditions to further examine the salient effects convective elements experience in a hurricane, including more sophisticated vorticity and shear profiles. The simple vorticity formulation that we use in this study allows us to isolate basic shear effects on convection. It also enables us to employ a local Cartesian modeling in the framework of a cylindrical problem.

4.2.3 Methods of analysis

Before exploring the details of the control experiments, a few important definitions are provided. First, a cloud updraft is strictly defined to exist where both $w \geq 0.5$ m s^{-1} and $q_{\text{cond}} \geq 0.5$ g kg^{-1}, where w is the vertical velocity and q_{cond} is the total cloud condensate, which includes all liquid and ice forms of water. Likewise, a cloud downdraft is defined for $w \leq -0.5$ and $q_{\text{cond}} \geq 0.5$ g kg^{-1}. In the past, similar definitions have been used to study cumulonimbus dynamics (e.g., Cohen 2000), but our definition restricts cloud updrafts and downdrafts to regions of significant levels of condensate (i.e., cloudy and precipitating updrafts and downdrafts). As in Cohen (2000), our threshold for vertical motion, $|w| \geq 0.5$, helps exclude cirrus anvils from our analysis of relevant cloud circulations. Also, our threshold for q_{cond} is higher than in Cohen (2000) in order to eliminate gravity waves from the analysis. Subjective analysis of model output suggests the significant portions of the cloud circulation are captured by this definition. Future volume averages are defined over volumes meeting these updraft and downdraft criteria. Finally, a convective lifecycle timescale, τ_{l}, is defined as any period of time in which cloud updrafts reach or exceed mid-levels (5.5 km) of the troposphere.

Because the cold pool is an important factor in the control and sensitivity experiments, it is worthwhile to quantify the strength of the cold pool. To this end,

we define an average cold pool deficit at the lowest model level, z_1, as follows:

$$\langle \Delta\Gamma \rangle_c = \frac{1}{\mathcal{A}} \int \int_{\mathcal{A}} [\Gamma_i(x, y, z = z_1) - \Gamma(x, y, z = z_1)] \; dx \; dy, \tag{4.12}$$

where Γ is some variable at the model level $z = z_1$, Γ_i is the initial Γ field, $\mathcal{A}$ is the area over which $\theta(x, y, z_1) < \theta_i(x, y, z_1)$, and θ is the potential temperature. If $\Gamma = \theta$, then (4.12) represents the average strength of the cold pool. This average deficit definition will also be applied to water vapor, q_v, and equivalent potential temperature, θ_e in the following analysis.

We carry out a dynamic pressure perturbation analysis to better quantify important dynamics in sheared convection. As in (4.3)–(4.5), turbulence and diffusion are ignored. There are pressure perturbations and buoyancy associated with the background horizontal shear, so π'_h and θ'_{vh} are subtracted from the RAMS output of π' and θ'_v in order to focus on cloud-induced perturbation pressures. Subtracting π'_h from (4.3)–(4.5) requires subtracting off v_h from the Coriolis term in (4.3). Finally, in this diagnosis, the assumption that the continuity equation takes the form

$$\nabla \cdot (\rho_0 \theta_{vo} \mathbf{u}) = 0 \tag{4.13}$$

is made.

Following Rotunno and Klemp (1982), we develop a diagnostic equation for the pressure perturbation, π'_r, which is the residual pressure perturbation after π'_h has been subtracted from π'. Taking the divergence of (4.3)–(4.5) and incorporating (4.13), we obtain

$$\begin{aligned} \nabla \cdot (\rho_o \theta_{vo}^2 \nabla \pi'_r) &= -\nabla \cdot (\rho_o \theta_{vo} \mathbf{u} \cdot \nabla \mathbf{u}) \\ + f \rho_o \theta_{vo} &\left(\frac{\partial (v - v_i)}{\partial x} - \frac{\partial u}{\partial y} \right) + \frac{\partial (\rho_o \theta_{vo} B_r)}{\partial z}, \end{aligned} \tag{4.14}$$

where $B_r = B - B_h$ and $B_h = g(\theta'_{vh}/\theta_{vo})$. The three terms on the right account for the dynamic component of the pressure field, π'_d, the Coriolis part of the pressure field, π'_c, and the buoyant contribution to the pressure field, π'_b. Together these pressure field

components comprise the total residual pressure perturbation field, π'_r. The dynamic pressure perturbations are diagnosed from

$$\nabla \cdot (\rho_o \theta_{vo}^2 \nabla \pi'_d) = -\nabla \cdot (\rho_o \theta_{vo} \mathbf{u} \cdot \nabla \mathbf{u}) = -\rho_o \theta_{vo} \left[\left(\frac{\partial u}{\partial x} \right)^2 + \left(\frac{\partial v}{\partial y} \right)^2 + \left(\frac{\partial w}{\partial z} \right)^2 \right] + \rho_o \theta_{vo} \left[w^2 \frac{d^2 \ln (\rho_o \theta_{vo})}{dz} \right] - 2\rho_o \theta_{vo} \left(\frac{\partial v}{\partial x} \frac{\partial u}{\partial y} + \frac{\partial u}{\partial z} \frac{\partial w}{\partial x} + \frac{\partial v}{\partial z} \frac{\partial w}{\partial y} \right), \tag{4.15}$$

the Coriolis pressure perturbations are diagnosed from

$$\nabla \cdot (\rho_o \theta_{vo}^2 \nabla \pi'_c) = f \rho_o \theta_{vo} \left(\frac{\partial (v - v_i)}{\partial x} - \frac{\partial u}{\partial y} \right), \tag{4.16}$$

and the buoyant pressure perturbations can be obtained from

$$\nabla \cdot (\rho_o \theta_{vo}^2 \nabla \pi'_b) = \frac{\partial (\rho_o \theta_{vo} B_r)}{\partial z}. \tag{4.17}$$

It turns out the Coriolis pressure perturbations are insignificant in all our analyses and they are therefore neglected. Gauss-Seidel relaxation is used to solve for π'_d and π'_b is obtained as a residual.

Finally, vorticity budgets are computed for all sheared convection experiments. Neglecting diffusion, the vertical vorticity budget is

$$\frac{\partial \zeta}{\partial t} = -\mathbf{u} \cdot \nabla_2 \zeta - w \frac{\partial \zeta}{\partial z} - (\zeta + f) \nabla_2 \cdot \mathbf{u} - \left(\frac{\partial w}{\partial x} \frac{\partial v}{\partial z} - \frac{\partial w}{\partial y} \frac{\partial u}{\partial z} \right) + \frac{1}{\rho^2} \left(\frac{\partial \rho}{\partial x} \frac{\partial p}{\partial y} - \frac{\partial \rho}{\partial y} \frac{\partial p}{\partial x} \right). \tag{4.18}$$

From left-to-right, the terms on the right-hand side of (4.18) represent horizontal advection of vorticity, vertical advection of vorticity, convergence of absolute vorticity, tilting of horizontal vorticity, and the baroclinic generation of vorticity.

4.3 Shear effects on convection

4.3.1 A basic state of rest

We now summarize some of the results of the control experiments. In experiment v00h0, simulated deep, moist convection in its motionless basic state evolves

along a well documented path. The heat plume resulting from the initial warm bubble grows upright with an axisymmetric overturning circulation. As in all of our control experiments, free convection is initiated around 0.8 h as the heat plume overcomes the small region of convective inhibition. This convective updraft quickly penetrates the tropopause, reaching a maximum height of $h_{\max} = 14.9$ km. Reflective of the artificial heating, although consistent with some observed "hot towers," the maximum updraft speeds achieve speeds exceeding 35 m s^{-1} (Table 4.1). However, the volume-average updraft speed ranges from 2 to 9 m s^{-1} over the course of the convective storm's lifetime. As the cloud matures, precipitation falls through the center of the storm and an axisymmetric cold pool forms at low levels. Strong convergence at the edge of the resulting cold pool initiates tertiary, convective cells symmetrically around the cold pool center. The total convective lifetime, τ_l, is 1.8 h for this event, but the initial convective cloud lasts approximately 1 h. The evolution of this convective event is captured in a plot of total cloud condensate (Fig. 4.4). We recall that total cloud condensate contains both cloud and precipitation.

Figure 4.5a shows that, in experiment v00h0, the cold pool strength, $\langle \Delta\theta \rangle_c$, quickly increases about 1.4 K by 1.7 h, and then progressively weakens as the cold pool grows in size. On the other hand, the cold pool initially acquires higher θ_e (Fig. 4.5b) due to water vapor convergence as the updraft matures. This surfeit decreases gradually as the cold pool matures, and by about 2.5 h, the water vapor excess decreases sufficiently so $\langle \Delta\theta_e \rangle_c$ becomes positive. A water vapor budget calculation shows downdrafts, which fall through the center of a relatively protected updraft core, produce modest water vapor decreases in the cold pool. Overall, strong low-level mass convergence at the edge of the axisymmetric cold pool keeps water vapor mixing ratios elevated in the cold pool areal average calculated via (4.12).

	τ_l	h_{max}	w_{max}	w_{min}
v00h0	1.8	14.9	37.8	-9.2
v05h0	1.0	14.4	37.3	-13.8
v10h0	0.9	14.4	34.8	-13.6
v20h0	0.9	14.4	32.9	-11.3
v00h2	0.9	12.9	30.8	-9.1
v05h2	1.0	13.4	31.6	-8.9
v10h2	0.9	13.4	33.4	-9.5
v20h2	1.1	13.4	31.4	-10.4
v00h4	1.0	10.9	22.6	-6.2
v05h4	1.0	10.9	26.4	-7.5
v10h4	1.0	11.9	26.2	-9.3
v20h4	0.9	12.4	24.3	-7.6
v00h6	0.2	8.4	12.3	-4.0
v05h6	0.2	9.4	13.3	-3.7
v10h6	0.4	9.9	13.3	-3.9
v20h6	0.5	9.4	15.2	-3.9

Table 4.1: Convective lifetimes, τ_l (hr), maximum height of convection, h_{max} (km), maximum vertical speed, w_{max} (m s^{-1}), and minimum vertical speed, w_{min} (m s^{-1}) for all experiments.

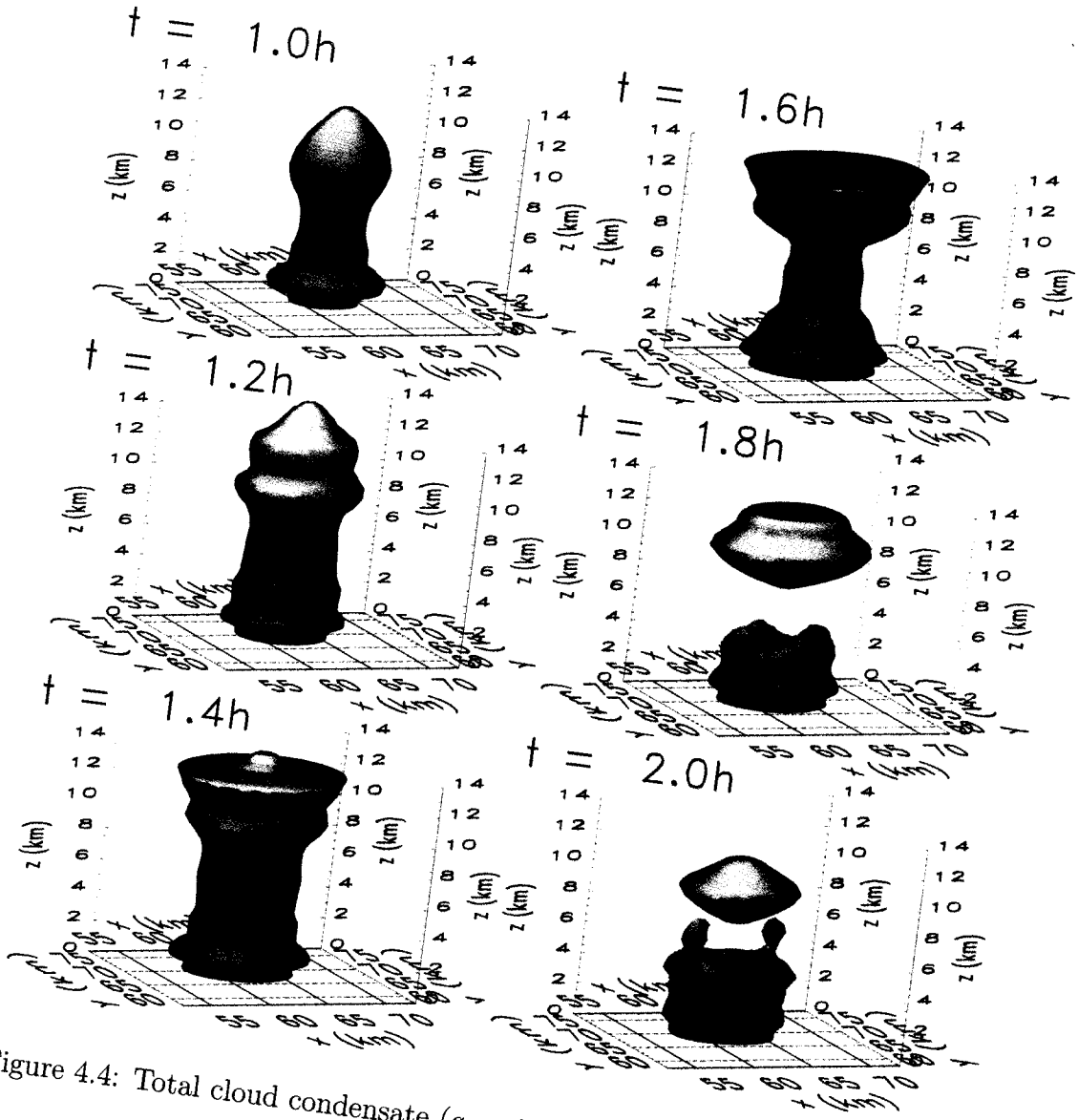

Figure 4.4: Total cloud condensate ($q_{\text{cond}} \geq 0.5$ g kg^{-1}) for experiment v00h0.

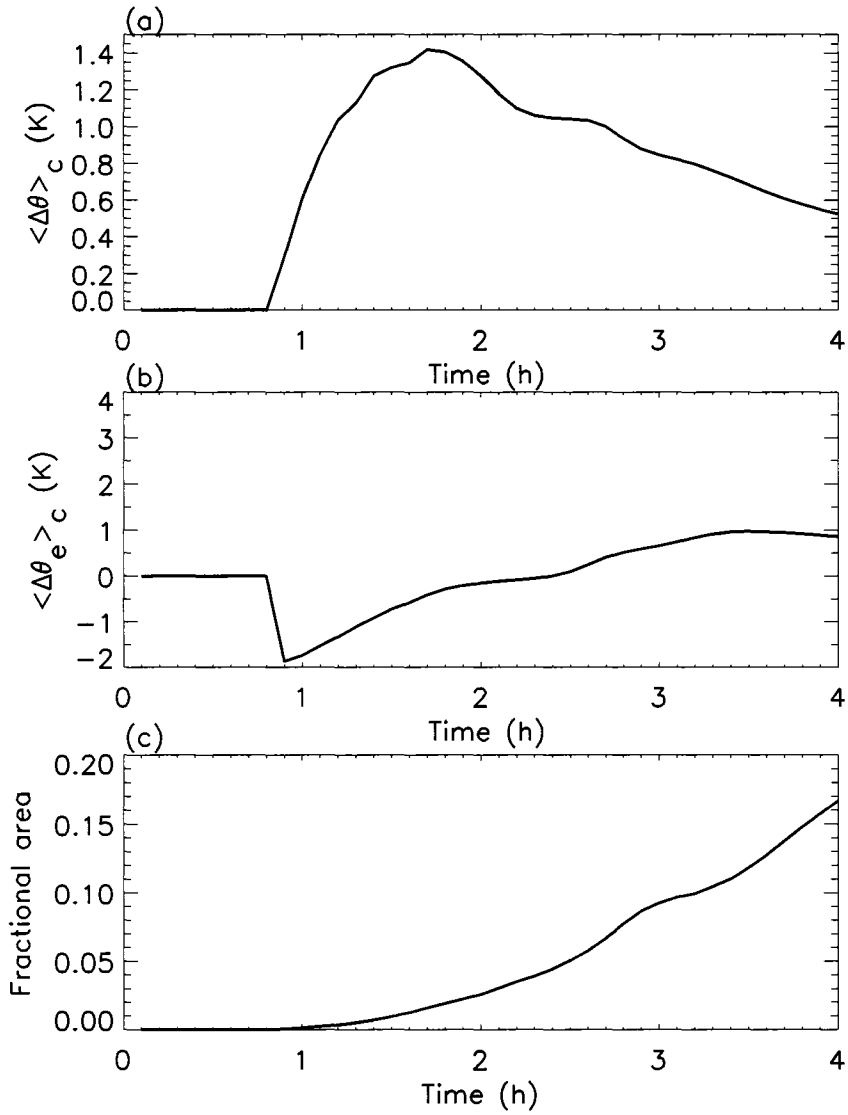

Figure 4.5: (a) Cold pool strength as defined in (4.12) for experiment v00h0, (b) corresponding θ_e deficits, and (c) the fraction of domain covered by the cold pool.

4.3.2 Vertical shear

Next, we revisit vertically sheared convection. Since convective plumes in unidirectional vertical wind shear are well documented in classic cloud dynamics literature (e.g., Wilhelmson and Klemp, 1978; Klemp, 1987), our overview of the vertical shear results in this section is brief, but we provide sufficient context for later discussion. In our control experiments v05h0, v10h0, and v20h0, the vertical overturning circulation associated with a developing cumulonimbus is tilted downshear with height. Figure 4.6 shows the total cloud condensate for experiment v20h0 and illustrates the downshear tilt of the cloud. With increasing shear, the simulated updrafts become more horizontally distorted from circular symmetry. When sufficiently strong shear is present, as seen around 1.6 h in v20h0, updraft splitting occurs (Fig. 4.6). Downdrafts extend further downshear from the cloud center as the vertical shear increases.

According to Fig. 4.7a, vertical shear does not have a significant impact on the volume-averaged updraft speed. However, one may argue that unsheared convection peaks earlier than sheared convection. Similar to unsheared convection, average updraft speeds vary between 2 and 9 m s^{-1}. Nevertheless, there is a slight decrease in the maximum updraft speeds from 37.8 to 32.9 m s^{-1} as the vertical shear increases (Table 4.1). Also, $w_{\min}$ is greater in magnitude in the presence of shear. Figure 4.7d provides a more detailed overview of downdraft behavior, where the volume-average downdraft maximizes during initial updraft growth. During this stage, the downdrafts are progressively weaker with increasing shear. Following this burst, stronger downdrafts are observed for increased vertical shear.

Despite the fact that vertical shear increases the surface area of an updraft (Fig. 4.7c), Fig. 4.7e demonstrates that the volume-average buoyancy values for the updrafts remain roughly comparable for all vertical shear cases, except when secondary convection is initiated in v00h0 around 1.6 h. These small differences agree with the small variance in average updraft speeds (Fig. 4.7a).

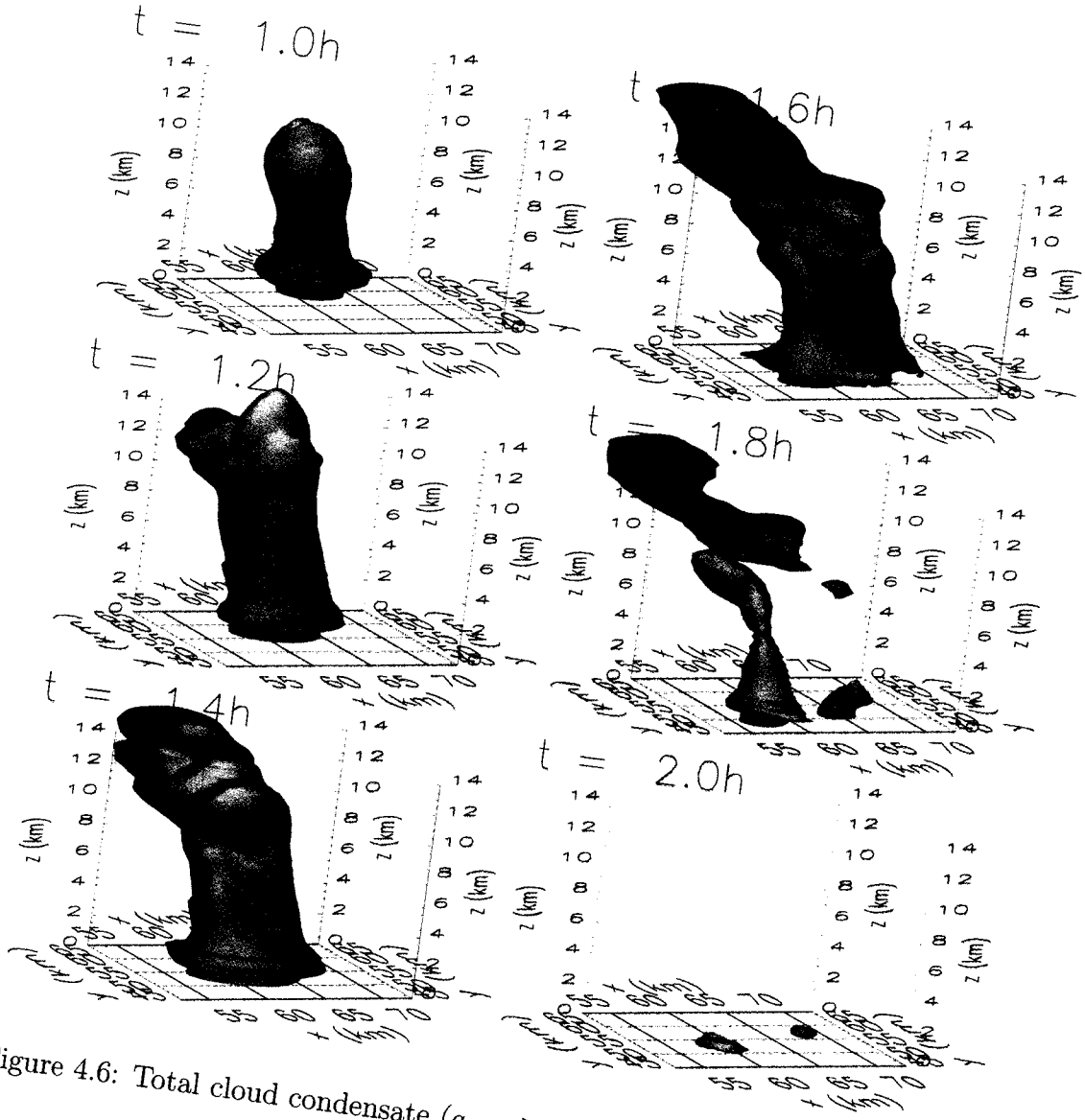

Figure 4.6: Total cloud condensate ($q_{\text{cond}} \geq 0.5$ g kg^{-1}) for experiment v20h0.

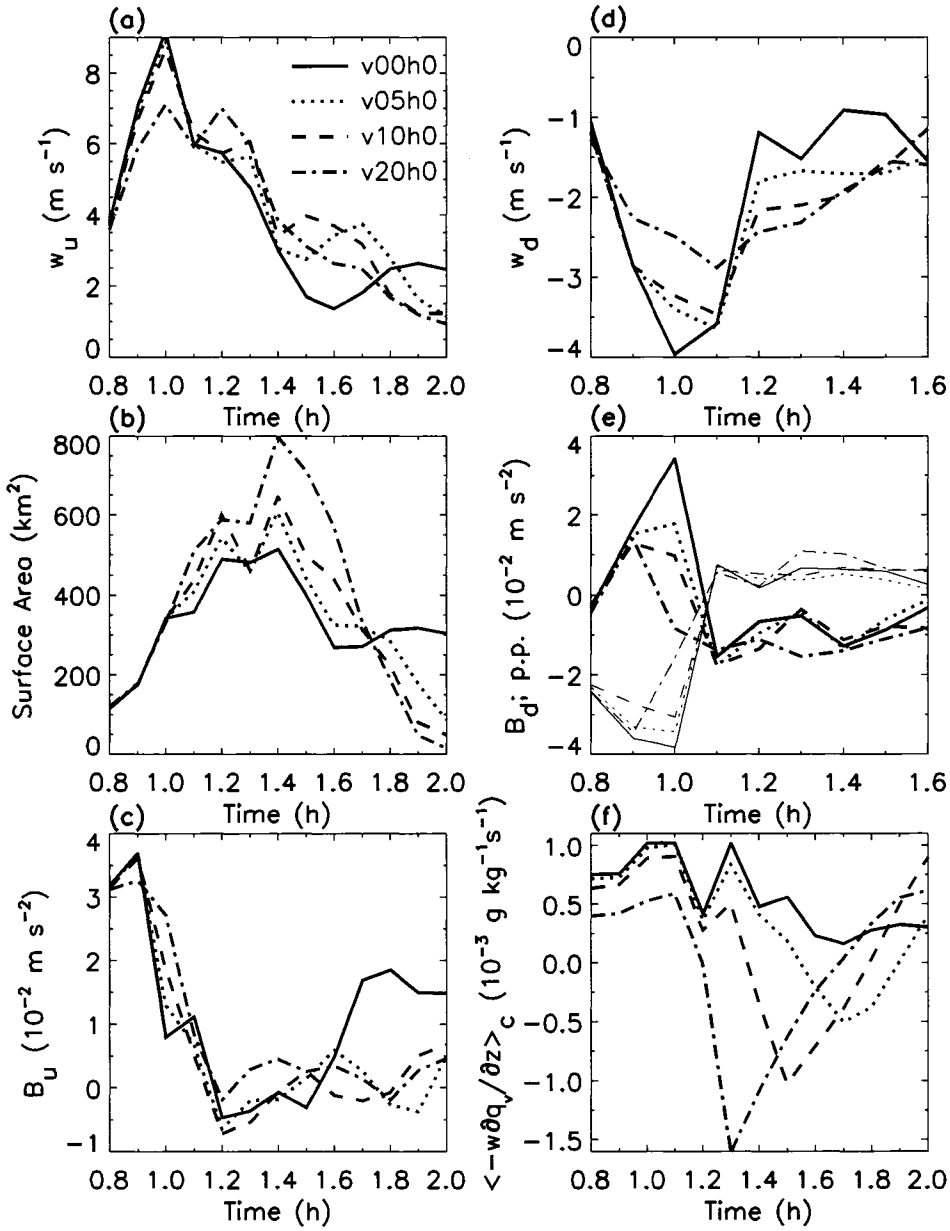

Figure 4.7: Updraft and downdraft averages for experiments v00h0 (solid), v05h0 (dotted), v10h0 (dashed), and v20h0 (dash-dotted), where (a) is the volume-average updraft speed, (b) is the volume-average downdraft speed, (c) is the surface area of the updraft, (d) is the volume-average downdraft buoyancy (thick) and vertical derivative of the storm induced perturbation pressure (thin), (e) is the volume-average updraft buoyancy, and (f) is the average vertical advection of water vapor in the cold pool.

Although there are no compelling trends in volume-average vertical motion fields (Fig. 4.7a), "nonlinear" dynamic pressure perturbations, which are especially pronounced in v20h0, contribute to storm splitting in experiments with larger vertical shear. Figure 4.8a shows an x-z cross section of vertical motion through the growing updraft of experiment v20h0 at 0.9 h. The updraft tilt is perpendicular to this cross section. Important terms in the vertical momentum equation (4.5) are also plotted in Fig. 4.8. It is apparent that buoyancy and buoyant pressure perturbation gradient forces dominate vertical accelerations (Figs. 4.8b,d). Nonetheless, the dynamic pressure perturbation gradient force (Fig. 4.8c) provides a substantial component of upward acceleration on the left and right flanks of the updraft in a manner consistent with Fig. 8 in Rotunno and Klemp (1982). Considering the bulk Richardson number results of Weisman and Klemp (1982) and our background CAPE which exceeds 2 kJ kg^{-1}, our vertical shear of 20 m s^{-1} (15 km)$^{-1}$ is still a marginal magnitude for long-lived supercells. Finally, although precipitation appears to accelerate splitting, a true quantification of this effect requires turning precipitation processes off and comparing the rates at which storms split.

The vorticity dynamics of our vertically sheared convection experiments verify behaviors that were documented in previous supercell dynamics literature (e.g., Klemp, 1987). As such, our summary is brief. Perpendicular to the vertical shear vector, anticyclonic and cyclonic vorticity form in the left and right halves of the sheared updraft (Fig. 4.9a). A vorticity budget is computed at an early time (0.6 h) into the simulation because it clearly captures the origin of the dipole in vorticity. Early on, the tilting term is a key term in the vorticity budget (Fig 4.9d). During this time, the total advection of vorticity (Fig. 4.9b), which is dominated by vertical advection, leads to increasing positive, vertical vorticity throughout the growing plume. This positive vorticity advection results from the low-level convergence of positive background vorticity (Fig. 4.9c). In agreement with Klemp and Wilhelmson (1978b),

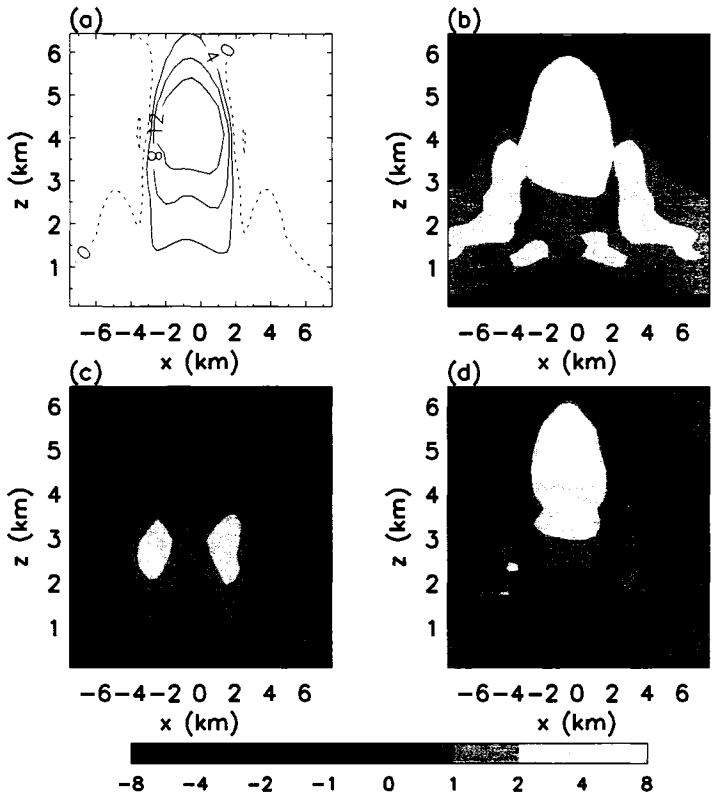

Figure 4.8: Vertical x-z cross-section of (a) vertical velocity (m s^{-1}), (b) buoyancy B (10^{-2} m s^{-2}), (c) dynamic perturbation pressure gradient acceleration ($-\theta_{vo}\ \partial\pi'_d/\partial z$) ($10^{-2}$ m s^{-2}), and (d) the sum of B and the buoyant perturbation pressure gradient acceleration ($B - \theta_{vo}\ \partial\pi'_b/\partial z$) ($10^{-2}$ m s^{-2}) for experiment v20h0 at 0.9 h.

the cyclonic vortex component of the updraft is therefore larger in magnitude than the anticyclonic vortex component due to inclusion of positive background absolute vorticity.

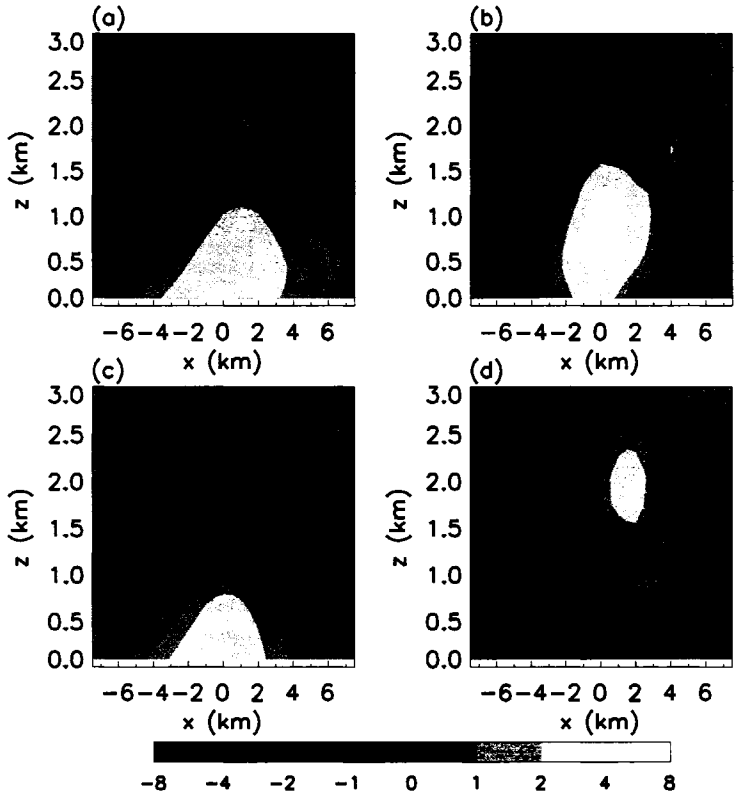

Figure 4.9: Vertical x-z cross-section of (a) vertical vorticity (10^{-4} s^{-1}), (b) total advection of vorticity (5×10^{-6} s^{-2}), (c) convergence of vorticity (5×10^{-6} s^{-2}), and (d) tilting of vorticity (5×10^{-6} s^{-2}) for experiment v20h0 at 0.6 h.

In contrast with the updraft behavior, downdrafts experience considerably more variability between experiments with different values of vertical shear (Fig. 4.7d). This behavior can be explained through a vertical momentum budget. Figure 4.7e shows the volume-average downdraft buoyancy (thick curves) and the volume-average downdraft perturbation pressure gradient (thin curves). During this period, precipitation is still forming and a primary downdraft has not matured. At midlevels, a primary negatively buoyant downdraft is formed downshear of the updraft as precipitation begins to fall. Near the top of the plume, significant downdrafts that are positively buoyant

form around the edge of the plume in response to a significant downward directed perturbation pressure gradient force around the updraft edges. The volume-average downdraft calculations in Fig. 4.7d,e are strongly biased toward this elevated plume downdraft during this convective burst. By 1.1 h, the updraft has matured and the primary downdraft materializes downshear of storm center throughout a deep layer. This downdraft forms more quickly in the presence of higher shear. As vertical shear increases, negative buoyancy also rises (Fig 4.7e) in the downdraft. These changes in buoyancy are related to the greater precipitation exposure to drier environmental air as the updraft tilts. The resulting evaporative cooling drives stronger downdrafts. Furthermore, the areal coverage of the downdraft increases with higher vertical shear. As a consequence of increased evaporative cooling and the increased areal coverage of downdrafts, the surface cold pool size grows substantially with increasing shear (Fig. 4.10c). While the average cold pool strength is similar for all our vertical shear cases (Fig. 4.10a), the $\langle \Delta\theta_e \rangle_c$ deficit varies nearly linearly between 0 K and 5 K between experiments v00h0 and v20h0 (Fig. 4.10b). Figure 4.7f shows the cold pool average vertical water vapor advection. Because of strong water vapor convergence near the edge of the cold pool, overall downward advection can be positive in the cold pool areal average as defined in (4.12). Nonetheless, it is evident from Fig. 4.7f elevated vertical shear leads to increased downward advection of drier air into the cold pool. While tertiary convection forms in v00h0, the vigorous cold pool, which is convectively stable, overwhelms vertically sheared convection and prevents secondary updraft development in experiments v05h0, v10h0, and v20h0. Between 1.5–1.7 h, the cold pool completely undercuts convection and diminishes the surface-based CAPE, which explains the relatively short timescales of the vertically sheared convection. Increased low-level shear (e.g., Weisman and Rotunno, 2004) could help prevent this detrimental cold pool from overtaking the instability available to convection.

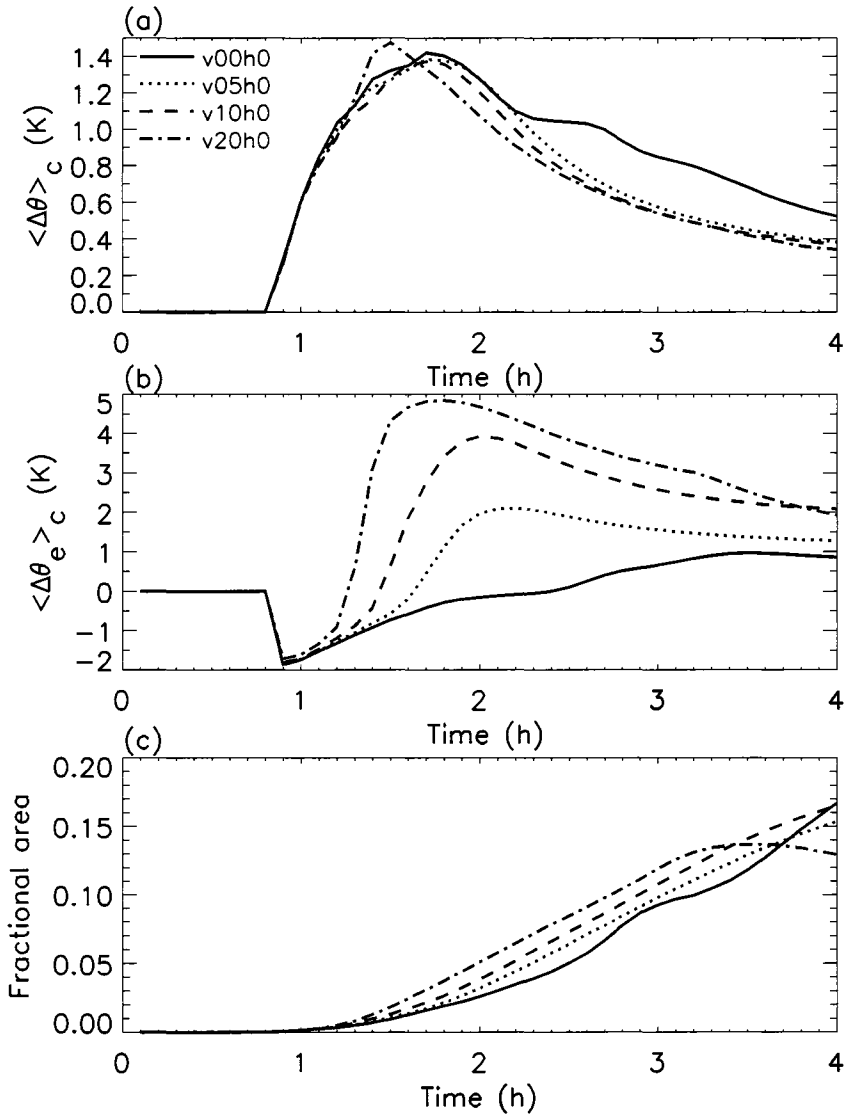

Figure 4.10: (a) Cold pool strength as defined in (4.12) (b) corresponding θ_e deficits, and (c) the fraction of domain covered by the cold pool for experiments v00h0 (solid), v05h0 (dotted), v10h0 (dashed), and v20h0 (dash dotted).

4.3.3 Horizontal shear

In experiments v00h2, v00h4, and v00h6, we isolate the effects of horizontal shear on the formation of a deep, convective plume. The time evolution of the clouds (Fig. 4.11) depicts a consistent picture for different values of v_x. Horizontally sheared updrafts experience two distinct regimes. The first regime sets up as the warm bubble is introduced into the domain. Although warm bubbles are used primarily to initiate deep, convective clouds, a lot can be learned from the early evolution of this bubble. In this first regime, the initial thermal becomes elongated into an ellipsoid. The strength of the horizontal shear governs the rate at which the thermal is elongated. Early in the warm bubble's lifetime, a banded overturning circulation develops and downward motion becomes restricted to the transverse flanks of the filamentary plume. In the second regime, deep, moist convection initiates from this elongating heat source as long as the horizontal shear is not too strong. For example, v00h6 barely succeeds at producing convection that reaches mid-levels, while v00h2 produces stronger and longer-lived convection (e.g., Table 4.1). When deep convection develops from the elongating plume, convection acquires a cellular nature along the band. When deep convection with intense updrafts is initiated, the convective overturning cycle is sped up. Soon after deep convection initiates, the updraft splits into two symmetric, but oppositely moving cells. Splitting occurs more readily in stronger shear. Each cell moves with its mean flow and continually experiences shearing deformation. Experiment v00h4 (middle column of Fig. 4.11) exhibits the most complex evolution. Here, a split occurs early on (around 1 h) and is followed by new cell development at the longitudinal ends of the expanding, elliptical cold pool. These younger cells dissipate by 1.6 h and weaker cells subsequently develop at the longitudinal ends of the cold pool. Convection is always suppressed on the transverse flanks of the banded system.

Horizontal shear diminishes most aspects of convection. Maximum cloud top heights decrease nearly linearly from 14.9 km to 8.4 km between experiments v00h0

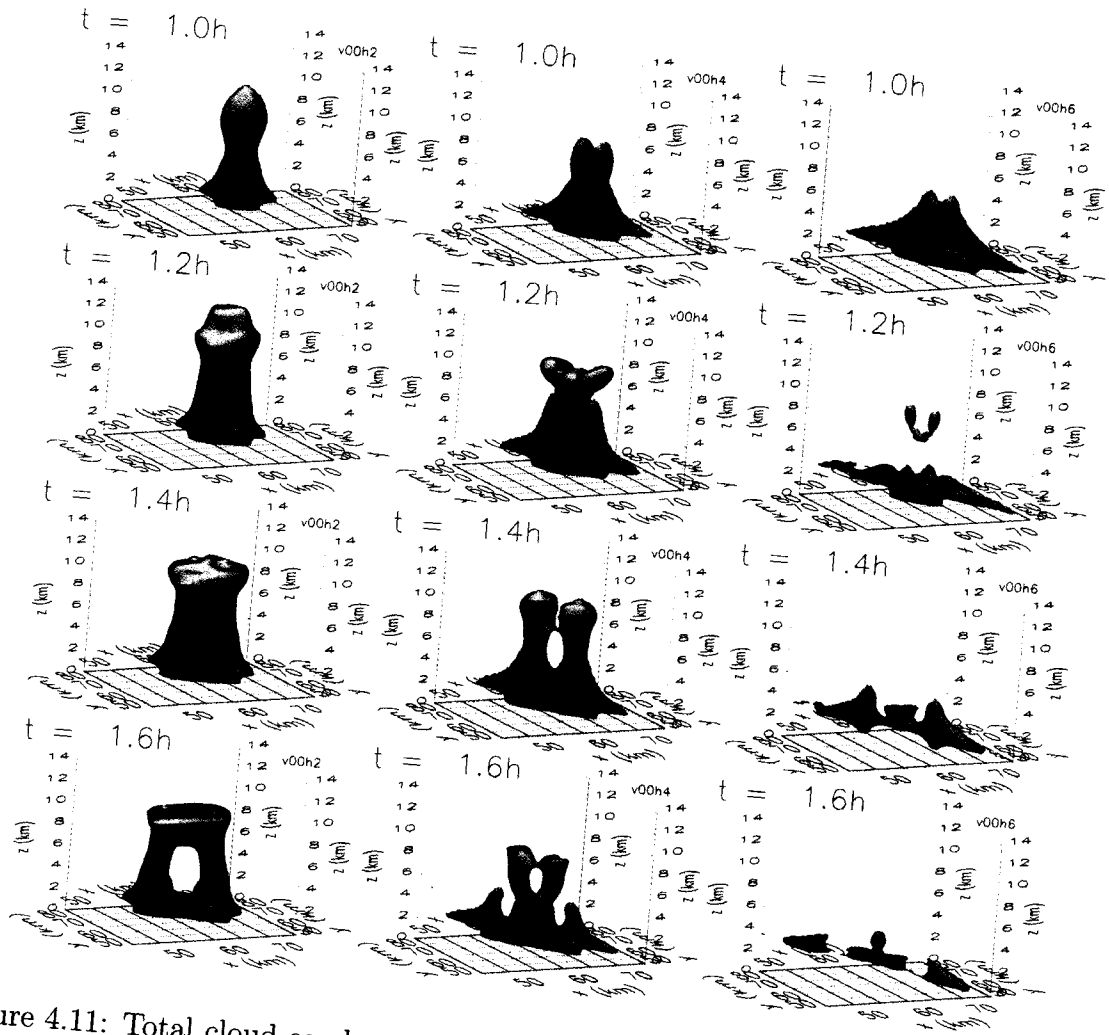

Figure 4.11: Total cloud condensate ($q_{\text{cond}} \geq 0.5$ g kg^{-1}) for experiments v00h2 (left column), v00h4 (middle column), and v00h6 (right column).

and v00h6 (Table 4.1). For the most part, volume-average updraft strength decreases monotonically with horizontal shear (Fig. 4.12a). These differences are most apparent right after convection commences. Cloud lifetimes are 1.8, 0.9, 1, and 0.2 h for experiments v00h0, v00h2, v00h4, and v00h6, respectively. Hence, a practical value of rapid filamentation for these experiments is $1/|-6\times10^{-4}| \approx 28$ min. The negative trends in cloud top height, vertical velocity, and lifetime are consistent with increased dry-air entrainment. As demonstrated in our calculation of the updraft surface area (Fig. 4.12) prior to storm maturation, increasing horizontal shear expands the surface area of the updraft exposed to a moderately dry environment. Indeed, during the rapid development of the updraft (0.6 to 0.9 h), the volume-average updraft buoyancy (Fig. 4.12) decreases with increasing horizontal shear. However, a true confirmation of entrainment effects would require careful consideration of parcel trajectories in and around the cloud.

It was mentioned just before that, in the early evolution of the heat bubble, downward motion is restricted along the transverse edges of the plume in horizontal shear. Figure 4.13a shows the vertical motion, in a frame of reference oriented along the plume's longitudinal axis, near the top of the warm bubble (z = 1.25 km) at 0.6 h in v00h6 and verifies the banded nature of horizontally sheared plumes. Figures 4.13b,c show the perturbation relative vorticity ζ', representing the difference between the total vertical vorticity and the background shear vorticity, at z = 1.25 km and z = 0.08 km. Perturbation wind vectors (i.e., wind not associated with the background flow), superimposed upon the vorticity fields in Fig. 4.13b,c, further illustrate the transverse nature of the plume's overturning circulation. Near the surface, positive ζ' dominates in an elliptical pattern. At the top of the plume, a quadrupole pattern of alternately signed vorticity exists in association with the perturbation wind field.

A vorticity budget suggests an origin of the transverse circulation. Near the

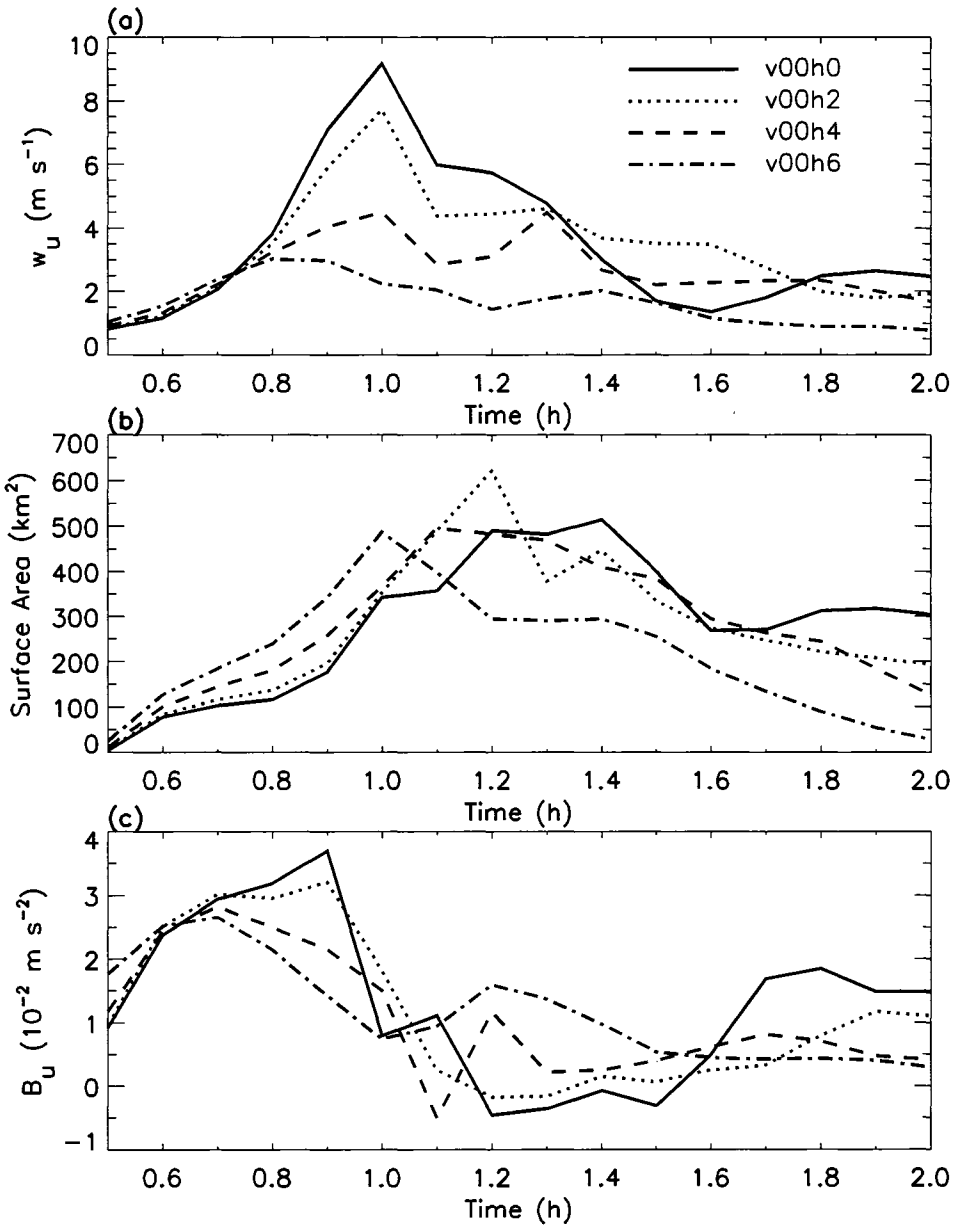

Figure 4.12: Updraft (a) volume-average vertical motion (m s^{-1}), (b) surface area (km^2), and (c) volume-average buoyancy (m s^{-2}) for v00h0, v00h2, v00h4, and v00h6.

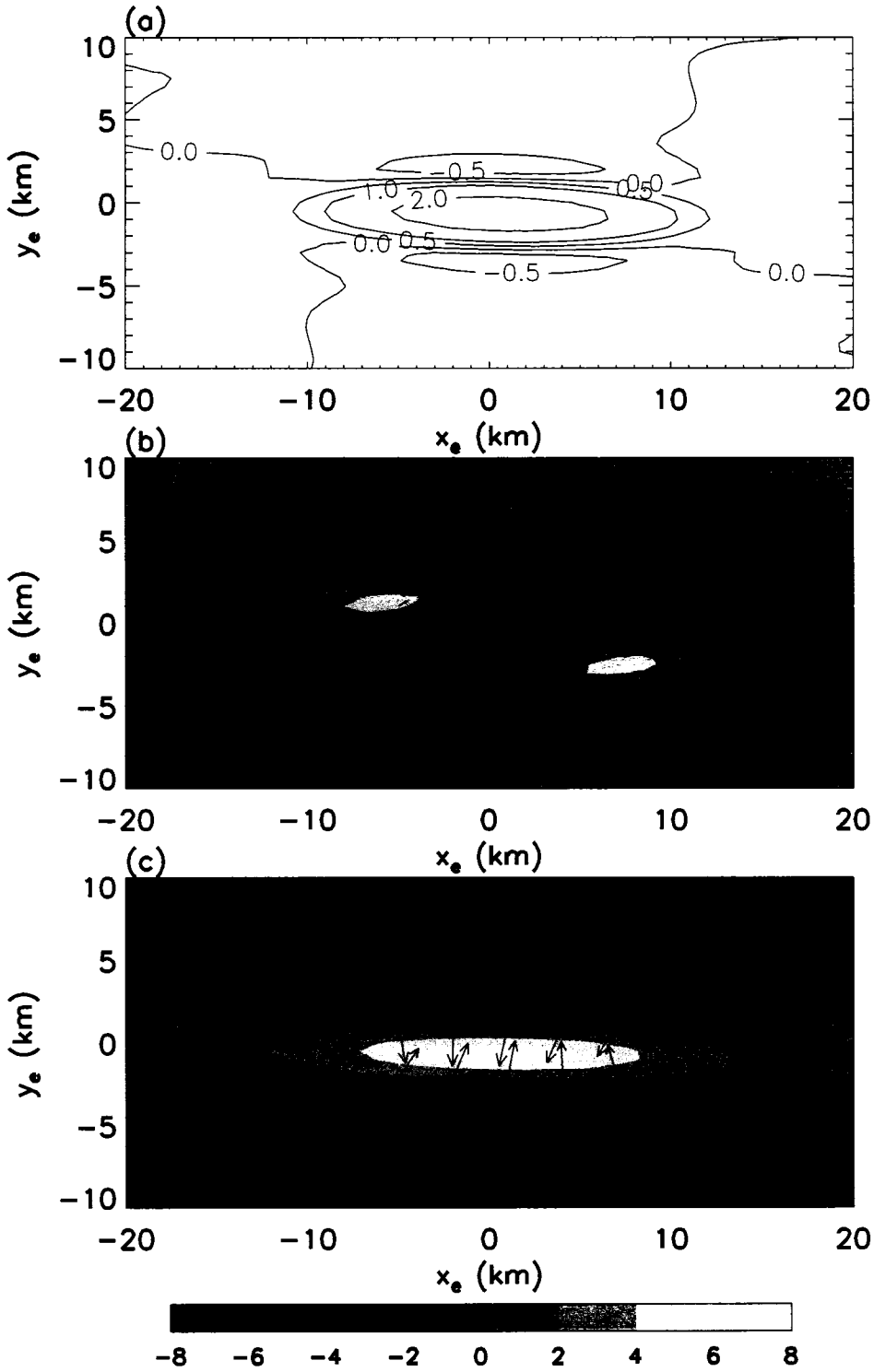

Figure 4.13: (a) Vertical motion (m s^{-1}) at 0.6 h and $z = 1.25$ km in a rotated frame of reference for experiment v00h6; Perturbation relative vorticity (10^{-4} s^{-1}) and associated horizontal wind vectors at 0.6 h and (b) $z = 1.25$ km and (c) $z = 0.08$ km. The maximum vector length represents a wind speed of 3 m s^{-1}.

surface, a vorticity budget shows the relevant process leading to the ellipse of positive ζ' is the convergence of background vorticity, ζ_a. Such vorticity convergence occurs in all of our experiments. However, near the top of a horizontally sheared plume, the tilting of positive vorticity leads to the quadrupole of vorticity. In our rotated grid, we establish a new coordinate system (x_e, y_e) with rotated wind components (u_e, v_e), where x_e (y_e) is oriented along the longitudinal (transverse) axis of the plume. Consequently, the tilting term in the vorticity equation can be expressed in the rotated coordinate system as

$$\left.\frac{\partial \zeta'}{\partial t}\right|_{\text{tilt}} = \frac{\partial w}{\partial y_e}\frac{\partial u_e}{\partial z} - \frac{\partial w}{\partial x_e}\frac{\partial v_e}{\partial z}. \tag{4.19}$$

Figure 4.14 shows each derivative and the complete products within the tilting term (4.19) for experiment v00h6 at 0.6 h and $z = 1.25$ km. Figures 4.14e,f show that vorticity tilting is dominated by the term $(\partial w/\partial y_e)(\partial u_e/\partial z)$. In other words, although the magnitude of vertical shear of the horizontal perturbation wind is comparable in all directions, stronger gradients of w form in the transverse direction. Moreover, because of the overturning circulation, there is a positive feedback in the growth of $(\partial w/\partial y_e)$ because of transverse downward motion and its subsequent contribution to the transverse w gradient. At the top of the plume around 0.6 h, the dynamic pressure perturbation gradient force is downward along the transverse flanks of this plume. However, this acceleration is about one quarter of the magnitude of downward accelerations due to buoyant contributions in the same region.

Later on, as deep convective clouds form, the vorticity evolution becomes increasingly complex. Figure 4.15 shows important information for case v00h4 related to the time evolution of the low-level updraft ($z = 1.25$ km). The left-hand column contains vertical motion and perturbation vertical vorticity ζ'. As before, the perturbation vertical vorticity is the component of vertical vorticity not associated with the background horizontal shear. At early times, the updraft contains positive vertical vorticity originating from the stretching of low-level, background vorticity. The

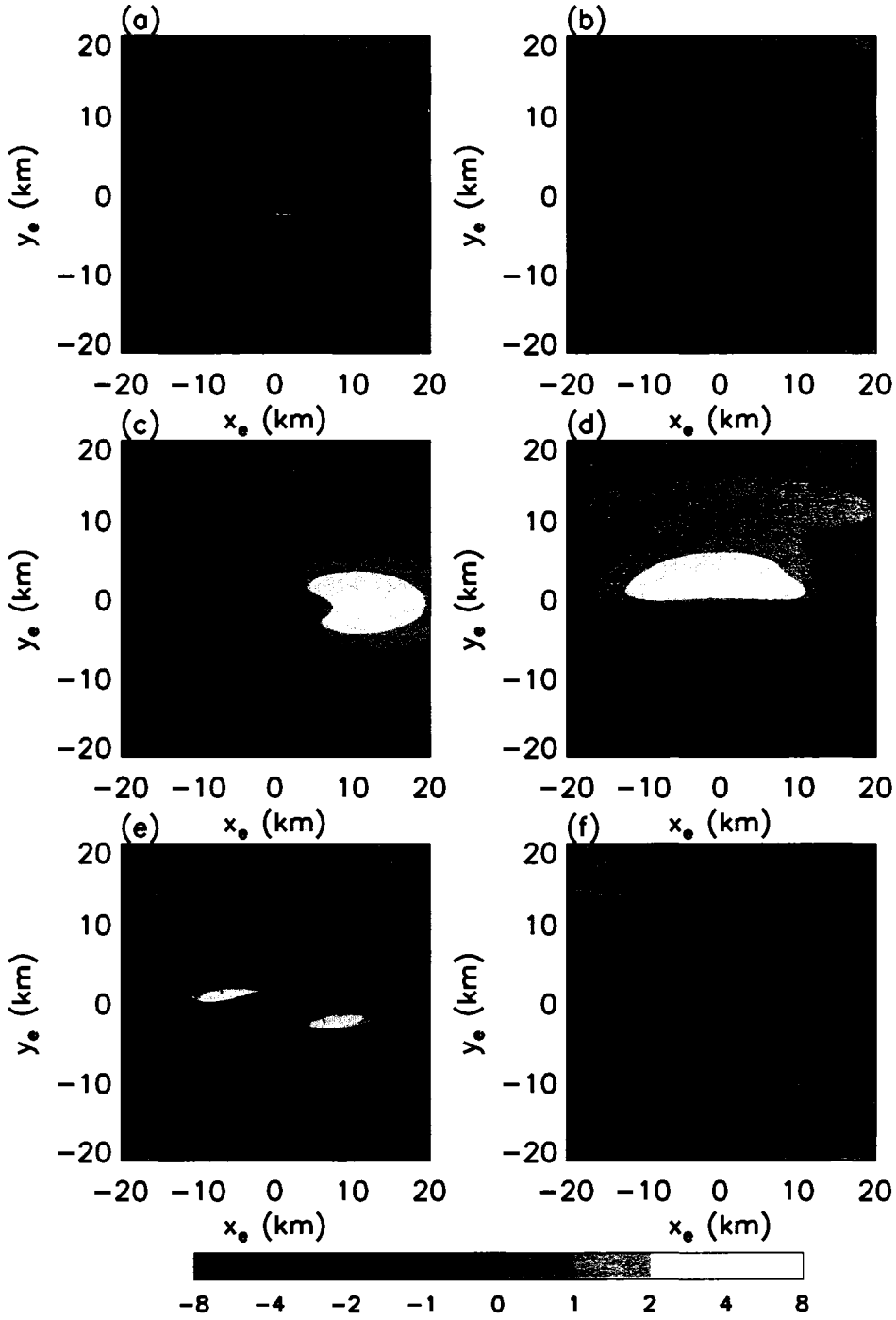

Figure 4.14: Components of the tilting term (4.19), (a) $\partial w/\partial y_r \times 10^3$, (b) $\partial w/\partial x_r$, (c) $\partial u_r/\partial z$, and (d) $\partial v_r/\partial z$ (10^{-3} s^{-1}), in experiment v00h6 at 0.6 h and z = 1.25 km; the corresponding, complete terms of (4.19), (e) $(\partial w/\partial y_r)(\partial u_r/\partial z)$, and (f)$-(\partial w/\partial x_r)(\partial v_r/\partial z)$ (10^{-6} s^{-2}). In (e) and (f), the total tilting term is contoured.

downdrafts advect the upper-level vorticity pattern described in Fig. 4.13b downward along the transverse edges of the updraft. As the experiment progresses in time, these alternating vorticity patterns persist along the flanks of the dispersing, longitudinal updraft cells. These vorticity quadrupoles are consistent with increased longitudinal flow into the updrafts and transversal flow out of the updraft at lower levels of this plume. In the wake of these updrafts, a long filament of positive vorticity (and positive PV) is left behind. This vorticity exceeds 1×10^{-3} s^{-1}. In v00h6, because of weaker updrafts, the vorticity wake decreases by half its magnitude found in v00h4 and the enhanced vorticity achieves lower maximum altitudes in v00h6 (figure not shown).

The middle and right-hand columns of Fig. 4.15 contain the important dynamic pressure perturbation gradient and the sum of the buoyancy and buoyant pressure perturbation gradient terms (buoyant forcing), respectively, in the w acceleration equation (4.5). Horizontal and vertical advection terms are not shown here because they provide expected results. Namely, at $z = 1.25$ km, upward advection of w contributes to a decrease in local w and horizontal background flow advects the updraft(s). The dynamic pressure perturbation gradient, driven by horizontal vorticity associated with the transverse overturning circulation, provides some upward acceleration just within the low-level flanks of the updraft at 0.7 h, but this acceleration becomes relatively insignificant at this particular vertical level afterward. Buoyant forcing is most prominent along the longitudinal edges of the low-level cold pool and corresponds well with the locations of the low-level updrafts.

Along with the updrafts, the cold pool resulting from precipitating downdrafts is stretched by the horizontal shearing deformation. As we identified in v00h0, low-level convergence by the cold pool is crucial in sustaining and reforming convective cells. In the cases of horizontal shear, enhanced low-level convergence surrounds the entire coldpool. Yet, as described earlier, transverse subsidence suppresses convec-

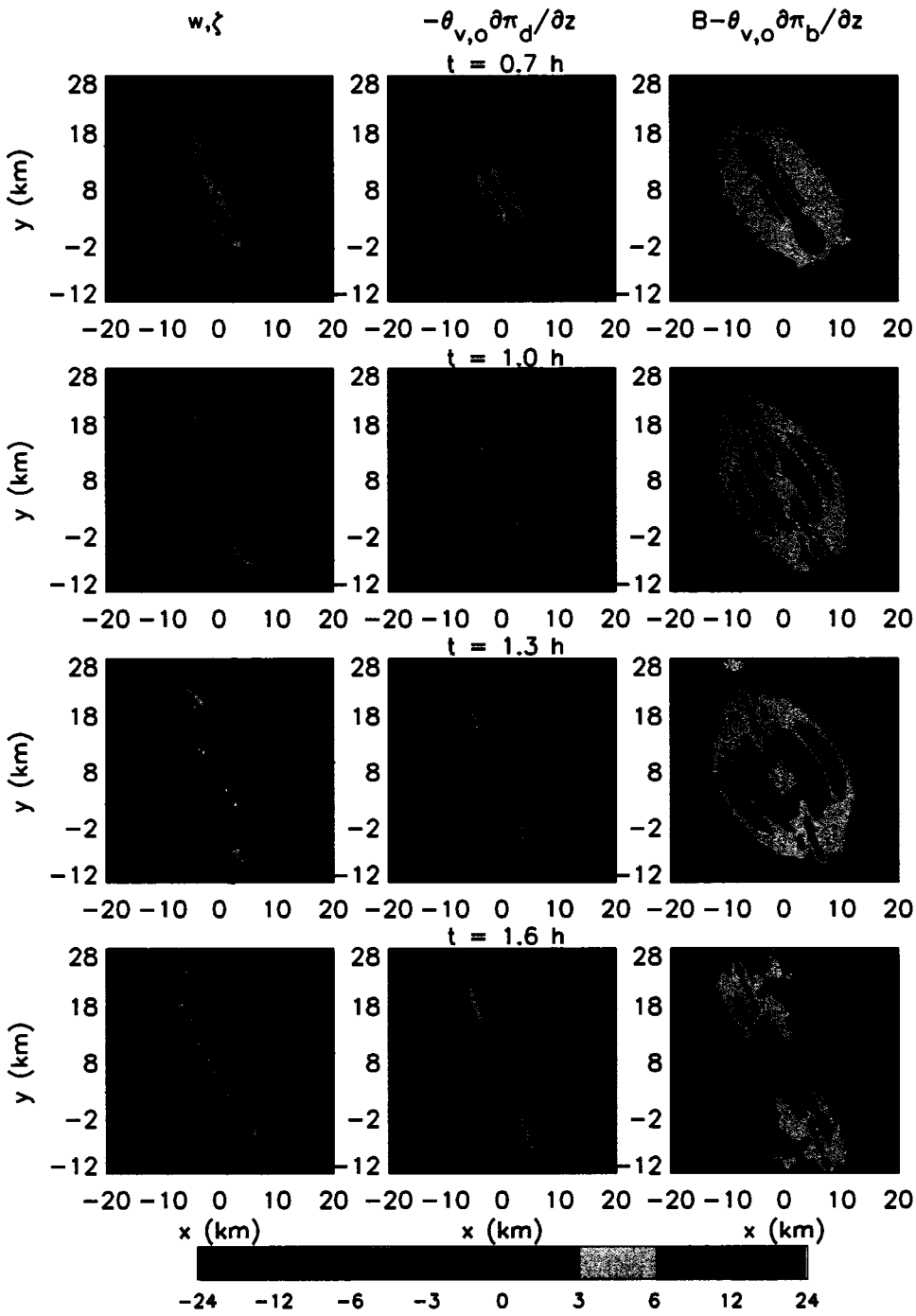

Figure 4.15: Vertical velocity fields (m s^{-1}; contoured) and perturbation vertical vorticity (10^{-4} s^{-1}; shaded) (left-hand column; Dynamic perturbation pressure gradient acceleration, $-\theta_{vo}$ $(\partial\pi'_d/\partial z)$ (10^{-3} m s^{-2}; shaded; middle column); the sum of B and the buoyant perturbation pressure gradient acceleration, $B-\theta_{vo}$ $\partial\pi'_b/\partial z$ (10^{-3} m s^{-2}; right-hand column) for experiment v00h4 at 0.7, 1.0, 1.3, and 1.6 h.

tive development on the transverse flanks. Consequently, large flanks of low-level divergence restrict the convergence region adjacent to the cold pool on these edges. Subsidence associated with banded gravity waves forming on the transverse flanks of the banded convection constructively adds to the suppression of convection in the transverse directions. CIN is substantially enhanced by amounts exceeding 25 J kg^{-1} in these gravity waves and CAPE is slightly depressed (figures not shown). The opposite is true along the longitudinal ends of the cold pool, where buoyancy is enhanced and CIN is eroded to about zero.

Another interesting property of the horizontal shear experiments also concerns the convectively-generated cold pool's impact on convection. As seen earlier in Fig. 4.11, the dispersing updrafts appear to lean over the cold pool toward one another. While low-level vertical shear is, in fact, generated by the cold pool, the horizontal shear also acts like a pseudo-vertical shear in this situation. In other words, new updrafts are forced at the longitudinal ends of the cold pool. However, as expected from 2D theory (e.g., Lapeyre et al., 1999), the elongated convective band is not oriented parallel to the horizontal background flow. Therefore, recently generated low-level updrafts are advected at different speeds relative to upper portions of the same updraft as a result of horizontal shear.

Following trends in covective vigor, the resulting cold pool strength decreases monotonically with increasing horizontal shear (Fig. 4.16a). Experiment v00h6 produces a particularly weak cold pool and this is attributable to the weaker convection. Figure 4.16b shows that the θ_e deficit grows larger with horizontal shear. The time rates of increase in the θ_e deficit are similar for each experiment after 1 h and therefore suggest much of the difference comes from the greater initial moisture convergence under stronger developing plumes in weaker shear situations. Hence, this cold pool effect constructively reinforces the suppressed nature of convection in stronger horizontal shear.

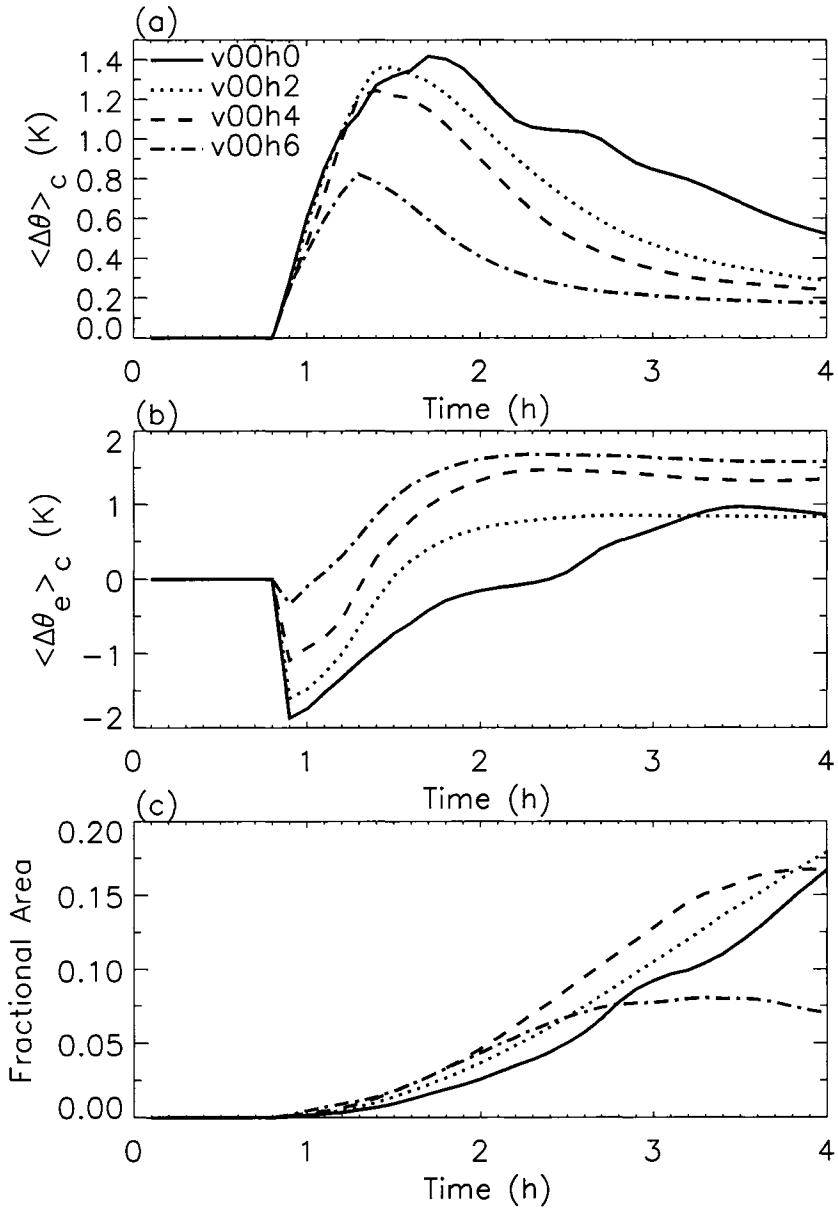

Figure 4.16: (a) Cold pool strength as defined in (4.12) for experiments v00h0, v00h2, v00h4, and v00h6, (b) corresponding θ_e deficits, and (c) fraction of the domain covered by the cold pool.

4.3.4 Vertical and horizontal shear

We now consider experiments containing both vertical and horizontal shears of the "tangential" wind. This configuration is a step closer toward a realistic kinematic environment within a TC. As noted earlier, shear profiles in real TCs are more sophisticated due to significant radial wind components in the vertical shear profile. Overall, the composite attributes of these experiments combine many responses from our previous experiments and the complexity of convective behavior grows accordingly. In order to survey the most interesting differences from the previously described experiments, we concentrate on hybrid experiments possessing the greatest vertical shear [i.e., v_z =(20 m s^{-1})(15 km)$^{-1}$].

Figure 4.17 shows the evolution of storms for experiments v20h2, v20h4, and v20h6 over a period of 40 min. Early on, the low-level warm bubble is stretched by the horizontal shear. Once a deep, moist convective cloud forms with intense vertical velocities, updrafts tilt with the vertical shear in each case. Also, in agreement with the horizontal shear experiments, the vigor of convection decreases with increasing horizontal shear, with suppressed $h_{\max}$, dampened vertical motions (i.e., $w_{\max}$ and $w_{\min}$), and decreased τ_l (Table 4.1). Once again, horizontal shear of $v_x = -6 \times 10^{-4}$ s^{-1} is strong enough to suppress significant convection. However, in comparing the results of our experiments in hybrid shears to those without vertical shear, a slightly stronger southern updraft emerges in the banded convective structures. Because the axis of convection never achieves an orientation perpendicular to the horizontal shear, the tilting of the updraft and its precipitation helps keep the updrafts ventilated from precipitation, although this situation favors the southern cells. It should be pointed out that storm splitting occurs in all hybrid configurations. Since a fundamentally different splitting mechanism was identified for each type of shear, it is necessary to discern which of these two mechanisms act in cases for different combinations of vertical and horizontal shear.

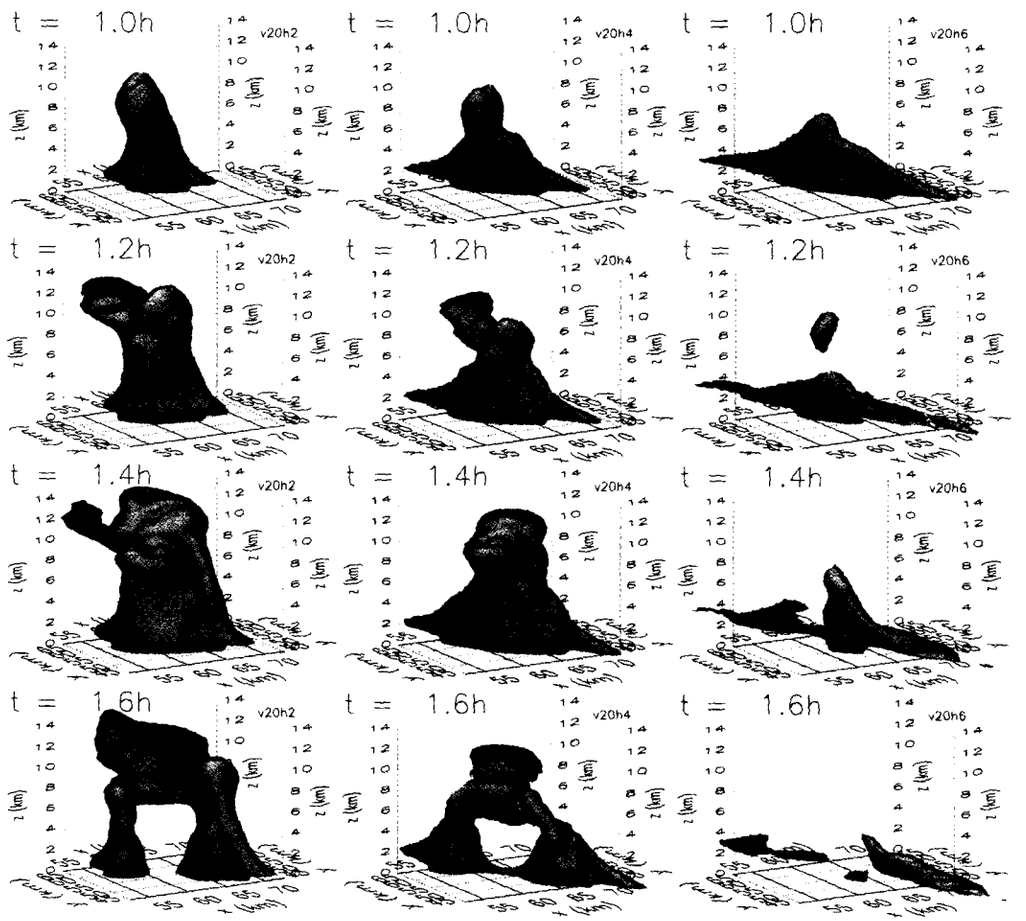

Figure 4.17: Total cloud condensate ($q_{\text{cond}} \geq 0.5$ g kg^{-1}) for experiments v20h2 (left column), v20h4 (middle column), and v20h6 (right column).

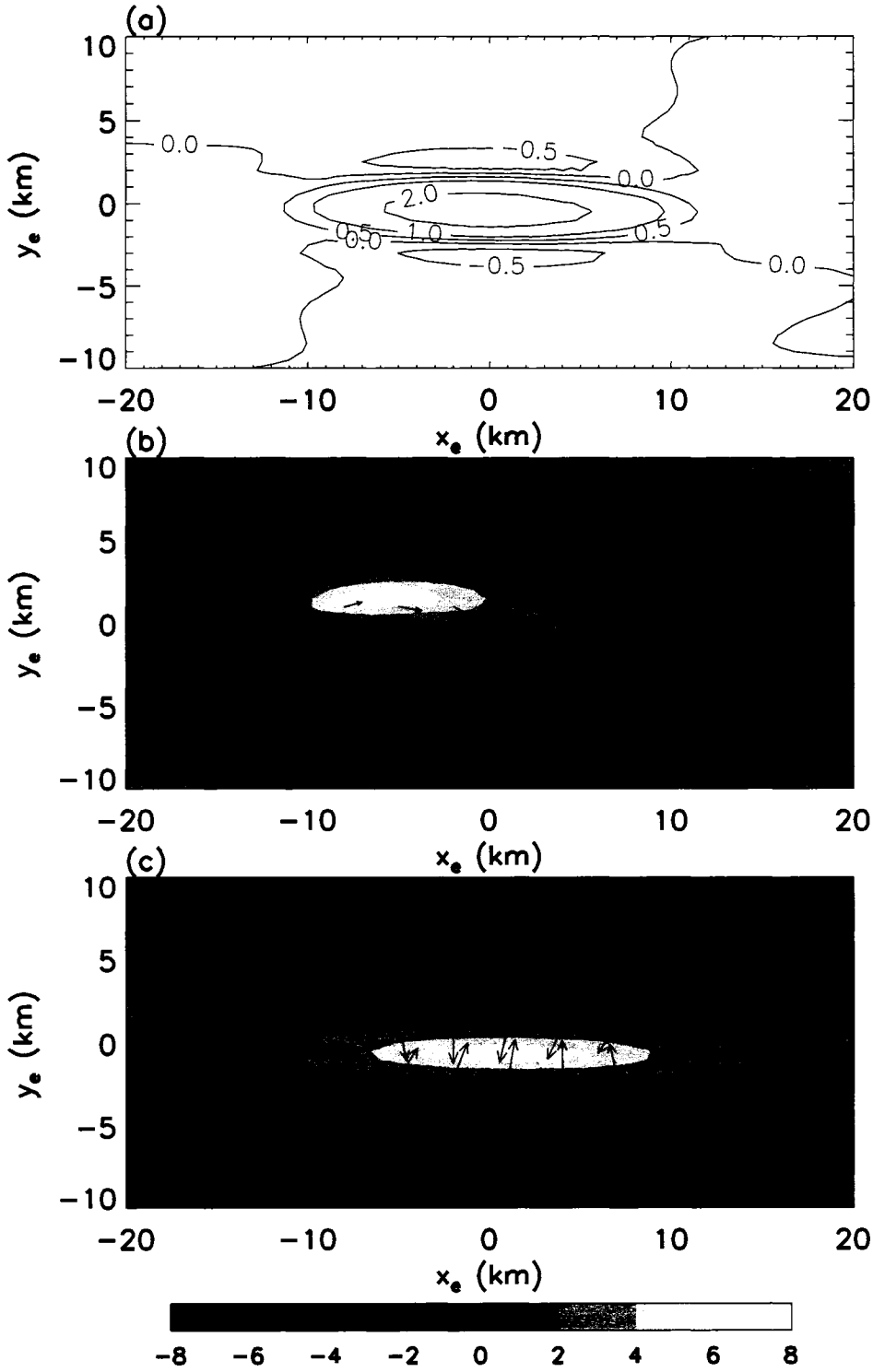

Figure 4.18: (a) Vertical motion (m s^{-1}) at 0.6 h and z = 1.25 km in a rotated frame of reference for experiment v00h6; Perturbation relative vorticity (10^{-4} s^{-1}) and associated horizontal wind vectors at 0.6 h and (b) z = 1.25 km and (c) z = 0.08 km. The maximum vector length represents a wind speed of 3 m s^{-1}.

Figure 4.18 displays vertical motion and perturbation vertical vorticity fields (i.e., background shear vorticity is subtrated off), in a rotated reference frame, at 0.6 h in experiment v20h6. Figure 4.18a shows the w field near the top of the plume ($z = 1.25$ km), which appears very similar to the w field in experiment v00h6 (Fig. 4.13a) except there is a slight bias toward stronger downward motion along the upper (downshear) flank of the plume. At $z = 1.25$ km, the vorticity pattern differs from v00h6 as its longitudinal anti-symmetry disappears in v20h6. In this case, cyclonic (anticyclonic) vorticity dominates on the upper (lower) flank of the plume. A vorticity budget (figure not shown) confirms that this pattern results from a combination of vortex tilting associated with the vertical shear of the ambient wind, as in v20h0, and the nonlinear vortex tilting deduced in v00h6. At low-levels, strong convergence dominates in concentrating positive perturbation vorticity underneath the plume. A very slight bias is introduced due to some projection of the tilting of the vertical shear. These results suggest two important features. It shows that horizontal shear, even in the presence of vertical shear, continues to play an important role in forming banded plumes. Second, the tilting of vorticity associated with the vertical shear sets the stage for an anticyclonic and cyclonic pair of storms, which we will now elaborate upon.

We first focus our attention on experiment v20h2. As seen in the 3D renderings of total cloud condensate above, this storm splits. The left-hand column of Fig. 4.19 shows w and perturbation vertical vorticity ζ' at $z = 1.25$ km. Within the updraft, a couplet of oppositely signed vorticity appears by 0.7 h. These patterns originate from vortex tilting. Around the edges of the updraft, transverse subsidence is present. Within these downdrafts, there are alternating patterns in the vorticity field, which result from the downward advection of the upper-level vorticity quadrupole. The middle and right-hand columns of Fig. 4.19 contain the dynamic perturbation pressure gradient force and the sum of the buoyancy and buoyant perturbation pressure gra-

dients, respectively. Similar to v20h0, dynamic pressure perturbation gradients force lifting on the flanks of the updraft. Buoyant contributions are larger in magnitude in this situation, with maxima of upward accleration located near the longitudinal ends of the updraft. By 1.0 h, the updraft is more filamented, and a negatively buoyant precipitating downdraft occurs downshear of the updraft. The left-hand filamented updraft is predominantly anticyclonic and the right-hand updraft is cyclonic. This situation behaves similarly to a supercell split. The buoyant forcing appears to be a significant component of the splitting and the dynamic pressure perturbations appear to be acting constructively toward a cloud split, where dynamic pressure perturbations pull the cyclonic vortex rightward and the anticylonic vortex leftward. We note the transverse gravity wave that appears in the buoyancy field in the right-hand column at 1.0 h. As time progresses, the updrafts completely split. The anticyclonic updraft is particularly filamented while the cyclonic updraft remains more compact. Buoyant forcing from outflow boundaries are evident by 1.6 h as the updraft begins to succomb to the cold pool.

Many of the same updraft features depicted in v20h2 are present in v20h4 (c.f., Figs. 4.19,4.20). Updrafts split in this case and each split contains the same signed vorticity as before. In this case of enhanced horizontal shear, the w and ζ' fields experience increased filamentation over v20h2. In contrast with the single positive vorticity filament left behind in v00h4, nearly parallel anticylonic and cyclonic vorticity filaments are left behind in the wake of the convective cells. Also, as in v20h2, dynamic pressure perturbations occur on the transverse flanks of convection, but the storm splitting is even more dominated by buoyant forcing in comparison to v20h2. The buoyant accelerations are particularly enhanced at the longitudinal ends of the convective band and are located at the edge of the cold pool where there is enhanced low-level convergence, although areas of convergence within the band promote buoyant forcing throughout the extent of the band.

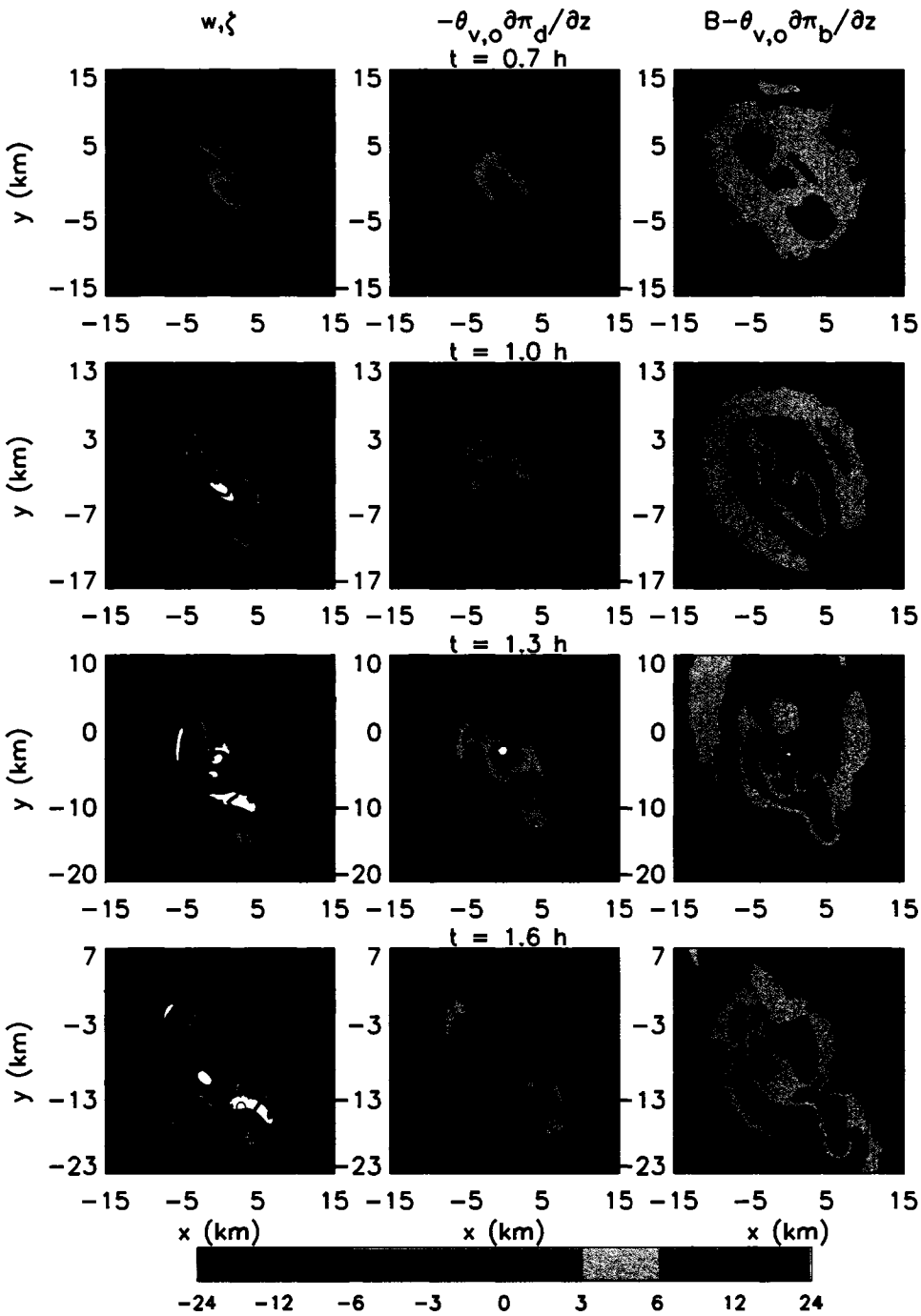

Figure 4.19: Vertical velocity fields (m s^{-1}; contoured) and perturbation vertical vorticity (10^{-4} s^{-1}; shaded) (left-hand column; Dynamic perturbation pressure gradient acceleration, $-\theta_{vo}$ $(\partial\pi'_d/\partial z)$ (10^{-3} m s^{-2}; shaded; middle column); the sum of B and the buoyant perturbation pressure gradient acceleration, $B-\theta_{vo}$ $\partial\pi'_b/\partial z$ (10^{-3} m s^{-2}; right-hand column) for experiment v20h2 at 0.7, 1.0, 1.3, and 1.6 h.

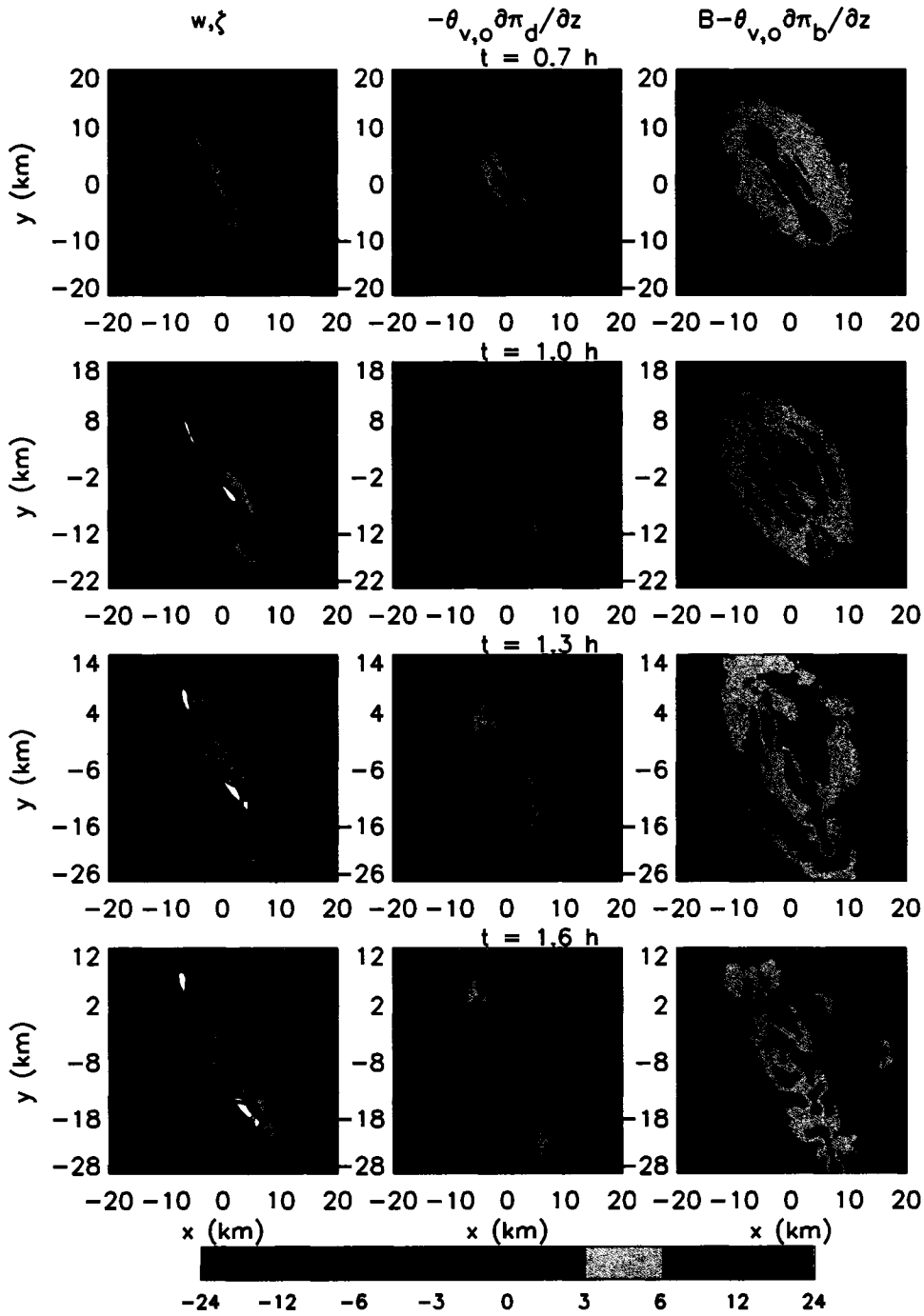

Figure 4.20: Vertical velocity fields (m s^{-1}; contoured) and perturbation vertical vorticity (10^{-4} s^{-1}; shaded) (left-hand column; Dynamic perturbation pressure gradient acceleration, $-\theta_{vo}$ $(\partial\pi'_d/\partial z)$ (10^{-3} m s^{-2}; shaded; middle column); the sum of B and the buoyant perturbation pressure gradient acceleration, $B-\theta_{vo}$ $\partial\pi'_b/\partial z$ (10^{-3} m s^{-2}; right-hand column) for experiment v20h4 at 0.7, 1.0, 1.3, and 1.6 h.

4.4 Thermodynamic sensitivities

The composite sounding we chose to initialize the control experiments contains relatively dry air aloft and also yields modest low-level instability. Given the amount of variability typically documented in thermodynamic conditions outside of a TC's primary eyewall, the background temperature and moisture profiles of our control experiments establish neither the generality of the sheared convective behavior nor the practical threshold for adverse filamentation. To explore the general validity of our control experiments, two additional sets of experiments are carried out to uncover the sensitivity of sheared convection to background moisture and convective instability. First, a set of "unstable" experiments are performed with slight modifications to the control sounding's low-level instability, and second, a set of "moist" experiments elucidates the effect of the control experiment's dry-air on key shear experiments by increasing the moisture in the control sounding.

4.4.1 Unstable experiments

The first series of sensitivity experiments increases the instability in the 900 to 700 hPa layer by cooling the ambient temperatures in that layer by no more than 1°C (cf., Fig. 4.21a and Fig. 4.3). This subtle alteration to the ambient lapse rate yields about 50 J kg^{-1} more undilute, surface-based CAPE than in our control sounding. Large sensitivities in convective initiation and strength to slight changes in boundary layer θ have been noted in the past (e.g., Brooks et al., 1993; Crook, 1996). In addition, McCaul and Weisman (2001) demonstrated that supercell morphology, particularly in lower CAPE situations, strongly depends on the vertical distribution of buoyancy. Hence, we expect that our sheared convection will be highly sensitive to cooling in the 900–700 hPa layer. In the following sensitivity experiments, four simulations adopt the wind profiles of v00h0, v20h0, v00h6, and v20h6 in the more

unstable environment. The remaining shear cases are not simulated due to practical computing limitations and redundant results.

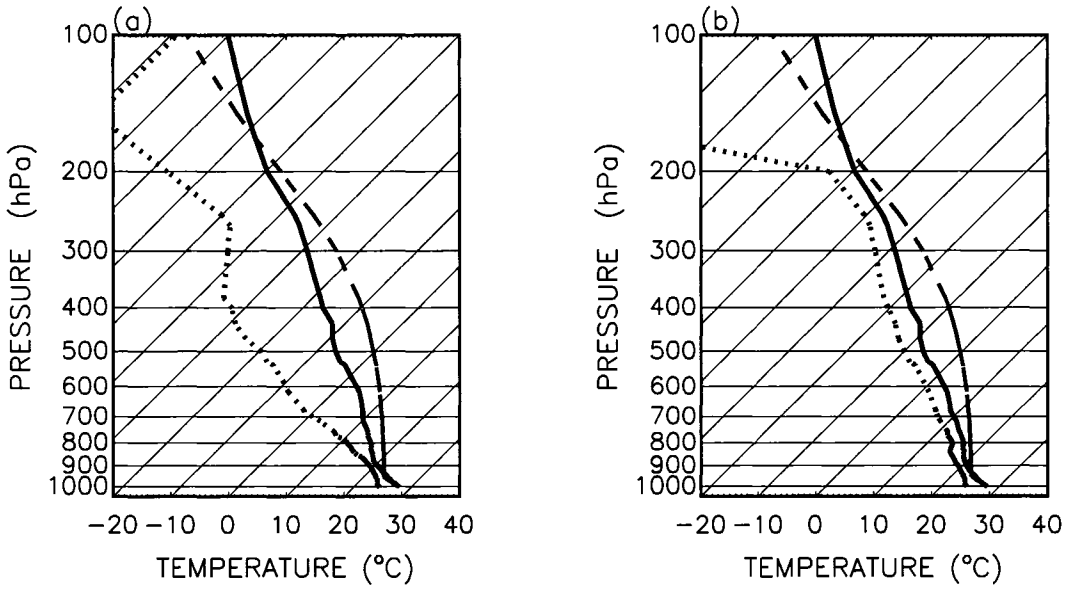

Figure 4.21: Same as in Fig. 4.3, but for the (a) "unstable" and (b) "moist" experiments.

As anticipated, convection in the unstable experiments is more vigorous than in our control experiments (Table 4.2; Fig. 4.22). The overall convective dynamics of the unstable experiments are not qualitatively different from our control experiments. The two left-hand columns in Fig. 4.22 illustrate snapshots of the total condensate for experiments v00h6 and v20h6 at select points in time during the mature phase of convection. As in cases of horizontal shear in the control experiments, the storms undergo splitting after initiation and move off in opposite directions rather quickly in time. Deep, moist convection initiates about 5 min earlier than in the control experiments. The updrafts extend further in height for all our unstable experiments. Experiments without horizontal shear (i.e., v00h0 and v20h0) reach about 1 km higher into the stratosphere in the unstable situation. However, $h_{\max}$ for the horizontally sheared situations (i.e., v00h6 and v20h6) increases by about 2.5 km. The strength of vertical velocities is also increased for all cases. While the storm lifetime, τ_l, is

	τ_l	h_{max}	w_{max}	w_{min}
v00h0	2.1	15.9	41.3	-16.6
v20h0	1.1	15.4	40.1	-16.2
v00h6	1.0	12.4	25.6	-6.6
v20h6	1.5	11.9	25.6	-9.6

Table 4.2: Convective lifetimes, τ_l (h), maximum height of convection, h_{max} (km), maximum vertical speed, w_{max} (m s^{-1}), and minimum vertical speed, w_{min} (m s^{-1}) for the unstable experiments.

increased by about 12 min in v20h0, τ_l substantially increases in situations with horizontal shear, where τ_l increases from 0.2 h to 1.0 h in v00h6 and from 0.5 to 1.5 h in v20h6 (Table 4.2). Hence, while the control experiments offer a practical threshold of "rapid filamentation", the unstable experiments show that a seemingly modest augmentation of the low-level potential buoyancy counteracts detrimental impacts of horizontal shear on deep, convective clouds.

Figure 4.23 presents integrated statistics for the changes in updraft strength between the unstable and control experiments. The difference in volume-average updraft vertical velocity is presented in Fig. 4.23a. Largely because convection developed 5 min earlier in the unstable experiments, the vertical velocity differences in v00h0 and v20h0 are most pronounced before 1 h. The largest change in w occurs for situations including horizontal shear since both v00h6 and v20h6 now form deep, convective circulations with consistently elevated updraft speeds. The amount of updraft surface area is also enhanced for all cases in the unstable environment. Somewhat more surprising is the relatively small differences in buoyancy between the two set of experiments (Fig. 4.23c). Updraft buoyancy is substantially smaller in v00h0 and v20h0 prior to 1.2 h.

Like the updrafts, cold pools increase in strength for all our unstable experiments. These changes are most distinguished in v00h6, v20h0, and v20h6 (Fig. 4.24a).

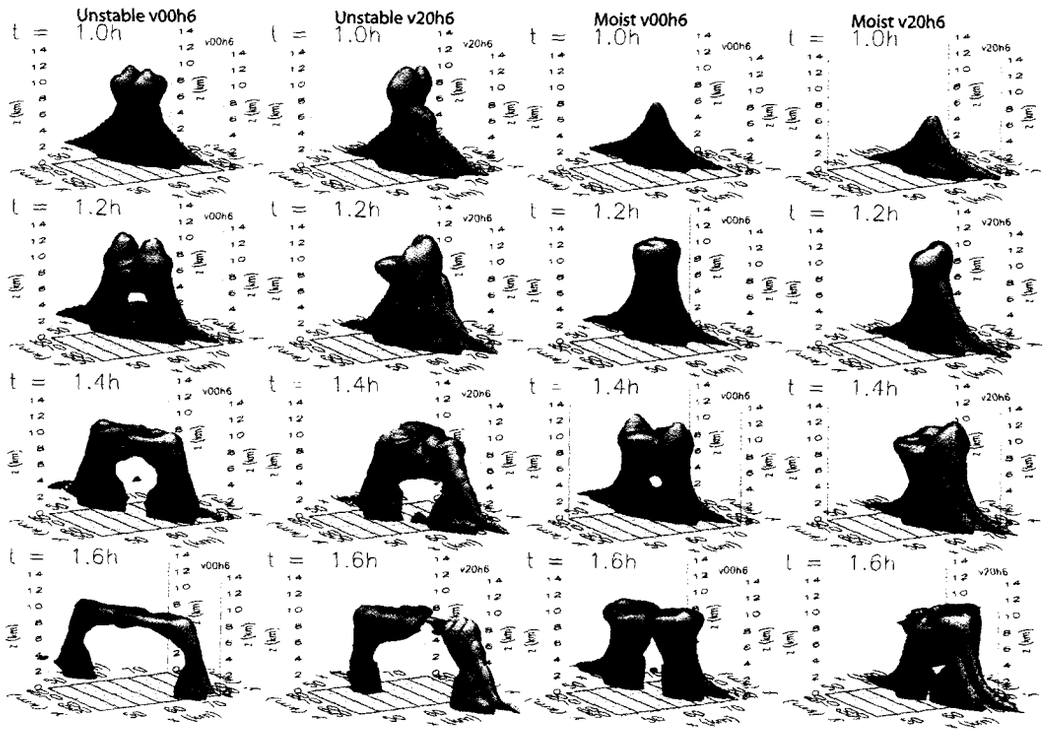

Figure 4.22: Total cloud condensate ($q_{\text{cond}} \geq 0.5$ g kg^{-1}) for v00h6 and v20h6 in the unstable experiments (two left hand columns, respectively) and the moist experiments (two right hand columns, respectively).

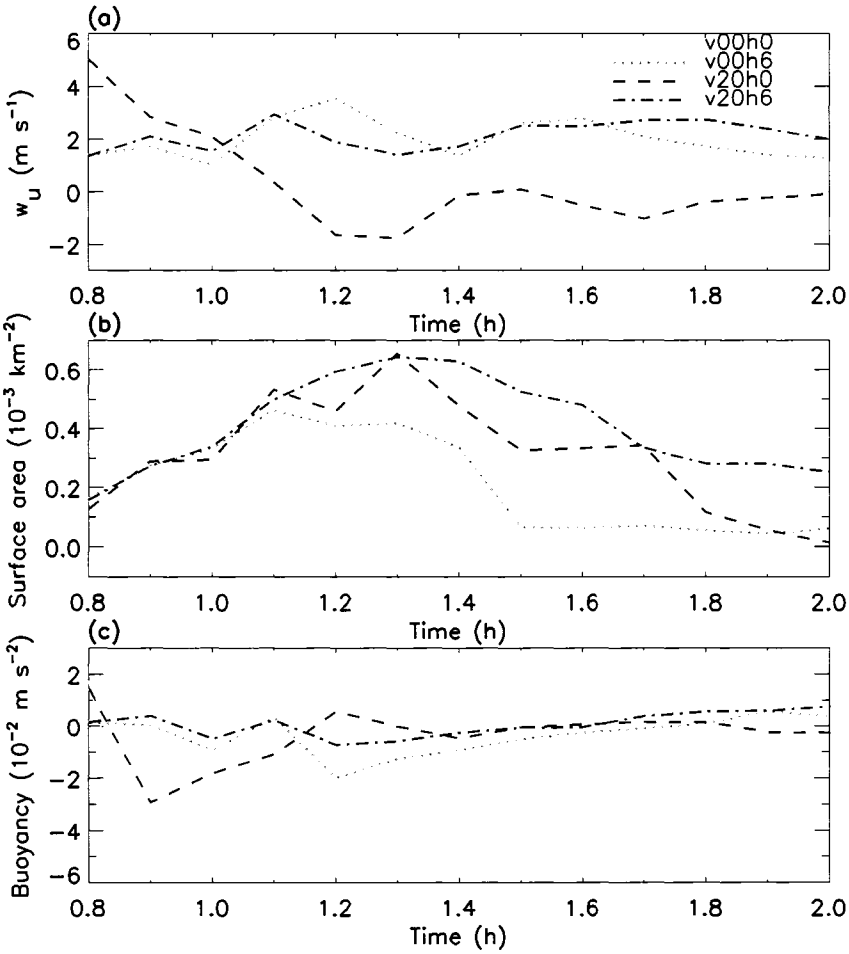

Figure 4.23: Differences between the unstable and control experiments' (a) volume-average updraft speed (m s^{-1}), (b) surface area of the updraft (10^{-3} km^{-2}), and (c) volume-average updraft buoyancy (10^{-2} m^{-1} s^{-2}).

In these cases, $\langle \Delta\theta \rangle_c$ (Fig. 4.24a) increases by 0.8–0.9°C. The cold pool produced by horizontally sheared convection is now comparable in strength to v00h0 with $\langle \Delta\theta \rangle_c$ values around 1.6–1.7°C. Similarly, θ_e deficits are stronger in these coldpools (Fig. 4.24b). For each experiment, the maximum value of $\langle \Delta\theta_e \rangle_c$ roughly doubles, where the deficit in the unstable v20h0 is 7 K greater than in the control experiment. Similar to some cold pools observed in rainbands (e.g., Barnes et al., 1983), v20h0 now produces a substantial θ_e deficit of 10.5 K. In all shear configurations, the fractional area of the domain covered by the cold pool increases significantly with a more unstable environment (Fig. 4.24c). In v20h6, the cold pool boundary traverses off of the domain by 3 h into the simulation. This effect creates a spurious decline in the cold pool fractional area after 3 h (Fig. 4.24c).

One hypothesis that most likely explains the updraft characteristics described earlier is that a more active cold pool in the unstable experiments forces convection over a greater proportion of the domain, but this cold pool is also more intrusive to the updrafts. This intense cold pool forces convection over a broader area in an environment that is more conducive to enhanced initiation. In addition, the drier cold pool spreads out more rapidly in our unstable experiments and, therefore, may lead to the observed decreased updraft buoyancy (Fig. 4.23c). Model snapshots of the cold pool and updraft show the cold pool more aggressively spreads beneath convection in our unstable experiment. In v20h0, the convective updraft in the unstable (control) environment is completely surrounded by the cold pool by 1.4 h (1.7 h). The updraft begins to diminish shortly after the passage of the cold pool. In association with these larger and stronger cold pools, plots of surface-based CAPE and CIN (figures not shown) show CAPE is depleted over a broader region and CIN is accordingly increased substantially over the same region.

Volume-average downdraft statistics and a budget of low-level water vapor transport help explain the increased strength of the low-level cold pool (Fig. 4.25).

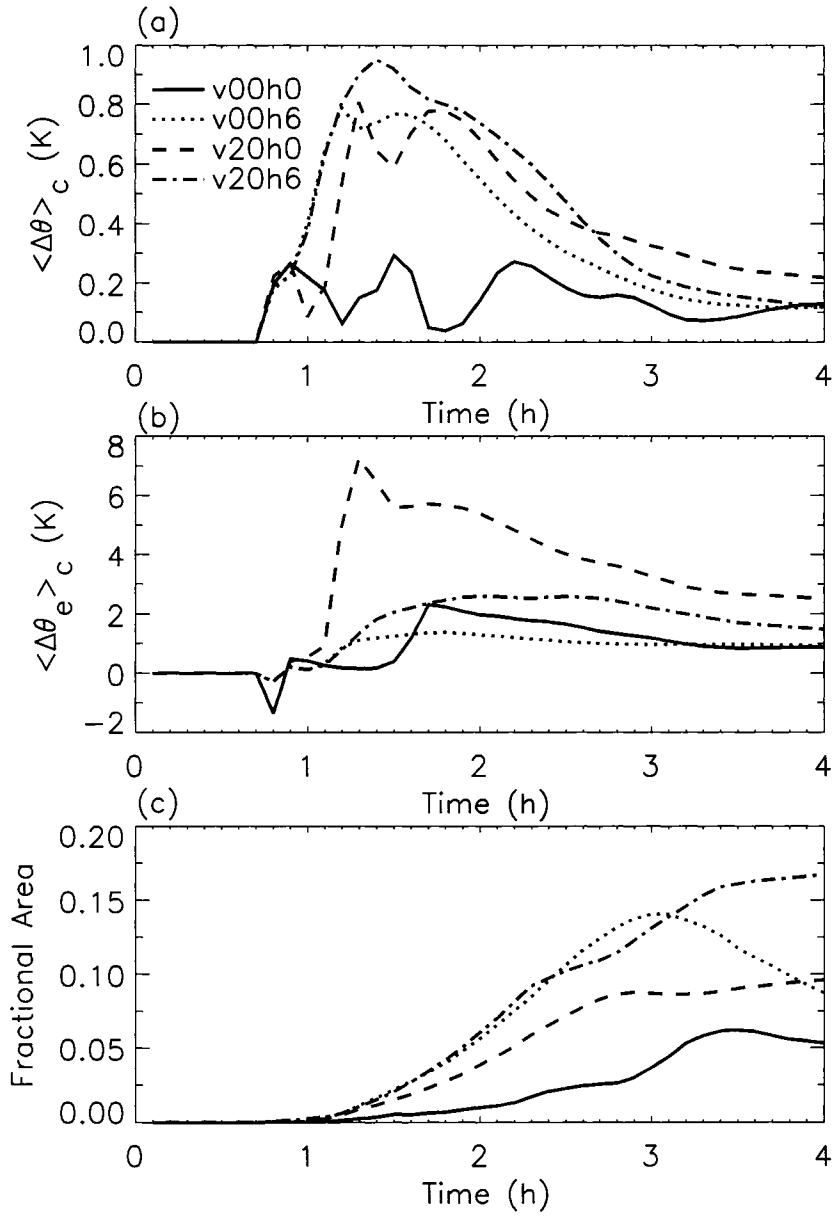

Figure 4.24: (a) The difference in cold pool strengths between the unstable and control experiments for cases v00h0, v00h6, v20h0, and v20h6, (b) corresponding θ_e deficit differences, and (c) difference in fraction of the domain covered by a cold pool.

Figure 4.25a shows the differences in volume-average downdraft strength between the unstable and control experiments. Overall, our unstable experiments produce enhanced downward motion between 0 and -1 m s^{-1}. The early minima in these differences are due to the earlier deep, convective cloud initiation in the unstable experiments. From Fig. 4.25b, the overall size of downdrafts in the unstable downdrafts is considerably larger in the more unstable situation. Increased transport of water vapor out of the cold pool is associated with enhanced downdrafts (Fig. 4.25). This factor is pronounced in experiment v20h0. The enhanced water vapor transport helps explain increased θ_e deficits in the cold pool. Figure 4.25d shows the difference in the average downward component of water vapor transport for each experiment. For the most part, greater downward advection of drier air is apparent in the unstable experiments, with the exception of v20h0 after 1.4 h.

4.4.2 Moist experiments

To further understand the role of dry air on the convective morphology observed in the previous experiments, another series of experiments adopt a very moist troposphere. The sensitivity of convection to tropospheric moisture has been noted in past literature (e.g., Gilmore and Wicker, 1998; Wilhelmson and Wicker, 2001; Derbyshire et al., 2004). The temperature profile is identical to the one used in our control experiments and the low-level moisture is unmodified. Hence, the surface-based, undilute CAPE remains the same as in the control experiments. The moist environmental sounding is displayed in Fig. 4.21b. Neglecting water loading, the effective CAPE in the control experiments must be smaller than the CAPE in the moist experiments. At any given vertical level, the entrainment and mixing of depressed water vapor mixing ratios into the updraft are greater in a drier atmosphere such as the one in the control experiments. As a result, it is anticipated the resulting buoyancy of the updraft in a drier atmosphere will be marginalized with respect to the

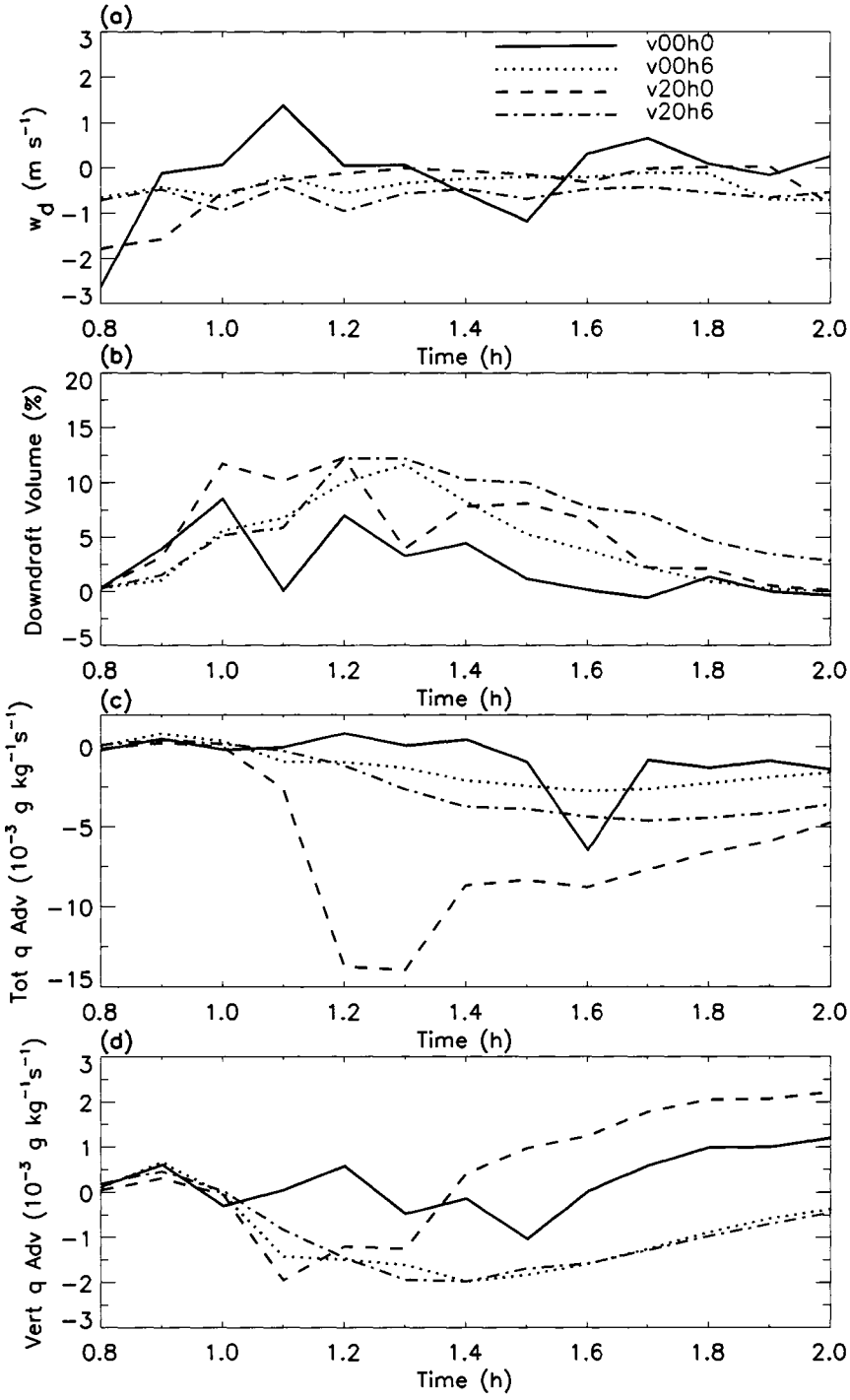

Figure 4.25: Differences between the unstable and control experiments' (a) volume-average downdraft speed (m s^{-1}), (b) percent of domain volume in a wet downdraft, (c) cold pool average advection of water vapor (10^{-3} g kg^{-1} s^{-1}), and (d) cold pool average vertical advection of water vapor (10^{-3} g kg^{-1} s^{-1}).

	τ_l	h_{max}	w_{max}	w_{min}
v00h0	0.5	15.4	43.7	-13.6
v20h0	1.3	14.9	33.4	-12.5
v00h6	0.8	12.4	26.6	-7.1
v20h6	1.1	12.4	27.6	-7.2

Table 4.3: Convective lifetimes, τ_l (h), maximum height of convection, h_{max} (km), maximum vertical speed, w_{max} (m s^{-1}), and minimum vertical speed, w_{min} (m s^{-1}) for the moist experiments.

moist experiments. However, water loading is increased in a moistened atmosphere and this effect should cancel some of the benefits of decreased dry air entrainment. As in our unstable experiments, the various shear configurations v00h0, v20h0, v00h6, and v20h6 are applied to our moist troposphere experiments.

For the given ambient shears, the convective morphology in a moist troposphere is qualitatively similar to convective behavior in the control experiments. However, the increased vigor of convection is readily apparent in all shears. The two right-hand columns in Fig. 4.22 provide selected snapshots of total condensate through time for the moist v00h6 and v20h6 experiments. The horizontally sheared convection again splits into two oppositely moving updrafts, but their dispersion rates from the center are considerably slower than in our control and unstable experiments. Once again, vertical shear promotes rotating updrafts and horizontal shear elongates convection along a preferred axis. Table 4.3 provides some simple statistical properties of the convective clouds in our moist experiments. In comparing these moist experiments with our control experiments, h_{max} for v00h0 and v20h0 increases by 0.5 km, while h_{max} increases by 2.5–3 km for the horizontally sheared convection. Vertical velocities are stronger for all moist experiments, where the horizontally sheared convection experiences the most dramatic enhancements. In the moist experiments, v00h0, v20h0, v00h6, and v20h6 experience increases of 5.9, 0.5, 14.3, and 12.4 m s^{-1}, respectively, in

$w_{\max}$. Because no convective redevelopment occurs in the unsheared experiment, τ_l is nearly a quarter of its value in the control experiments, whereas all of the sheared updrafts are longer-lived within the moist environment. Overall, it appears the benefits of decreased entrainment outweigh additional water loading in the moist experiments.

Overall, the differences portrayed in Fig. 4.26 demonstrate the stronger nature of updrafts in our moist environment. For the most part, volume-averaged vertical velocities in the updraft are greater in the moist experiments. The horizontally-sheared convection is no longer suppressed and experiences 1–3 m s^{-1} stronger updrafts than in our control experiments (Fig. 4.26a). After 1 h, the updraft surface area grows between 60 % (v00h0) to 110 % (v20h0) larger than in our control experiments. Although young updrafts contain greater volume-average buoyancy during early development in the moist atmosphere, their buoyancy is generally less after 1 h. Both the larger surface area experienced after 1 h and increased water loading may explain the lack of enhanced buoyancy in our moist experiments' updrafts.

The cold pool differences between the control and moist experiments act in opposite senses depending on the ambient shear (Fig. 4.27). Because of the increased vigor of the horizontally sheared convection, the strength (i.e., $\langle \Delta\theta \rangle_c$) and size of the cold pools increase in the moist experiments. The exception to this rule is found in v00h0, which experiences a later decrease in cold pool strength as secondary convection now fails to form. While there is a slight decrease of about 0.25 K in v20h0's cold pool strength around 1.5 h, the differences become positive due to stronger convection and a longer storm lifespan. The largest cold pool changes are seen in $\langle \Delta\theta_e \rangle_c$ for v20h0. In v20h0, the moistened atmosphere decreases the negative impact of downdrafts on surface θ_e observed in the control experiments. In contrast with v20h0, v20h6 does not show a decrease in θ_e primarily because the convection in the control v20h6 was suppressed in comparison to the moist background.

Figure 4.28 suggests some of the reasons for cold pool differences between our

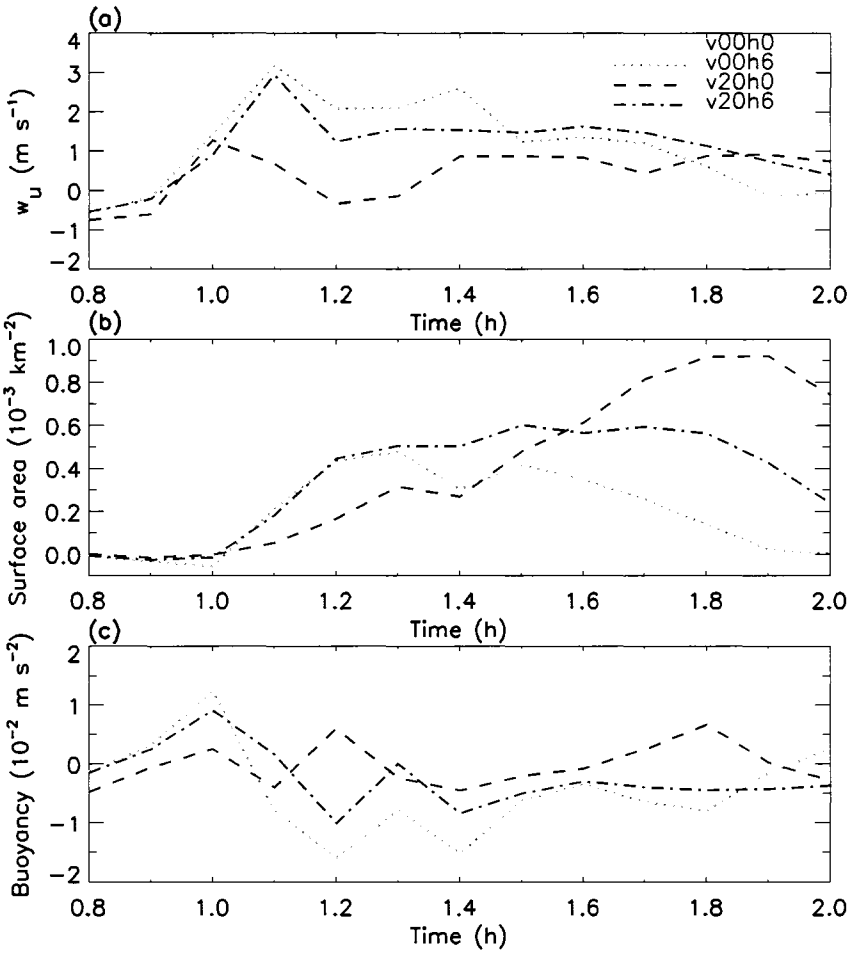

Figure 4.26: Differences between the moist and control experiments' (a) volume-average updraft speed (m s^{-1}), (b) surface area of the updraft (10^{-3} km^2), and (c) volume-average updraft buoyancy (10^{-2} m^{-1} s^{-2}).

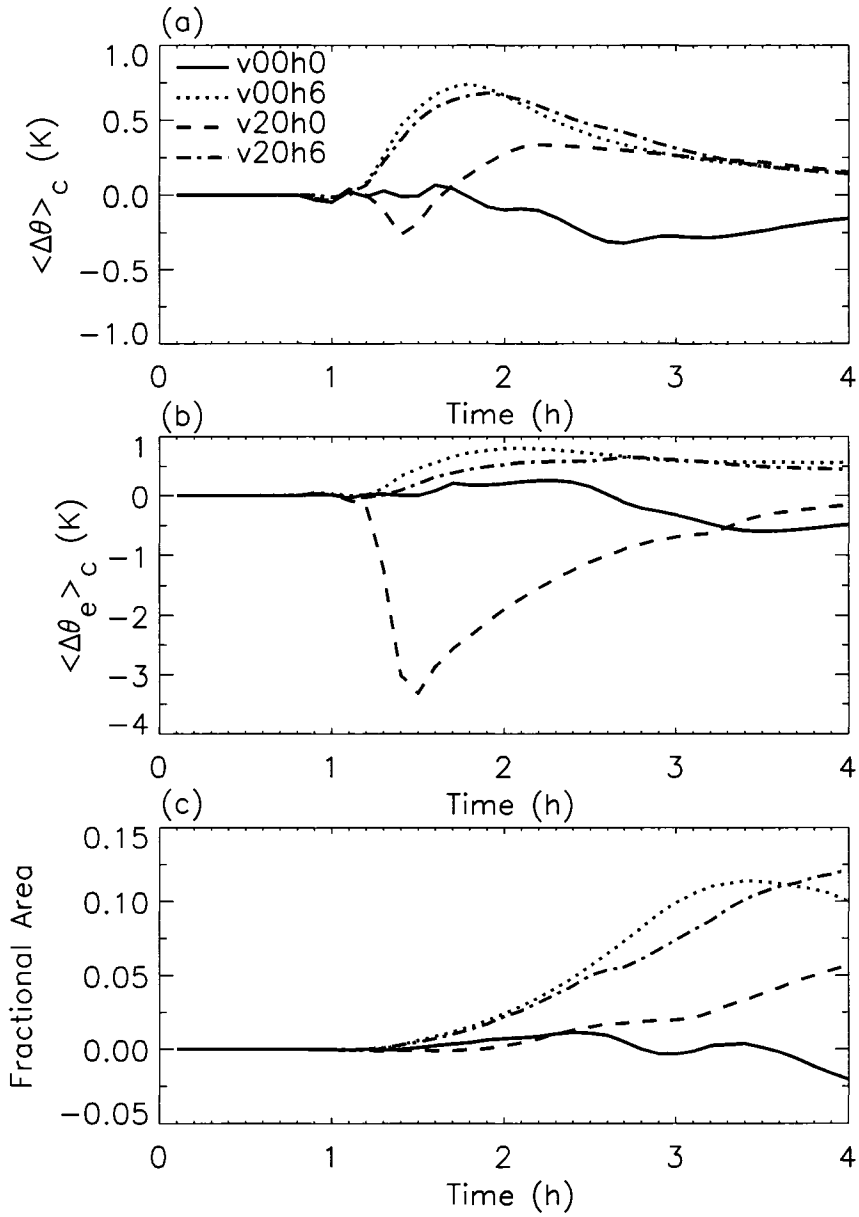

Figure 4.27: (a) The difference in cold pool strengths between the moist and control experiments for cases v00h0, v00h6, v20h0, and v20h6, (b) corresponding θ_e deficit differences, and (c) difference in fraction of the domain covered by a cold pool.

moist and control experiments. Consistent with decreased evaporative cooling, the volume-average downdraft speeds are slightly less than in the control experiments. An exception to this rule is found at earlier times since the overall invigorated convection creates stronger dynamically-driven downdrafts. Now, the downdraft volume increases dramatically for all moist experiments (Fig. 4.28b) and these changes are particularly pronounced for v20h0. Yet, v20h0's θ_e deficit is substantially weaker than in the control experiments. It turns out this there is decreased dry air advection into low-levels. This effect is shown in Figs. 4.28c,d, which shows both the cold pool average water vapor advection and the vertical component of the water vapor advection differences are positive for the moist v20h0 experiment. In reality, the moist v20h0 produces very little dry air advection while the control v20h0 exhibits considerable dry-air advection of the amount indicated in Figs. 4.28c,d. The horizontally sheared convection has the opposite result because, in comparison with the control experiments, the convection in v00h6 and v20h6 is not suppressed in the moist troposphere.

4.5 Summary of key results

In summary, rich dynamics are revealed in our idealized study of convection in horizontal and vertical shears. The cloud dynamics in the cases of zero shear and vertical shear follow well-documented morphologies. The basic dynamics of vertically sheared convection is summarized in Fig. 4.29.

Inclusion of horizontal shear is relatively poorly studied and new dynamical behaviors are identified. A background of constant lateral shear (i.e., shear in the meridional component of wind) has the following impacts on convective lifecycles for our control sounding:

- Horizontal shear organizes convective plumes into elongated cells that tend toward parallel modes. Banded structures occur because transverse gradients in vertical motion grow while longitudinal gradients remain diffuse. This

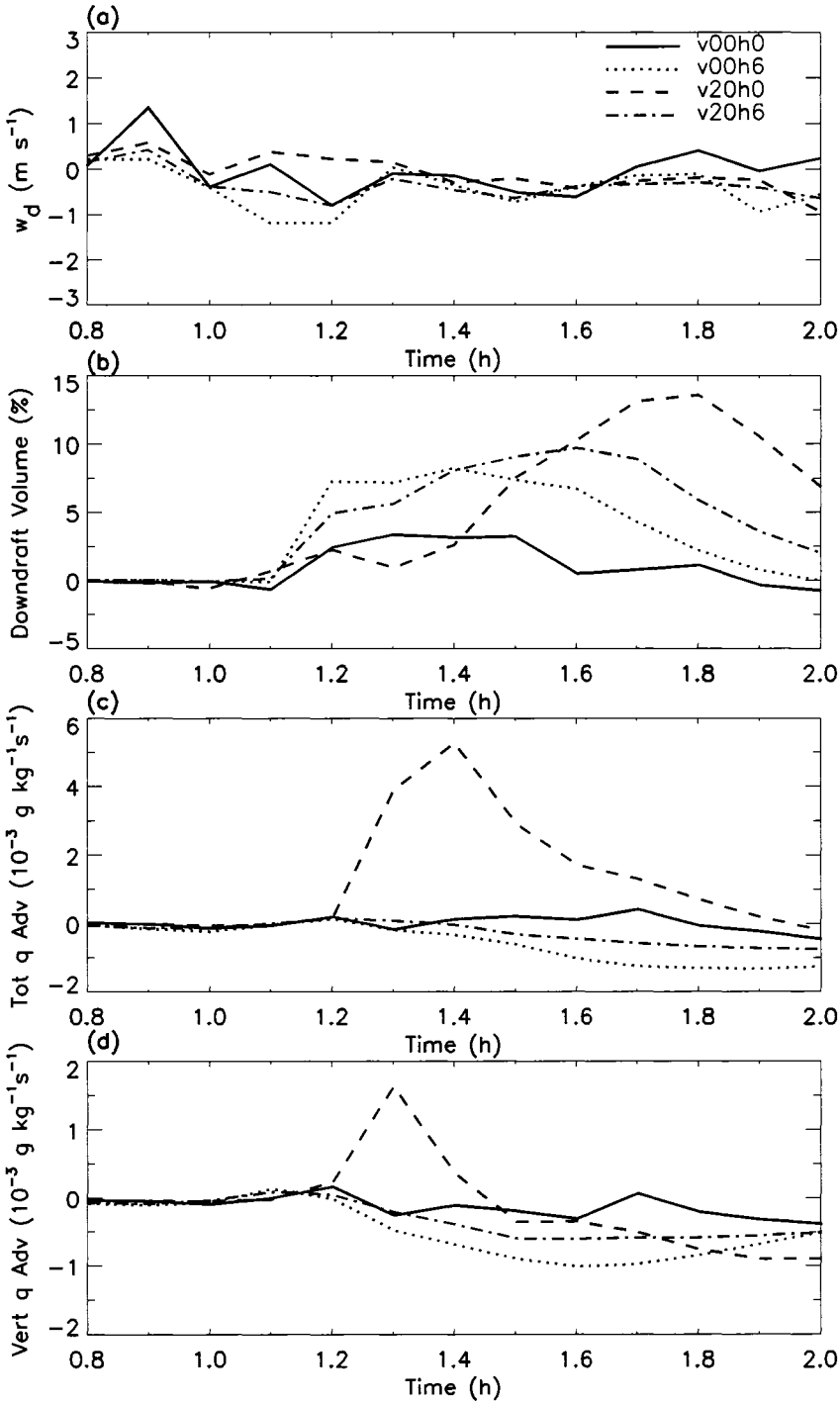

Figure 4.28: Differences between the moist and control experiments' (a) volume-average downdraft speed (m s^{-1}), (b) percent of domain volume in a wet downdraft, (c) cold pool average advection of water vapor (10^{-3} g kg^{-1} s^{-1}), and (d) cold pool average vertical advection of water vapor (10^{-3} g kg^{-1} s^{-1}).

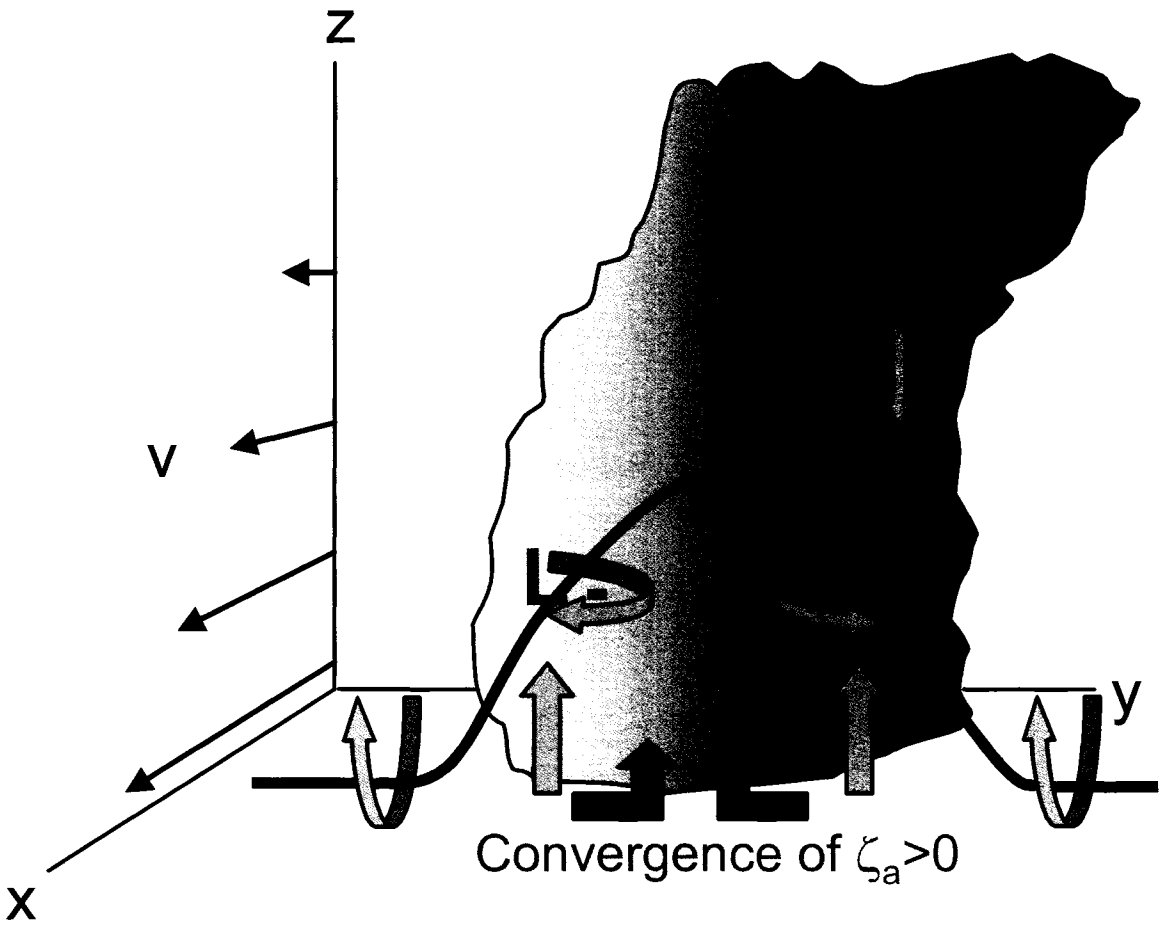

Figure 4.29: An idealized schematic of vertically sheared convection. A convective cloud is tilted downshear by vertical shear. Horizontal vorticity associated with the background vertical shear, which is denoted by the thick curve, is tilted upward by the updraft. This tilted vorticity leads to a vorticity dipole. Rotation contributes to dynamic pressure perturbations which help split the updraft into two oppositely rotating updrafts. Downdrafts occur downshear. Cyclonic background vorticity is converged at low-levels and leads to a bias in cyclonic vorticity.

asymmetric gradient in vertical motion leads to differential tilting of the vorticity associated with the overturning circulation and results in a quadropole vorticity pattern that forces subsidence on the plume's transverse flanks.

- In a background of positive vertical vorticity, horizontally sheared convection stretches this vorticity and leaves behind a filamented positive wake of vorticity.

- If horizontal shear is not too strong, vigorous cellular convection initiates at the longitudinal edges of the cold pool.

- Most likely due to enhanced entrainment and mixing, sufficiently strong horizontal shear suppresses deep convective clouds in the control environment.

- Cold pools become elliptical and weaker in the presence of enhanced horizontal shear. Downward motion and increased CIN suppress convection along the transverse flanks of the cold pool, while new convection is favored along the longitudinal flanks of the cold pool. In contrast to symmetric cell regeneration along an axisymmetric cold pool in no shear, asymmetric buoyant forcing along the cold pool's gust front essentially leads to storm splitting in horizontal shear.

Many key aspects of the dynamics of a horizontally sheared cumulonimbus cloud are illustrated in Fig. 4.30.

In the situation of our control sounding, when convective clouds are placed in costant horizontal and vertical shears of the meridional flow, the following noteworthy behaviors are displayed:

- Convective clouds in both horizontal and vertical shears exhibit morphologies that combine many aspects of convective dynamics in either type of shear alone. Horizontal shear organizes convection toward a longitudinal band. Stronger horizontal shear still suppresses convection. Sufficiently strong vertical shear leads to mesocyclones.

- The vorticity dynamics combine the vorticity patterns associated with horizontal shear and the tilting of the horizontal vorticity associated with the vertical shear, which imposes dynamic pressure perturbation lift on updraft flanks. Splitting is largely governed by the asymmetric, horizontally sheared

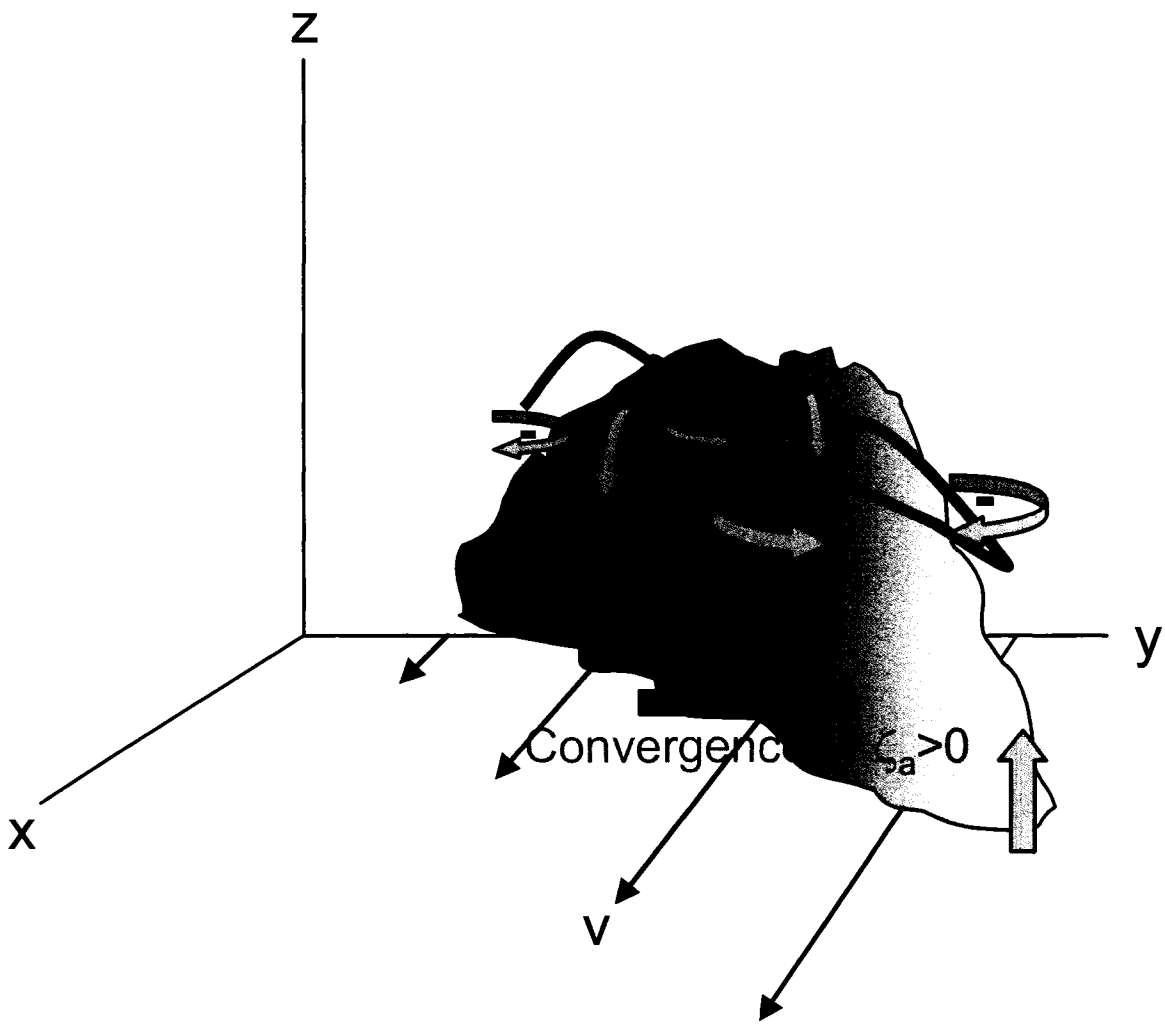

Figure 4.30: An idealized schematic of horizontally sheared convection. A convective cloud is elongated by the horizontal shear. The overturning circulation produces a vortex line indicated by the thick black curve surrounding the top of the convective cloud. Differential vertical motion tilts this vortex line on the longitudinal flanks of the cloud. Vortex tilting leads to an upper level vorticity quadrupole and transverse circulation. The figure also emphasizes the importance of the convergence of background positive vorticity.

cold pool forcing, but dynamic pressure perturbations constructively contribute to splitting, especially in environments possessing lower horizontal shear.

- With vertical shear, the downshear cell contains anticyclonic vorticity while the upshear cell contains cyclonic vorticity.

- A wake of cyclonic and anticyclonic vorticity is left behind as updrafts split and disperse. In lower horizontal shear, the anticyclonic vorticity is highly filamentary and the cyclonic vorticity is relatively more concentrated. As horizontal shear increases, increased symmetry in this filamentary vorticity dipole is achieved.

- Vertical shear increases the strength and dryness of cold pools of horizontally sheared convection.

Finally, experiments modifying the background thermodynamic sounding demonstrate substantial convective sensitivities.

- Convection is greatly invigorated and detrimental filamentation is alleviated by a slight 1 K cooling in the low-level temperature profile.

- Enhanced cold pools are formed due to more intense and larger downdrafts in the slightly more unstable atmosphere.

- Moistening our control sounding also leads to invigorated convection in even the strongest shear situations and therefore suggests that entrainment and mixing were probably important in suppressing strongly sheared convection in the control experiments.

Chapter 5

CONCLUSIONS

5.1 Summary and discussion

In this work, we examined various aspects of moat formation in tropical cyclones. In Chapter 2, we hypothesized rapid filamentation zones, regions of enhanced strain outside of the core of intense vortices, create unfavorable conditions for deep, moist convection. While it is well established subsidence and its associated static stability act as barriers to convective development in a mature moat, our work suggests rapid filamentation is another mechanism that may contribute to moat formation in concentric eyewall formation. We used the Okubo-Weiss and Hua-Klein stirring criteria for 2D flows to estimate exponential growth rates of gradients associated with filamenting structures in predominantly strain-dominated regions. Relaxing the assumption of a slowly-varying velocity gradient tensor, the Hua-Klein stirring criterion estimated stronger filamentation zones than analyzed in Rozoff et al. (2006). The validity of these 2D criteria is questionable for even 2D, axisymmetric vortices (e.g., Lapeyre et al., 1999) and further challenged in the context of the complex and active nature of 3D convection. Nonetheless, the rapid filamentation concepts should apply to convection in flows with intense strain. Furthermore, the simple 2D rapid filamentation criteria can be easily revised in order to account for the increased complexity of 3D, convective flows.

In Chapter 3, we explored flight-level and dropsonde observations in Hurricanes Frances (2004) and Rita (2005), both of which produced eyewall replacement cycles.

According to 2D stirring criteria, the region immediately outside of a primary eyewall persistently qualified as a rapid filamentation zone. Closer to the inner eyewall, dropsondes suggested the low-level convective instability was most often reduced before and after secondary eyewall formation. On occasion, dropsondes exhibited low-level buoyancy just outside the primary eyewall both before and after moat formation. Flight-level data generally possessed larger dewpoint depressions in this region as well. At larger radii, greater low-level convective instability was found in both individual and composite dropsondes both before and after secondary eyewall formation. These regions were also in less adverse horizontal strain. Thus, some ambiguity remains as to whether rapid filamentation or subsidence predominate in the formation of a moat. In the context of a balanced vortex model, solutions to a simple, analytical approximation of the Sawyer-Eliassen transverse circulation equation suggest that, as a secondary eyewall forms and contracts, the moat continues to experience increasing eye-like subsidence and warming rates. It is therefore likely that rapid filamentation theory is most relevant during earlier time periods in an ERC. Nonetheless, rapid filamentation may still play an important role in more convectively unstable regions outside of an established outer eyewall.

Idealized 3D cloud simulations were summarized in Chapter 4. Our experiments covered a spectrum of constant horizontal and vertical shears. For simplicity, curvature was neglected and the background vorticity was kept at a constant 1×10^{-4} for all values of horizontal shear. The background thermodynamic environment was constructed from dropsondes and a deep-layer proximity sounding associated with Category 5 Hurricane Isabel (2003), and consequently, this composite sounding contained marginal low-level instability representive of the marginal thermodynamics common to convection outside of intense TC cores prior to concentric eyewall formation. Above low-levels, the sounding was relatively dry, which led to vigorous downdrafts once deep convective clouds formed in these experiments. Convective plumes

were initialized via low-level convective bubbles in these shear flows and allowed to evolve.

Although convection was never particularly long-lived in any of our sheared convection experiments, interesting dynamics were revealed by convection over a wide spectrum of hurricane-like shears of the meridional ("tangential") winds. In the experiments with horizontal shear, a practical threshold for rapid filamentation was revealed in our control experiments. Despite the evidently changing τ_{conv} as convection transitions from a low-level plume into strong, splitting cellular convective cells, convection was weakened in horizontal shear. Updraft statistics and the moist sensitivity experiment indicated that weakening is most likely attributable to increased dry-air entrainment. Consequently, an effective rapid filamentation zone was found in our control experimental configuration to take place for $v_x \leq -6 \times 10^{-4}$.

Our experiments indicated that certain distributions of PV wakes are left behind convective cells depending on the background shear. Horizontal shear contributed to long filaments of enhanced cyclonic vorticity with a broad region of slightly anticyclonic vorticity encompassing the filaments. Stronger horizontal shear weakened the magnitude of the vorticity filament. Smaller-scale vorticity quadrupoles formed at the top of horizontally sheared convection and were advected downward along the transverse flanks of the updraft. Vertical shear introduced vorticity dipoles through the tilting of horizontal vorticity and horizontal shear filamented these vorticity patterns. In agreement with Franklin et al. (2006), who revealed vorticity dipoles created through the tilting of diabatically generated PV in rainband stratiform regions, our small-scale convection also generated impressive PV dipole structures, which may be important in accelerating or decelerating the mean flow. The PV patterns we found are strongly dependent on the varying amounts of shear and suggest that different regions of a TC should lead to different vorticity generation patterns in the presence of convection. How these PV structures in TC intensity and concentric eyewall

formation are related are yet to be resolved.

Sensitivity experiments that increased either the low-level potential instability or the troposphere's relative humidity were performed with key shear configurations. The results were remarkable. The threshold of adverse shear was shown to be quite sensitive to background instability. Thus, we expect rapid filamentation zones to be larger for environments characterized by less instability and small filamentation zones to exist in very convectively unstable environments. Perhaps what should be evaluated to determine likely areas of convection in TCs is an empirically-based ratio between τ_{conv} and τ_{fil}, where τ_{conv} is some function of instability. In regions where $\tau_{\text{conv}}/\tau_{\text{fil}}$ is smaller, convection would be more likely.

5.2 Suggestions for future research

While this work begins to give us an understanding of moat formation, more theoretical progress can certainly be made in analyzing the effects of strain on convection. We also encourage more observational analysis over a large sample of intense TCs. Deep-layer soundings would be particularly beneficial to address convection outside of the primary eyewall. Nonetheless, outer eyewalls and other tertiary convective clouds are often shallower than inner eyewalls. Therefore, the restricted height of thermodynamic profiles provides proportionally more information about potential buoyancy available to outer convective clouds.

Much more can be learned from idealized convection studies. Our experimental configuration only considered constant shears of the tangential wind, v_θ. In real TCs, shear is often not constant. Also, there is strong low-level inflow associated with the v_r component of wind that adds curvature to a hodograph. We therefore expect typical hurricane hodographs to favor cyclonic updrafts (Rotunno and Klemp, 1982). The anticipated cyclonic bias should impact rainband dynamics and vorticity wakes. Moreover, the strong low-level inflow can contain cold pools, although strong horizon-

tal shear appears to have this effect too for a given thermodynamic background. With essentially parallel deep-layer shear and the perpendicular low-level shear, it would be interesting to compare rainband dynamics with the parallel stratiform shear situations considered in Parker (2007a,b). Also, our experiments were carried out with rather modest, but constant, values of background vorticity. In the region that becomes a moat in an ERC, greater values of background vorticity often exist and may even be associated with a gradient in vorticity. The effects of such vorticity on the dynamics of sheared convection would be prudent to study.

A full theory for eyewall replacement cycles may require rapid filamentation zones. In an environment already characterized by modest convective instability, rapid filamentation zones most likely decrease the probability of secondary eyewall formation within certain radial distances of a primary eyewall. In other words, forcing mechanisms necessary for the acceleration of the azimuthally mean flow outside of the primary eyewall would need to act at sufficiently far distances so that convection has the opportunity to couple with these secondary wind/vorticity maxima. If these essential forcing mechanisms are vortex Rossby waves, then the likelihood of secondary eyewall formation should depend strongly on the azimuthally mean vorticity structure. Also, our idealized convection results show that certain combinations of cyclonic and anticyclonic vorticity wakes are left behind and these distributions depend on the combination of horizontal and vertical shears. Perhaps certain combinations of horizontal and vertical shear are needed to produce the most ideal vorticity patterns for secondary eyewall formation. Therefore, secondary eyewall formation would strongly depend on the mean radial distribution of horizontal and vertical shears. Should a secondary wind maximum form in a region sufficient for moist convection, then this convection may further concentrate postive vertical vorticity ("vortex stretching"). Positive air-sea feedbacks associated with enhanced surface fluxes of latent and sensible heat (Nong and Emanuel, 2003) would provide the extra energy to maintain the

incipient eyewall. The above chain-hypothesis is consistent with a hypothesis recently constructed from a full hurricane simulation in RAMS (W. D. Terwey, personal communication) and will be published soon. Once an incipient secondary eyewall forms, inertial stability is locally increased in the region of the secondary eyewall, and perhaps in the moat if PV mixing occurs there (e.g., Kossin et al., 2000). Contraction of the outer eyewall is enhanced by increased moat inertial instability. As subsidence increases in the moat, rapid filamentation is no longer as relevant in the moat dynamics, except to filament transient convection that occasionally appears there. To evaluate the role of rapid filamentation in convective processes in concentric eyewalls, analysis of 3D hurricane simulations is recommended.

BIBLIOGRAPHY

Arakawa, A., and V. R. Lamb, 1981: A potential enstrophy and energy conserving scheme for the shallow water equations. *Mon. Wea. Rev.* , **109**, 18–36.

Barnes, G. M., E. J. Zipser, D. Jorgensen, and F. Marks, Jr., 1983: Mesoscale and convective structure of a hurricane rainband. *J. Atmos. Sci.*, **40**, 2125–2137.

Barnes, G. M., J. F. Gamache, M. A. LeMone, and G. S. Stossmeister, 1991: A convective cell in a hurricane rainband. *Mon. Wea. Rev.*, **119**, 776–794.

Barnes, S. L., 1973: Mesoscale objective analysis using weighted time-series observations. NOAA Tech. Memo. ERL NSSL-62, National Severe Storms Laboratory, Norman, OK 73069, 60 pp.

Basdevant, C., and T. Philipovitch, 1994: On the validity of the "Weiss criterion" in two-dimensional turbulence. *Physica D*, **73**, 17–30.

Bell, M. M., and M. Montgomery, 2007: Observed structure, evolution and potential intensity of category five Hurricane Isabel (2003) from 12–14 September. *Mon. Wea. Rev.*, in press.

Bevin, J., 2004: Tropical cyclone report on Hurricane Frances (2004). National Hurricane Center/Tropical Prediction Center.

Black, M. L., and H. E. Willoughby, 1992: The concentric eyewall cycle of Hurricane Gilbert. *Mon. Wea. Rev.* , **120**, 947–957.

Black, P. G., H. V. Senn, and C. L. Courtright, 1972: Airborne radar observations of eye configuration changes, bright-band distribution, and precipitation tilt during the 1969 muliple seeding experiments in Hurricane Debbie. *Mon. Wea. Rev.*, **100**, 208–217.

Brooks, H. E., C. A. Doswell III, and L. J. Wicker, 1993: STORMTIPE: a forecasting experiment using a three-dimensional cloud model. *Wea. Forecasting*, **8**, 352–362.

Chen, Y., and M. K. Yau, 2001: Sprial bands in a simulated hurricane. Part I: vortex Rossby wave verification. *J. Atmos. Sci.*, **58**, 2128–2145.

Chen, Y., G. Brunet, and M. K. Yau, 2003: Spiral bands in a simulated hurricane. Part II: wave activity diagnostics. *J. Atmos. Sci.*, **60**, 1239–1256.

Cohen, C., 2000: A quantitative investigation of entrainment and detrainment in numerically simulated cumulonimbus clouds. *J. Atmos. Sci.*, **57**, 1657–1674.

Cotton, W. R., and Coauthors, 2003: RAMS 2001: current status and future directions. *Meteor. Atmos. Phys.*, **82**, 5–29.

Crook, N. A., 1996: Sensitivity of moist convection forced by boundary layer processes to low-level thermodynamic fields. *Mon. Wea. Rev.*, **124**, 1767–1785.

Davies-Jones, R. P., 1971: Thermal convection in a horizontal plane Couette flow. *J. Fluid Mech.*, **49**, 193–205.

Derbyshire, S. H., I. Beau, P. Bechtold, J.-Y. Grandpeix, J.-M. Piriou, J.-L. Redelsperger, and P. M. M. Soares, 2004: Senstivity of moist convection to environmental humidity. *Q. J. R. Meteorol. Soc.*, **130**, 3055–3079.

Dodge, P., R. W. Burpee, and F. D. Marks Jr., 1999: The kinematic structure of a hurricane with sea level pressure less than 900 mb. *Mon. Wea. Rev.*, **127**, 987–1004.

Dresselhaus, E., and M. Tabor, 1991: The kinematics of stretching and alignment of material elements in general flow fields. *J. Fluid Mech.*, **236**, 415–444.

Dritschel, D. G., and D. W. Waugh, 1992: Quantification of the inelastic interaction of unequal vortices in two-dimensional vortex dynamics. *Phys. Fluids A*, **4**, 1737–1744.

Eastin, M. D., P. G. Black, and W. M. Gray, 2002: Flight-level instrument wetting errors in hurricanes. Part I: observations. *Mon. Wea. Rev.*, **133**, 209–227.

Eliassen, A., 1951: Slow thermally or frictionally controlled meridional circulation in a circular vortex. *Astrophys. Norv.*, **5**, 19–60.

Emanuel, K. A., 1988: The maximum intensity of hurricanes. *J. Atmos. Sci.*, **45**, 1143–1155.

Fortner, L. E., 1958: Typhoon Sarah, 1956. *Bull. Amer. Meteor. Soc.*, **39**, 633–639.

Franklin, C. N., G. J. Holland, and P. T. May, 2006: Mechanisms for the generation of mesoscale vorticity features in tropical cyclone rainbands. *Mon. Wea. Rev.*, **134**, 2649–2669.

Franklin, J., M. L. Black, and K. Valde, 2003: GPS dropwindsonde wind profiles in hurricanes and their operational implications. *Wea. Forecasting*, **18**, 32–44.

Fulton, S. R., and W. H. Schubert, 1987: Chebyshev spectral methods for limited-area models. Part II. Shallow water model. *Mon. Wea. Rev.*, **115**, 1954–1965.

Gamache, J. F., and R. A. Houze Jr., 1982: Mesoscale air motions associated with a tropical squall line. *Mon. Wea. Rev.*, **110**, 118–135.

Gentry, R. C., 1969: Project STORMFURY. *Bull. Amer. Meteor. Soc.*, **50**, 404–409.

Gilmore, M., and L. J. Wicker, 1998: The influence of mid-tropospheric dryness on supercell morphology and evolution. *Mon. Wea. Rev.*, **126**, 943–958.

Guinn, T. A., and W. H. Schubert, 1993: Hurricane spiral bands. *J. Atmos. Sci.*, **50**, 3380–3403.

Haller, G., 2005: An objective definition of a vortex. *J. Fluid Mech.*, **525**, 1–26.

Hart, J. E., 2000: The modulation of convection by a lateral shear. *J. Atmos. Sci.*, **57**, 1169–1180.

Hausman, S. A., 2001: Formation and sensitivity analysis of a nonhydrostatic, axisymmetric tropical cyclone model. Colorado State University Department of Atmospheric Science Paper No. 701, 210 pp.

Hawkins, H. F., and D. T. Rubsam, 1968: Hurricane Hilda, 1964. II: structure and budgets of the hurricane on 1 October 1964. *Mon. Wea. Rev.*, **96**, 617–636.

Hawkins, H. F., 1971: Comparison of results of the Hurricane Debbie (1969) modification experiments with those from Rosenthal's numerical model simulation experiments. *Mon. Wea. Rev.*, **99**, 427–434.

Hawkins, J. D., M. Helveston, T. F. Lee, F. J. Turk, K. Richardson, C. Sampson, J. Kent, and R. Wade, 2006: Tropical cyclone multiple eyewall configurations. Preprints, 27th Conference on Hurricanes and Tropical Meteorology, Monterey, CA, Amer. Meteor. Soc., 6 pp.

Hill, G. E., 1974: Factors controlling the size and spacing of cumulus clouds as revealed by numerical experiments. *J. Atmos. Sci.*, **31**, 646–673.

Hock, T. F., and J. L. Franklin, 1999: The NCAR GPS dropwindsonde. *Bull. Amer. Met. Soc.*, **80**, 407–420.

Holland, G. J., 1997: The maximum potential intensity of tropical cyclones. *J. Atmos. Sci.*, **54**, 2519–2541.

Holliday, C. R., 1977: Double intensification of Typhoon Gloria, 1974. *Mon. Wea. Rev.*, **105**, 523–528.

Hoose, H. M., and J. A. Colon, 1970: Some aspects of the radar structure of Hurricane Beulah on September 9, 1967. *Mon. Wea. Rev.*, **98**, 529–533.

Houze, R. A., S. S. Chen, W.-C. Lee, R. F. Rogers, J. A. Moore, G. J. Stossmeister, M. M. Bell, J. Cetrone, W. Zhao, and S. R. Brodzik, 2006: The Hurricane Rainband and Intensity Change Experiment: observations and modeling of Hurricanes Katrina, Ophelia, and Rita. *Bull. Amer. Meteor. Soc.*, **87**, 1503–1521.

Houze, R. A., S. S. Chen, B. F. Smull, W.-C. Lee, and M. M. Bell, 2007: Hurricane intensity and eyewall replacement. *Science*, **315**, 1235–1239.

Hua, B. L., and P. Klein, 1998: An exact criterion for the stirring properties of nearly two-dimensional turbulence. *Physica D*, **113**, 98–110.

Hua, B. L., J. C. McWilliams, and P. Klein, 1998: Lagrangian accelerations in geostrophic turbulence. *J. Fluid Mech.*, **366**, 87–108.

Jordan, C. L., and F. J. Schatzle, 1961: The "double eye" of Hurricane Donna. *Mon. Wea. Rev.*, **94**, 454–458.

Jordan, C. L., 1966: Surface pressure variations at coastal stations during the period of irregular motion of Hurricane Carla of 1961. *Mon. Wea. Rev.*, **94**, 454–458.

Jorgensen, D. P., 1984: Mesoscale and convective-scale characteristics of mature hurricanes. *J. Atmos. Sci.*, **41**, 1268–1285.

Kimura, Y., and J. R. Herring, 2001: Gradient enhancement and filament ejection for nonuniform elliptic vortex in 2D turbulence. *J. Fluid Mech.*, **439**, 43–56.

Klein, P., B. L. Hua, and G. Lapeyre, 2000: Alignment of tracer gradient vectors in 2D turbulence. *Physica D*, **146**, 246–260.

Klemp, J. B., and R. B. Wilhelmson, 1978a: The simulation of three-dimensional convective storm dynamics. *J. Atmos. Sci.* , **35**, 1070–1096.

Klemp, J. B., and R. B. Wilhelmson, 1978b: Simulations of right- and left-moving storms produced through storm splitting *J. Atmos. Sci.*, **35**, 1097–1110.

Klemp, J. B., 1987: Dynamics of tornadic thunderstorms. *Ann. Rev. Fluid Mech.*, **19**, 369–402.

Knabb, R. D., D. P. Brown, and J. R. Rhome, 2006: Tropical cyclone report on Hurricane Rita, 18–26 September 2005. National Hurricane Center.

Kossin, J. P., W. H. Schubert, and M. T. Montgomery, 2000: Unstable interactions between a hurricane's primary eyewall and a secondary ring of enhanced vorticity. *J. Atmos. Sci.*, **57**, 3893–3917.

Kossin, J. P., and M. D. Eastin, 2001: Two distinct regimes in the kinematic and thermodynamic structure of the hurricane eye and eyewall. *J. Atmos. Sci.*, **58**, 1079–1090.

Kossin, J. P., and W. H. Schubert, 2001: Mesovortices, polygonal flow patterns, and rapid pressure falls in hurricane-like vortices. *J. Atmos. Sci.*, **58**, 2196–2209.

Kossin, J. P., B. D. McNoldy, and W. H. Schubert, 2002: Vortical swirls in hurricane eye clouds. *Mon. Wea. Rev.*, **130**, 3144–3149.

Kuo, H.-C., L.-Y. Lin, C.-P. Chang, and R. T. Williams, 2004: The formation of concentric vorticity structures in typhoons. *J. Atmos. Sci.*, **61**, 2722–2734.

Lapeyre, G., P. Klein, and B. L. Hua, 1999: Does the tracer gradient vector align with the strain eigenvectors in 2D turbulence? *Phys. Fluids*, **11**, 3729–3737.

Lapeyre, G., B. L. Hua, and P. Klein, 2001: Dynamics of the orientation of active and passive scalars in two-dimensional turbulence. *Phys. Fluids*, **13**, 251–264.

Lee, B. D., and R. B. Wilhelmson, 1997: The numerical simulation of non-supercell tornadogenesis. Part II: evolution of a family of tornadoes along a weak outflow boundary. *J. Atmos. Sci*, **54**, 2387–2415.

Lilly, D. K., 1962: On the numerical simulation of buoyant convection. *Tellus*, **14**, 148–172.

Louazel, S., and B. L. Hua, 2004: Vortex erosion in a shallow-water model. *Phys. Fluids*, **16**, 3079–3085.

Lukovich, J. V., and T. G. Shepherd, 2005: Stirring and mixing in two-dimensional divergent flow. *J. Atmos. Sci.*, **62**, 3933–3954.

Mallen, K. J., M. T. Montgomery, and B. Wang, 2005: Reexamining the near-core radial structure of the tropical cyclone primary circulation: implications for vortex resiliency. *J. Atmos. Sci.*, **62**, 408–425.

Mariotti, A., B. Legras, and D. G. Dritschel, 1994: Vortex stripping and the erosion of coherent structures in two-dimensional flows. *Phys. Fluids A*, **6**, 3954.

Marks, F. D., Jr., 1985: Evolution of the structure of precipitation in Hurricane Allen (1980). *Mon. Wea. Rev.*, **113**, 909–930.

May, P. T., G. J. Holland, and W. L. Ecklund, 1994: Wind profiler observations of Tropical Storm Flo at Saipan. *Wea. Forecasting*, **9**, 410–426.

May, P. T., 1996: The organization of convection in the rainbands of Tropical Cyclone Laurence. *Mon. Wea. Rev.*, **124**, 807–815.

May, P. T., and D. K. Rajopadhyaya, 1996: Wind profiler observations of vertical motion and precipitation microphysics of a tropical squall line. *Mon. Wea. Rev.*, **124**, 621–633.

May, P. T., and G. J. Holland, 1999: The role of potential vorticity generation in tropical cyclone rainbands. *J. Atmos. Sci.*, **56**, 1224–1228.

McCaul, E. W., Jr., 1987: Observations of the Hurricane Danny tornado outbreak of 16 August 1985. *Mon. Wea. Rev.*, **115**, 1206–1223.

McCaul, E. W., Jr., and M. L. Weisman, 1996: Simulations of shallow supercell storms in landfalling hurricane environments. *Mon. Wea. Rev.*, **124**, 408–429.

McCaul, E. W., and M. L. Weisman, 2001: The sensitivity of simulated supercell structure and intensity to variations in the shapes of environmental buoyancy and shear profiles. *Mon. Wea. Rev.*, **129**, 664–687.

Melander, M. V., J. C. McWilliams, and N. J. Zabusky, 1987: Axisymmetrization and vorticity-gradient intensification of an isolated two-dimensional vortex through filamentation. *J. Fluid Mech.*, **178**, 137–159.

McNoldy, B. D., 2004: Triple eyewall in Hurricane Juliette. *Bull. Amer. Meteor. Soc.*, **85**, 1663–1666.

Möller, J. D., and M. T. Montgomery, 1999: Vortex Rossby-waves and hurricane intensification in a barotropic model. *J. Atmos. Sci.*, **56**, 1674–1687.

Möller, J. D., and M. T. Montgomery, 2000: Tropical cyclone evolution via potential vorticity anomalies in a three-dimensional balance model. *J. Atmos. Sci*, **47**, 3366–3387.

Montgomery, M. T., and R. Kallenbach, 1997: A theory for vortex Rossby-waves and its application to spiral bands and intensity changes in hurricanes. *Quart. J. Roy. Meteor. Soc.*, **123**, 435–465.

Montgomery, M. T., and J. Enagonio, 1998: Tropical cyclogenesis via convectively forced vortex Rossby waves in a three-dimensional quasigeostrophic model. *J. Atmos. Sci.*, **55**, 3176–3207.

Montgomery, M. T., V. A. Vladimirov, and P. V. Denissenko, 2002: An experimental study on hurricane mesovortices. *J. Fluid Mech.*, **471**, 1–32.

Montgomery, M. T., M. M. Bell, S. D. Aberson, and M. L. Black, 2006: Hurricane Isabel (2003): new insights into the physics of intense storms. Part I: mean vortex structure and maximum intensity estimates. *Bull. Amer. Meteor. Soc.*, **87**, 1335–1347.

Nong, S., and K. Emanuel, 2003: A numerical study of the genesis of concentric eye walls in hurricanes. *Q. J. R. Meteor. Soc.*, **129**, 3323–3338.

Okubo, A., 1970: Horizontal dispersion of floatable particles in the vicinity of velocity singularities such as convergence. *Deep-Sea Res.*, **17**, 445–454.

Ooyama, K. V., 1990: A thermodynamic foundation for modeling the moist atmosphere. *J. Atmos. Sci.*, **47**, 2580–2593.

Ooyama, K. V., 2001: A dynamic and thermodynamic foundation for modeling the moist atmosphere with parameterized microphysics. *J. Atmos. Sci.*, **58**, 2073–2102.

Parker, M. D., 2007a: Simulated convective lines with parallel stratiform precipitation. Part I: An Archetype for Convection in Along-Line Shear. *J. Atmos. Sci.*, **64**, 267–288.

Parker, M. D., 2007b: Simulated convective lines with parallel stratiform precipitation. Part II: Governing Dynamics and Associated Sensitivities. *J. Atmos. Sci*, **64**, 289–313.

Pedlosky, J., 1987: *Geophysical fluid dynamics.* Springer-Verlag, 710 pp.

Persing, J., and M. T. Montgomery, 2003: Hurricane superintensity. *J. Atmos. Sci.*, **60**, 2349–2371.

Polvani, L. M., G. R. Flierl, and N. J. Zabusky, 1989: Filamentation of unstable vortex structures via separatrix crossing: a quantitative estimate of onset time. *Phys. Fluids A*, **1**, 181–184.

Powell, M. D., 1990a: Boundary layer structure and dynamics in outer hurricane rainbands. Part I: mesoscale rainfall and kinematic structure. *Mon. Wea. Rev.*, **118**, 891–917.

Prieto, R., B. D. McNoldy, S. R. Fulton, and W. H. Schubert, 2003: A classification of binary tropical-cyclone-like vortex interactions. *Mon. Wea. Rev.*, **131**, 2656–2666.

Raymond, D. J., and H. Jiang, 1990: A theory for long-lived mesoscale convective systems. *J. Atmos. Sci*, **47**, 3067–3077.

Rotunno, R., and K. A. Emanuel, 1987: An air-sea interaction theory for tropical cyclones. Part II: evolutionary study using a nonhydrostatic axisymmetric numerical model. *J. Atmos. Sci.*, **44**, 542–561.

Rotunno, R., and J. B. Klemp, 1982: The influence of the shear-induced pressure gradient on thunderstorm motion. *Mon. Wea. Rev.*, **110**, 136–151.

Rotunno, R., and J. B. Klemp, 1985: On the rotation and propagation of simulated supercell thunderstorms. *Mon. Wea. Rev.*, **42**, 271–292.

Rozoff, C. M., W. H. Schubert, B. D. McNoldy, and J. P. Kossin, 2006: Rapid filamentation zones in intense tropical cyclones. *J. Atmos. Sci.*, **63**, 325–340.

Samsury, C. E., and E. J. Zipser, 1995: Secondary wind maxima in hurricanes: Airflow and relationship to rainbands. *Mon. Wea. Rev.*, **123**, 3502–3517.

Schlesinger, R. E., 1980: A three-dimensional numerical model of an isolated deep thunderstorm. Part II: dynamics of updraft splitting and mesovortex couplet evolution. *J. Atmos. Sci.*, **37**, 395–420.

Schubert, W. H., and J. J. Hack, 1982: Inertial stability and tropical cyclone development. *J. Atmos. Sci.*, **39**, 1687–1697.

Schubert, W. H., and J. J. Hack, 1983: Transformed Eliassen balanced vortex model. *J. Atmos. Sci.*, **40**, 1571–1583.

Schubert, W. H., M. T. Montgomery, R. K. Taft, T. A. Guinn, S. R. Fulton, J. P. Kossin, and J. P. Edwards, 1999: Polygonal eyewalls, asymmetric eye contraction, and potential vorticity mixing in hurricanes. *J. Atmos. Sci.*, **56**, 1197–1223.

Schubert, W. H., S. A. Hausman, M. Garcia, K. V. Ooyama, and H.-C. Kuo, 2001: Potential vorticity in a moist atmosphere. *J. Atmos. Sci.*, **58**, 3148–3157.

Schubert, W. H., 2004: A generalization of Ertel's potential vorticity to a cloudy, precipitating atmophere. *Meteorol. Zeits.*, **13**, 465–471.

Schubert, W. H., and M. T. Masarik, 2006: Potential vorticity aspects of the MJO. *Dyn. Atmos. Oceans*, **42**, 127–151.

Schubert, W. H., C. M. Rozoff, J. L. Vigh, B. D. McNoldy, and J. P. Kossin, 2007: On the distribution of subsidence in the hurricane eye. *Q. J. R. Meteorol. Soc., in press.*

Shapiro, L. J., and H. E. Willoughby, 1982: The response of balanced hurricanes to local sources of heat and momentum. *J. Atmos. Sci.*, **39**, 378–394.

Shapiro, L. J., and M. T. Montgomery, 1993: A three-dimensional balance theory for rapidly rotating vortices. *J. Atmos. Sci.*, **50**, 3322–3335.

Simpson, R. H., and L. G. Starrett, 1955: Further studies of hurricane structure by aircraft reconnaissance. *Bull. Amer. Meteor. Soc.*, **36**, 459–468.

Smagorinsky, J., 1963: General circulation experiments with the primitive equations. I. The basic experiment. *Mon. Wea. Rev.* , **91**, 99–164.

Snow, J., S.-H. Chen, R. L. Elsberry, G. Holland, T. N. Krishnamurti, M. T. Montgomery, and R. Rotunno, 2006: *National Oceanic and Atmospheric Administration (NOAA) Science Advisory Board: Final Majority Report of the Hurricane Intensity Research Working Group*, 43 pp.

Terwey, W. D., and M. T. Montgomery, 2006: Modeled secondary eyewall and spiral band dynamics. *27th Conf. On Hurricanes and Tropical Meteorology*, Monterey, CA, Preprints, American Meteorological Society.

Walko, R. L., W. R. Cotton, M. P. Meyers, and J. Y. Harrington, 1995: New RAMS cloud microphysics parameterization. Part I: the single-moment scheme. *Atmos. Res.*, **38**, 29–62.

Wang, Y., 2001: An explicit simulation of tropical cyclones with a triply nested movable mesh primitive equation model: TCM3. Part I: model description and control experiment. *Mon. Wea. Rev.*, **129**, 1370–1394.

Wang, Y., 2002: Vortex Rossby waves in a numerically simulated tropical cyclone. Part I: overall structure, potential vorticity, and kinetic energy budgets. *J. Atmos. Sci.*, **59**, 1213–1238.

Wang, Y., 2006: Concentric eyewall simulated in a fully compressible, nonhydrostatic, multiply nested, movable mesh tropical cyclone model (TCM4). *27th Conf. On Hurricanes and Tropical Meteorology*, Monterey, CA, Preprints, American Meteorological Society.

Weisman, M. L., and J. B. Klemp, 1982: The dependence of numerically simulated convective storms on vertical wind shear and buoyancy. *Mon. Wea. Rev.*, **110**, 504–520.

Weisman, M. L., and R. Rotunno, 2004: "A theory for strong long-lived squall lines" revisited. *J. Atmos. Sci.*, **61**, 361–382.

Weiss, J., 1991: The dynamics of enstrophy transfer in two-dimensional turbulence. *Physica D*, **48**, 273–294.

Wilhelmson, R. B., and J. B. Klemp, 1978: A numerical study of storm splitting that leads to long-lived storms. *J. Atmos. Sci.*, **35**, 1974–1986.

Wilhelmson, R. B., and L. J. Wicker, 2001: Numerical modeling of severe local storms. *Severe Convective Storms, Meteor. Monogr.*, No. 50, Amer. Meteor. Soc., 123–166.

Willoughby, H. E., and M. B. Chelmow, 1982: Objective determination of hurricane tracks from aircraft observations. *Mon. Wea. Rev.*, **119**, 1298–1305.

Willoughby, H. E., J. A. Clos, and M. G. Shoreibah, 1982: Concentric eye walls, secondary wind maxima, and the evolution of the hurricane vortex. *J. Atmos. Sci.*, **39**, 395–411.

Willoughby, H. E., H.-L. Jin, S. J. Lord, and J. M. Piotrowicz, 1984: Hurricane structure and evolution as simulated by an axisymmetric, non-hydrostatic numerical model. *J. Atmos. Sci.*, **41**, 1169–1186.

Willoughby, H. E., 1990: Temporal changes of the primary circulation in tropical cyclones. *J. Atmos. Sci.*, **47**, 242–264.

Yau, M. K., Y. Chen, and M. T. Montgomery, 2006: The formation of concentric eyewall in Hurricane Floyd (1999). *27th Conf. On Hurricanes and Tropical Meteorology*, Monterey, CA, Preprints, American Meteorological Society.

Yoshikawa, Y., and K. Akitomo, 2003: Transverse roll convection in horizontal plane Couette flow. *J. Fluid Mech.*, **493**, 191–208.

Zeng, X., 1996: Numerical simulation of tropical cyclones by an axisymmetric nonhydrostatic model. *Meteorol. Atmos. Phys.*, **60**, 207–224.

Zhang, Q.-H., Y.-H. Kuo, and S.-J. Chen, 2005: Interaction between concentric eyewalls in super typhoon Winnie (1997). *Q. J. R. Meteorol. Soc.*, **131**, 3183–3204.

Zipser, E. J., R. J. Meitin, and M. A. LeMone, 1981: Mesoscale motion fields associated with a slowly moving GATE convective band. *J. Atmos. Sci.*, **38**, 1725–1750.